2017

# Plasmonic Approaches and Photoemission: Ag-Based Photocathodes

Zhaozhu Li
*College of William and Mary*, zli@email.wm.edu

Follow this and additional works at: https://scholarworks.wm.edu/etd

Part of the Physics Commons

Plasmonic Approaches and Photoemission: Ag-based Photocathodes

Zhaozhu Li

Qiqihar, Heilongjiang Province, China

Bachelor of Science, University of Science and Technology of China, 2009
Master of Science, The College of William & Mary, 2011

A Dissertation presented to the Graduate Faculty
of The College of William & Mary in Candidacy for the Degree of
Doctor of Philosophy

Department of Physics

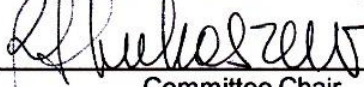College of William & Mary
August, 2017

# APPROVAL PAGE

This Dissertation is submitted in partial fulfillment of
the requirements for the degree of

Doctor of Philosophy
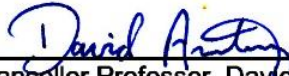
_____
Zhaozhu Li

Approved by the Committee, May, 2017

_____
Committee Chair
Virginia Microelectronics Consortium Distinguished Professor, R. Alejandra Lukaszew,
Physics
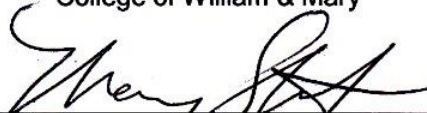College of William & Mary

_____
Chancellor Professor, David Armstrong, Physics
College of William & Mary

_____
Assistant Professor, Eugeniy Mikhailov, Physics
College of William & Mary

_____
Associate Professor, Mumtaz Qazilbash, Physics
College of William & Mary

_____
Dr. Marcy Stutzman
Jefferson Lab

# ABSTRACT

Photocathodes play an important role in present large accelerator facilities by providing polarized or un-polarized electron beams. Current state-of-art high polarization photocathodes consist of strained super-lattice GaAs based photocathodes, e.g. GaAs/GaAsP has a quantum efficiency ~1% and polarization ~90% at near-infrared wavelength for the incident light. Despite the advantages offered by metallic photocathodes regarding longer life time, fast response time and low requirements of ultra-high vacuum environment, they have not been put to use due to their low quantum efficiency, even though one can envision several approaches to achieve spin-polarization from them. A possible solution is to apply the Fano resonance, that involves coupling the surface plasmon resonance and the 1st diffraction order of incident light on a corrugated silver surface. This thesis demonstrates that this approach yields an enhancement of the QE performance of a cesiated silver grating cathode for light incident at the resonance angle, compared to that of a cesiated flat silver cathode measured in the same system. By altering the grating profile through oblique angle deposition (OAD) of a silver thin film onto a grating surface using magnetron sputtering deposition, one can further enhance the Fano resonance and consequently improve the electric field intensity near the silver cathode surface. QE measurements confirm an enhancement of QE (26%) on the cesiated OAD sample compared to a cesiated one obtained under normal deposition(ND) for light incident at resonance, respectively, showcasing a possible road for metallic photocathodes for this application.

# TABLE OF CONTENTS

# ACKNOWLEDGEMENTS

This dissertation is the product of many years of hard work, perseverance, and perhaps the same dose of setback and frustration. During those years, I owe so much to so many people around me. Most of all, I would like to express my appreciation to my advisor Professor Ale Lukaszew, who has mentored and trusted in me throughout my graduate studies. I also thank all the other members of our research group –José Riso, Kaida Yang, Melissa Beebe, Douglas Berringer, Scott Madaras; and many those who already have graduated: Lei Wang and William Roach. Their involvement and support has taught me the way with team collaboration as well as the way with being a doctoral student. I'd like to specially thank three other brilliant scientists Mike Klopf, Marcy Stutzman and Matt Poelker, who generously supported and contributed to this dissertation project. I'm also very thankful for my committee members, David Armstrong, Mumtaz Qazilbash, Eugeniy Mikhailov and Marcy Stutzman for their insightful comments and persistent encouragement. Last and not the least, my thanks also go to the faculty and staff members at the Department of Physics at the College of William and Mary, for their dedicated kindness and support to me throughout my graduate work.

This Ph.D. is dedicated to my Lord Jesus, who have trusted and helped me all along.

# LIST OF TABLES

# LIST OF FIGURES

# Chapter 1  Introduction

1.1  Overview

Chapter 1 will introduce photocathodes and the fundamental theory of photoemission. It will also discuss the theories of surface plasmon resonance (SPR) and the Fano resonance, which are fundamental to the design of this project to enhance the quantum efficiency (QE) of silver cathodes. Chapter 2 will discuss the experimental apparatus and method that was used in this project, including an ultra-high vacuum (UHV) system using physical vapor deposition (PVD) method, a QE measurement system and other characterization instruments. Chapter 3 will discuss the effect of MgO as a layer to lower the work function on a crystalline silver substrate. It will also discuss the measurements of QE on MgO/Ag grating cathodes. Chapter 4 will discuss the measurements of QE on Cs/Ag grating cathodes. Chapter 5 will discuss the measurements of QE on Cs/Ag grating cathodes deposited by oblique angle deposition (OAD). Chapter 6 will provide conclusions and the outlook on plasmonic silmanal cathodes that can be used for polarized electron beam production.

1.2  Photocathodes

Photocathodes are material surfaces that emit electrons when light shines upon them. This phenomenon, the so called "photoelectric effect", was first discovered by Hertz in 1887. The manufacturing development of photocathodes has yielded industrial application of photocathodes for photomultipliers, image sensors, photoelectric spectroscopy, night vision devices, and other products.

One of the features of photocathodes that has gained attention in the field of accelerator applications, since the mid-1970's, is the capability to emit spin-polarized electrons. One

example is GaAs.  In 1978, researchers at SLAC[1] used the first GaAs photoinjector to perform parity violation experiments that verified the electroweak sector of the (now) standard model of particle physics.  Further improvements to the design of GaAs photocathodes involved the use of strained-layerGaAs photocathodes and strained-superlattice (multi-layer) GaAs/GaAsP photocathodes. The latter is a state-of-art photocathode for large accelerator applications which can provide a high quantum efficiency (QE) ~ 1% and a high degree of polarization, ~85%[2].

Such photocathodes are semiconductor-based photocathodes, which are characterized by their relatively high QE, such as >10% for bulk GaAs at 550nm illumination. However, semiconductor photocathodes have their limitations. One of the limitations is that the surface of a semiconductor photocathode tends to be damaged by ion bombardment, which is generated from the collisions of electrons and the residual gas molecules. Consequently, semiconductor photocathodes require ultrahigh vacuum pressure for operation (~$10^{-11}$ Torr). In addition, the response time of the semiconductor-based photocathodes is ~10s picoseconds, which makes them unsuitable for applications to generate sub-picosecond electrons.

In contrast, bare metallic photocathodes are more robust to environmental contaminations. They can operate at $10^{-9}$ Torr and have long lifetimes (~years). They also have very fast response times, which are less than a picosecond. However, they are of limited use for many applications because of their low QE (~$10^{-5}$ at UV illumination). A review of the three-step model of the photoemission process[3] can help us to understand their low QE.

1.3 Three-step model of the photoemission process

The emission of electrons from photocathodes can be described in three steps: 1) The electrons absorb the photon energy and are excited to the conduction band from the valence band; 2) The electrons overcome the scattering processes with other electrons or the lattice and travel to the surface. Many electrons lose their energy in the form of heat and cannot reach the surface of the cathode; 3) The electrons overcome the potential at the surface and escape from the cathode surface. The emitted electrons are the photoelectrons observed during the QE measurement. The photoemission processes for metal and semiconductor photocathodes are shown in Figure 1.1.
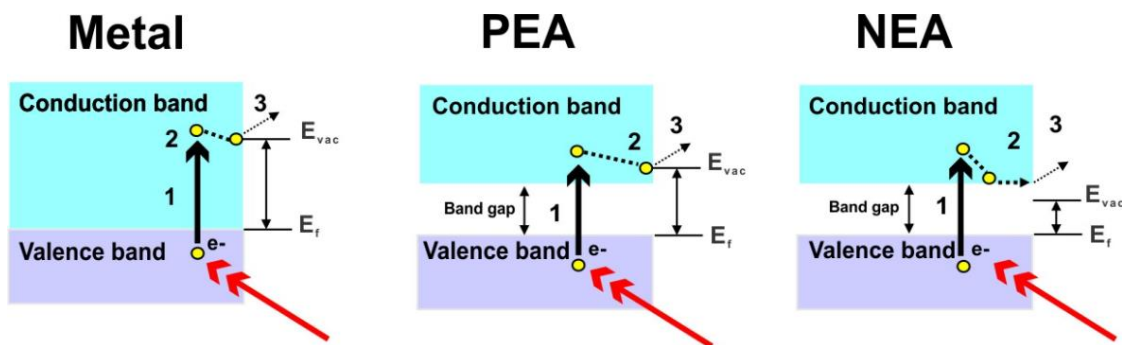


**Figure 1.1 Photoemission processes for metal, Positive Electron Affinity (PEA) semiconductor and Negative Electron Affinity (NEA) semiconductor photocathodes.**

The metal and semiconductor photocathodes show different behaviors in this model for photoemission. For metal photocathodes, the reflectivity is typically high and consequently only a small portion of the light can be absorbed so that it penetrates below the cathode surface. Then at the second step, electron-electron scattering process is the main process. Because of the high density of electrons in the conduction band for metals, the probability of electron-electron scattering is quite high. Thus, a large fraction of photoelectrons will eventually lose their energy and fail to reach the metal surface. The work function of a metal – i.e. the energy required to remove an electron from the metal --- is quite high. The work function is the difference between the Fermi Energy and the vacuum energy of the

metal. For an alkali metal, the work function energy is approximately that of visible light photon. For other metals, the energy is mostly in the ultra-violet wavelength region. This makes few electrons can overcome the work function very few.

Conversely, semiconductor photocathodes have a high efficiency for light absorption. They have a rather low reflectivity, and the photon absorption efficiency for energy above the band gap is high. For semiconductor photocathodes, the main scattering process is electron-phonon scattering, in which the energy loss per collision is much less than the electron-electron scattering in metals. Thus photoelectrons can exist a longer time during the scattering process, which means an electron that is deeper from the surface can be excited and can migrate to the surface. There are two types of electron affinity for semiconductor photocathodes: the negative electron affinity (NEA) and positive electron affinity (PEA). For the PEA semiconductors, electrons need to overcome the bandgap energy plus the electron affinity at the surface in order to escape from the surface. For the NEA semiconductors, their vacuum energy near the surface is typically lower than the conduction minimum energy of the bulk. Any electrons in the conduction band that are able to migrate to the surface will escape from the cathode and give a high QE. For NEA GaAs, the QE at 532nm is ~ 10% or higher.

Thus it is interesting to study metal photocathodes with the goal of improving their low quantum efficiency, while taking advantage of the long lifetime and potential polarized material such as silmanal. In this project, plasmonic approaches have been applied to improve the QE of silver-based photocathodes, which will be illustrated below.

1.4  Plasmonic Approaches

This section discusses the background theory of plasmonic resonance, which was used in this study to guide the design of the cathodes and the measurements of QE.

### 1.4.1 Surface Plasmon Resonance

Surface plasmon resonance (SPR) is a coherent resonance behavior[4] of surface electrons in a metal when a certain dispersion relationship of the incident electrons or the light is met. It was first demonstrated by Powell and Swan in their experiments on electron-energy loss[5] in 1960 and has been diligently studied by scientists since then. At the excitation of the resonance, an electromagnetic wave propagates along the surface and enhances the electromagnetic field. This phenomenon can be utilized in surface-plasmon-enhanced photoemission, strong Raman scattering (SERS), etc.

The dispersion relationship of the surface plasmon resonance can be described by the Maxwell equations applied to the surface of a semi-infinite solid system, which is shown in Figure 1.2[2]. The systems' interface between materials 1 & 2 has a dielectric constant $\varepsilon_1 = \varepsilon_1' + i\varepsilon_1''$ and $\varepsilon_2$ (vacuum or air).
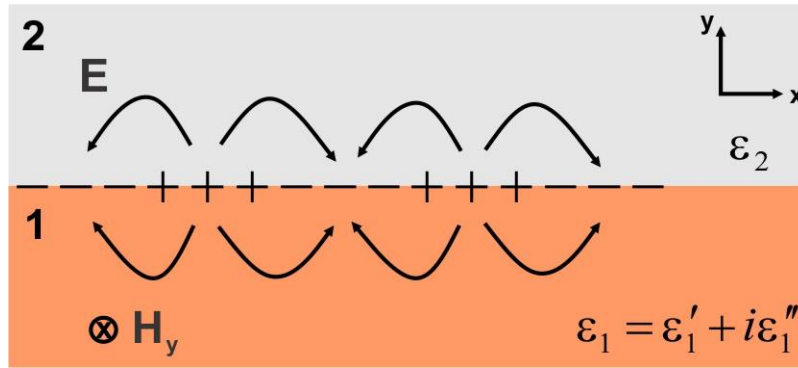


**Figure 1.2 A semi-infinite solid system with excitation of SPR from p-polarized incident light. Charges and the propagation of SPR wave on the surface are shown in the figure[2].**

The electric field in the system can be described as

$$\vec{E} = \vec{E}_0^{\pm} \exp[i(k_x x \pm k_z z - \omega t] \quad , \quad (1.1)$$

where "+" is for $z \geq 0$ and "−" is for $z \leq 0$; $E_0^{\pm}$ is the electric field in the indicated

directions for z. $k_x = k_x' + ik_x''$ is the complex wave vector in the x direction and

$k_z = k_z' + ik_z''$ is the complex wave vector in the z direction; $\omega$ is the angular frequency.

Specifically, we can write the electric and magnetic field in medium 1 and medium 2 as:

$$\begin{cases} \vec{H}_2 = \hat{y}H_{y2}\exp[i(k_{x2}x + k_{z2}z - \omega t)] \\ \vec{E}_2 = (\hat{x}E_{x2} + \hat{z}E_{z2})\exp[i(k_{x2}x + k_{z2}z - \omega t] \end{cases} \quad z > 0 \quad , \quad (1.2)$$

$$\begin{cases} \vec{H}_1 = \hat{y}H_{y1}\exp[i(k_{x1}x - k_{z1}z - \omega t)] \\ \vec{E}_1 = (\hat{x}E_{x1} + \hat{z}E_{z1})\exp[i(k_{x1}x - k_{z1}z - \omega t] \end{cases} \quad z < 0 \quad , \quad (1.3)$$

where $\hat{x}$, $\hat{y}$ and $\hat{z}$ are the unit vectors in each respective direction. These fields must

satisfy Maxwell's equations:

$$\begin{cases} \nabla \times \vec{H}_i = \varepsilon_i \varepsilon_0 \dfrac{\partial E_i}{\partial t} \\ \nabla \times \vec{E}_i = -\mu_0 \dfrac{\partial H_i}{\partial t} \\ \nabla \cdot \vec{H}_i = 0 \\ \nabla \cdot (\varepsilon_i \varepsilon_0 \vec{E}_i) = 0 \quad , \end{cases} \quad (1.4)$$

subject to the boundary conditions (z=0):

$$\begin{cases} \hat{z} \times \hat{y}(H_{y2}\exp ik_{x2}x - H_{y1}\exp ik_{x1}x) = 0 \\ \hat{z} \times \hat{x}(E_{x2}\exp ik_{x2}x - E_{x1}\exp ik_{x1}x) = 0 \\ \hat{z} \cdot \hat{z}(\varepsilon_2 E_{z2} - \varepsilon_1 E_{z1}) = 0 \quad . \end{cases} \quad (1.5)$$

6

From equations (1.4) we can get

$$H_{y2} = H_{y1}$$
$$E_{x2} = E_{x1} \qquad (1.6)$$
$$\varepsilon_2 E_{z2} = \varepsilon_1 E_{z1}$$

with

$$k_{x1} = k_{x2} = k_x \quad . \quad (1.7)$$

From equation (1.3) we can get

$$\hat{x} \times \hat{y}(ik_x H_{y2} \exp i(k_x x + k_{z2} z) = -\hat{z} i \omega \varepsilon_0 \varepsilon_2 E_{z2} \exp i(k_x x + k_{z2} z)$$
$$\hat{z} \times \hat{y}(ik_{z2} H_{y2} \exp i(k_x x + k_{z2} z) = -\hat{x} i \omega \varepsilon_0 \varepsilon_2 E_x \exp i(k_x x + k_{z2} z)$$
$$\hat{x} \times \hat{y}(ik_x H_{y1} \exp i(k_x x + k_{z1} z) = -\hat{z} i \omega \varepsilon_0 \varepsilon_1 E_{z1} \exp i(k_x x - k_{z1} z)$$
$$\hat{z} \times \hat{y}(ik_{z1} H_{y1} \exp i(k_x x + k_{z1} z) = \hat{x} i \omega \varepsilon_0 \varepsilon_1 E_x \exp i(k_x x - k_{z1} z) \quad .$$

$$(1.8)$$

From equation (1.7) we can get

$$k_x H_{y2} = -\omega \varepsilon_0 \varepsilon_2 E_{z2}$$
$$k_{z2} H_{y2} = -\omega \varepsilon_0 \varepsilon_2 E_x$$
$$k_x H_{y1} = -\omega \varepsilon_0 \varepsilon_1 E_{z1} \qquad \text{and} \qquad \frac{k_{z1}}{\varepsilon_1} + \frac{k_{z2}}{\varepsilon_2} = 0 \quad (1.9)$$
$$k_{z1} H_{y1} = \omega \varepsilon_0 \varepsilon_1 E_x \quad .$$

Similarly, from equation (1.3) we can also get

7

$$\hat{z} \times \hat{x} i(k_{z2}E_{x2} - k_x E_{z2}) \exp i(k_x x + k_{z2}z) = -\hat{y} i\omega\mu_0 H_{y2} \exp i(k_x x + k_{z2}z)$$

$$\text{(1.10)}$$

$$\hat{z} \times \hat{x} i(-k_{z1}E_{x1} - k_x E_{z1}) \exp i(k_x x - k_{z1}z) = -\hat{y} i\omega\mu_0 H_{y1} \exp i(k_x x - k_{z1}z) \quad .$$

Thus we get

$$k_{z2}E_{x2} - k_x E_{z2} = -\omega\mu_0 H_{y2}$$
$$k_{z1}E_{x1} + k_x E_{z1} = \omega\mu_0 H_{y1} \quad .$$
$$\text{(1.11)},$$

Together with equation (1.9) we have

$$k_{z2}^2 + k_x^2 = \frac{\omega^2}{c^2}\varepsilon_2$$
$$k_{z1}^2 + k_x^2 = \frac{\omega^2}{c^2}\varepsilon_1 \quad .$$
$$\text{(1.12)}$$

Thus, from equation (1.9) and (1.12) we have

$$k_x = \frac{\omega}{c}\sqrt{\frac{\varepsilon_1\varepsilon_2}{\varepsilon_1 + \varepsilon_2}} = k_{spp} \quad . \quad \text{(1.13)}$$

Equation (1.13) gives the dispersion relationship for surface plasmon excitation on a semi-infinite solid system.

Quite often medium 2 is vacuum or air, giving its dielectric constant $\varepsilon_2 \sim 1$. Thus equation (1.13) will reduce to

$$k_x = \frac{\omega}{c}\sqrt{\frac{\varepsilon_1}{\varepsilon_1 + 1}} = k_{spp} \quad . \quad \text{(1.14)}$$

If we assume that $\varepsilon_1'' < |\varepsilon_1'|$, then equation (1.14) can be rewritten as

$$k_x' = \frac{\omega}{c}\sqrt{\frac{\varepsilon_1'}{\varepsilon_1'+1}}$$

(1.15)

$$k_x'' = \frac{\omega}{c}\sqrt{(\frac{\varepsilon_1'}{\varepsilon_1'+1})^3}\,\frac{\varepsilon_1''}{2(\varepsilon_1')^2}\qquad.$$

To let $k_x'$ become real, $\varepsilon_1' < 0$ and $|\varepsilon_1'|$ has to be larger than 1. This condition is satisfied by most metals.

Figure 1.3 shows the dispersion relationship of surface plasmons(SPs). One can observe that the wave vector of SPs is on the right side of the light line, i.e. $k_0 = \dfrac{\omega}{c}$ , and indicates the need to use some sort of coupling to provide the internal wave excitation. At the extreme condition of $-\varepsilon_1' \to \varepsilon_2$, the resonance frequency reaches the limit of

$\omega = \dfrac{\omega_p}{\sqrt{1+\varepsilon_2}}$, where $\omega_p = \dfrac{4\pi n e^2}{m}$ is the plasmon frequency, e is the electron charge, n is the bulk electron density, and m is the effective electron mass.
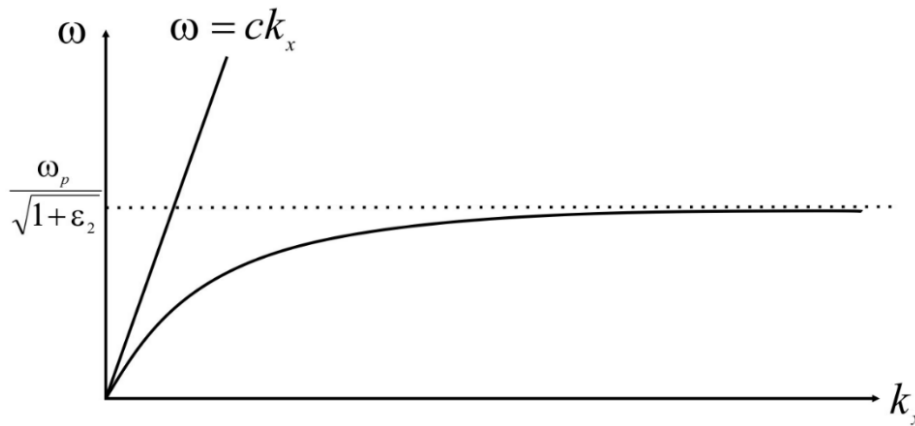


**Figure 1.3 Dispersion relationship of SPR excitation.**

9

The main kind of couplers to excite the SPR by light are:

- A prism used in Attenuated Total Reflection (ATR) geometry, where a medium with dielectric constant $n$ larger than 1 is applied above the metallic surface. The light that goes through the medium above the metal will have a wave vector of $k_x = \frac{\omega}{c} n \sin \theta$, where $\theta$ is the incident angle, $n$ is the refractive index of the medium. It satisfies the dispersion relationship in equation (1.14) when

$$k_x = \frac{\omega}{c} n \sin \theta = \frac{\omega}{c} \sqrt{\frac{\varepsilon_1'}{\varepsilon_1' + 1}}.$$

- A Grating coupler, where the wave vector of the incident light is added to a grating as in the left side of equation (1.15) below, where the condition for constructive interference depends on the grating periodicity thus the dispersion relationship becomes:

$$\frac{\omega}{c} \sin \theta \pm N \frac{2\pi}{\lambda_g} = k_{SPP} = \frac{\omega}{c} \sqrt{\frac{\varepsilon_1 \varepsilon_2}{\varepsilon_1 + \varepsilon_2}} \qquad (1.16)$$

Here $\theta$ is the incident angle for the laser light, $\lambda_g$ is the grating periodicity and $N$ is an integer.

The propagation length of SPs can be studied by examining the imaginary part of $k_x''$ in equation (1.15). The field intensity falls exponentially in the x direction. Defining a decay length as the intensity where the field amplitude falls to 1/e of its initial value, we have:

$$L_{SP} = \frac{1}{2k_x''} \qquad (1.17)$$

or substituting from the above:

$$L_{SP} = \frac{\lambda}{2\pi} \sqrt{(\frac{\varepsilon_1' + 1}{\varepsilon_1'})^3 \frac{(\varepsilon_1')^2}{\varepsilon_1''}} \qquad (1.18)$$

Similarly, the penetration depth for the SP field in the z direction is defined as

$$L_{zi} = \frac{1}{|k_{zi}|} \qquad (1.19)$$

From equation (1.11) and (1.14) we can obtain the depths for SPs in the z direction for interfaces between metal and either vacuum or air):

$$L_{z1} = \frac{\lambda}{2\pi} \left| \sqrt{\frac{\varepsilon_1' + 1}{(\varepsilon_1')^2}} \right|$$

$$\qquad (1.20)$$

$$L_{z2} = \frac{\lambda}{2\pi} \left| \sqrt{\varepsilon_1' + 1} \right|$$

For a 405nm wavelength light impinging on a vacuum/silver semi-infinite system, the propagation length in the x direction is computed to be 23.49 $\mu m$, and the z direction field depth in the metal (medium 1) is 27 nm.

## 1.4.2   Fano Resonance

Here we follow the development of a Fano resonance. Fano resonance describes the interaction between a localized (discrete) mode and a radiative (continuum) mode which gives an asymmetric profile of the incident light's angular frequency in measurable quantities such as reflectivity, transmission, etc. The radiative mode is often associated with plane-wave illumination which excites the localized mode in the system. This localized

mode in return interferes with the radiative mode and cause the asymmetric shape in the measurement quantity. A similar phenomenon has been observed in many other systems such as coupled clusters of metallic nano-particles[6-8], metallic photonic crystals[9] and metamaterials[6,10-13], etc. It is worth noting that this type of resonance can be used in applications including sensing[14,15], optical modulators [16-18], selective optical polarizers[19], etc., because of its unique properties. However, classical optical phenomena such as the Wood anomaly resulting from the interference between Surface Plasmon Resonance (SPR) with radiative diffraction orders have only recently been clearly understood. [6,20]

In the original work of Fano[21], the asymmetric response of the system is the product of the radiative mode with the Fano profile. Here the Fano profile can be described as:

$$F(\omega) = \frac{(\kappa + q)^2}{\kappa^2 + 1} \quad , \quad (1.21)$$

And $\kappa$ can be expressed as

$$\kappa = \frac{\omega^2 - \omega_l^2 - \omega_l \Delta}{\Gamma} \quad , \quad (1.22)$$

$$\Delta = \frac{\omega_l^2 - \omega_r^2}{\omega_l} \quad , \quad (1.23)$$

$$\Gamma = \gamma_r \omega_l \quad , \quad (1.24)$$

where $\omega_l$ is the resonance frequency of the localized mode and $\omega_r$ is the resonance frequency of the radiative mode. $\gamma_r$ is the loss of the radiative mode. $q$ characterizes the asymmetry of the resonance profile.

The overall profile $\sigma(\omega)$ is the coupling of the radiative mode and the Fano profile

$$\sigma(\omega) = \frac{\Gamma_r^2}{(\omega^2 - \omega_r^2) + \Gamma_r^2} F(\omega) \qquad (1.25)$$

The physics mechanism can be described as an analogy with respect to two coupled resonant electric circuits, as shown in Figure 1.4 (a). The radiative mode $L_l$ is excited by the source and excites the localized mode in $L_r$. However, the main limitation of the original Fano resonance expression is that it lacks accounting of intrinsic losses of the localized mode. Benjamin Gallinet and Olivier J. F. Martin proposed a new description of the Fano resonance[22-24], including consideration of intrinsic damping as shown in equation (1.26) ($R_l$ in Figure 1.4(b)). This treatment enables understanding the influence of electromagnetic interactions on the resonance through the information drawn from the Fano profile.
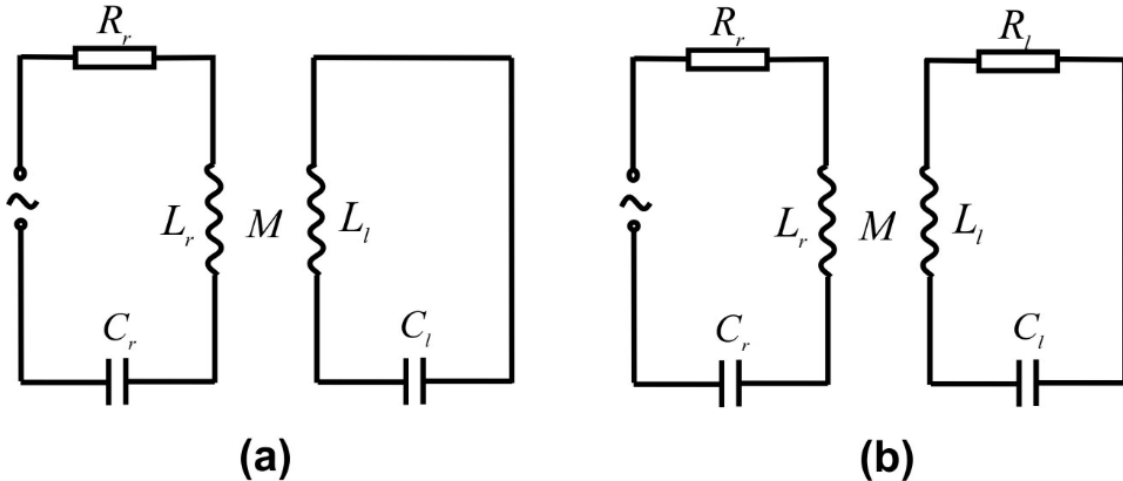


**Figure 1.4 Illustration of the underlying physics of the Fano resonance by two resonant electrical circuits: (a) Original description by Fano without consideration of intrinsic losses in localized mode (b) Modified description of Fano resonance including the consideration of the intrinsic losses ($R_l$) in the localized mode[22].**

Based on the extended model, the line profile for the localized mode is described in equation (1.26),

$$\sigma_l(\omega) = \frac{(\frac{\omega^2 - \omega_l^2}{2W_l\omega_l} + q)^2 + b}{(\frac{\omega^2 - \omega_l^2}{2W_l\omega_l})^2 + 1} \quad . \quad (1.26)$$

Here, $\omega$ is the angular frequency of the incident light, $\omega_l$ is the resonance central

spectral frequency, $W_l$ is an approximation of the spectral width where $W_l << \omega_l$, $b$

represents the damping of the Fano resonance which affects the contrast of the resonance

profile and $q$ characterizes the asymmetry of the resonance profile.

The radiative mode can be constructed as

$$\sigma_r(\omega) = \frac{a^2}{(\frac{\omega^2 - \omega_r^2}{2W_r\omega_r})^2 + 1} \quad , \quad (1.27)$$

where $a$ is the maximum amplitude, $\omega_r$ is the resonance frequency, and $W_r$ is the

approximated spectral width if $W_r << \omega_r$. The total response of the system is given by

equation (1.28), which results from the product of equation (1.26) and equation (1.27),

and can be applied to measurable quantities:

$$\sigma(\omega) = \sigma_l(\omega)\sigma_r(\omega) \quad . \quad (1.28)$$

One can apply equation (1.28) to either theoretical or experimental results for reflectance,

transmittance, absorbance, extinction and/or total cross section[20,22,23]. A fit of the data to

this function can provide all the parameters for radiative and localized modes for a better

understanding of the Fano resonance. Specifically, one can look at the damping in the

Fano resonance in the parameter $b$ [22-24]. The dielectric constants of metals have imaginary

parts that lead to the imaginary parts in the resonance frequency of a localized mode,

14

which prevents the two modes from interfering completely constructively or destructively. The $b$ parameter evaluates such effect as the ratio between the intensity lost to the metallic structure and the intensity transferred from the radiative mode to a localized mode. When $b$ equals 0, the intrinsic losses of the localized mode would fully disappear and the Fano profile is recovered as in equation (1.25). The parameter $q$ describes the asymmetry in the Fano profile. The parameter $q$ together with the modulation parameter $b$ describe the shape of the Fano resonance. The effect of $q$ and $b$ is shown in Figure 1.7, where

$\kappa = \dfrac{\omega^2 - \omega_l^2}{2W_l\omega_l}$. In a plasmonic system of a metallic grating coupler, the SPR could serve

as the localized mode interfering with the radiative mode (diffraction orders)[18] excited by the outside illumination. The total optical response from the illumination is thus the total result of a Fano resonance excited on the metallic grating.
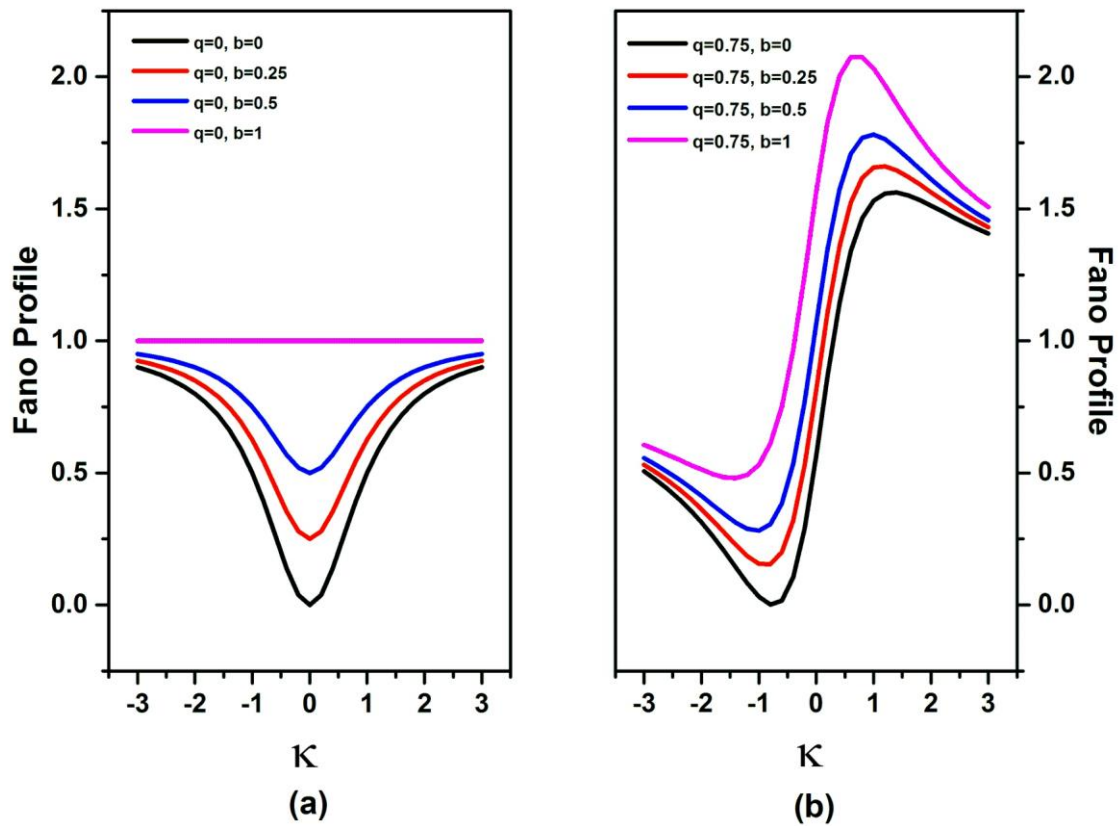
**Figure 1.5 Illustration of effects of parameter q and b: (a) shows when q=0, the resonance profile becomes symmetrical and b determines the profile contrast (b) when q>0, the profile becomes asymmetrical.**

# Chapter 2 Experimental Apparatus and Measurement Methods

2.1 Introduction

This chapter will describe typical vacuum pumps used in ultra-high vacuum (UHV) systems. Deposition methods for thin film growth will also be described, such as evaporation deposition and magnetron sputtering deposition. Oblique angle deposition (OAD) based on the magnetron sputtering deposition will also be presented. Characterization methods will be briefly described such as Atomic Force Microscopy (AFM) and Scanning Electron Microscope (SEM) and X-ray Reflectometry (XRR). A system for QE measurement and its measurement uncertainty will be presented. The optical system for reflectivity measurements that was used for characterization of the plasmonic resonance will also be illustrated.

2.2. Ultra High Vacuum System Apparatus

2.2.1 Vacuum Pumps

To reach an ultra-high vacuum, different types of pumps are required to constitute a pumping system. The vacuum pumps can be classified based on two types of mechanism: gas transfer and gas capture. Gas transfer pumps compress gas molecules in a specific direction and eject them into the atmosphere. In such pumps, roughing pumps are suitable for pumping from atmosphere down to $10^{-2}$~$10^{-3}$ Torr. Turbo pumps can reach to $10^{-11}$ Torr with proper configurations and treatments. Gas capture pumps capture gas molecules on pump surfaces through physical or chemical reactions and are often suitable for small gas loads below $10^{-3}$ Torr. However, cryo pumps can be used for large gas loads in semiconductor fabrication processes.

One example of the pumps used in the UHV chamber of our sample deposition and QE measurement is shown in Table 2.1.

| | Rough Pump | Turbo Pump | Cryo Pump | Ion Pump | NEG Pump |
|---|---|---|---|---|---|
| Gas Transfer | Y | Y | N | N | N |
| Gas Capture | N | N | Y | Y | Y |

**Table 2.1 Classification of vacuum pumps including rough pump, turbo pump, cryo pump, ion pump and non-evaporable getter (NEG) pump. Y/N refers to yes or no.**

An ideal pump for a vacuum system is one with a fast pumping speed and low effective base pressure. To maintain an UHV environment, four types of typical pumps are described: turbomolecular pumps, sputter-ion pumps, cryogenic pumps and getter pumps.

2.2.2 Turbomolecular Pumps

Turbomolecular pumps are gas-transferring pumps that compress the gas by momentum transfer. They were used during the bake-out of the QE chamber. The operation of a turbo pump involves the high-speed rotation of blades with speeds ranging from 24,000 to 6,000 rpm[25]. It must be used in combination with a roughing pump because of the preferred high working efficiency in the molecular flow range, which is below $10^{-3}$ Torr. By a proper choice of roughing pump, a pressure of $10^{-8}$ Torr can be produced. For a turbo pump, hydrogen molecules are often the main component of the residual gas because of its low compression ratio. This can be partially relieved by the application of getter pumps, such as titanium sublimation pumps[26].

### 2.2.3 Sputter-Ion Pumps

A sputter-ion pump (thereafter called an ion pump) we use, contains a multi-cell anode and a titanium plate as well as a tantalum plate at its sides. Here we take the construction of an ion pump from Gamma Vacuum[27] for illustration. In the module of an ion pump, ferromagnets are placed outside of the stainless-steel vacuum wall to create a large magnetic field of ~0.12 T through the cathode and anode assembly. A high voltage of 3-7 kilovolts is applied to the anode, which is electrically isolated from the rest of the ion pump. The cathode and the other parts of the ion pump are at ground potential. After entering the pump, electrons are drawn to the anode. The magnetic field inside the system causes the electrons to oscillate spirally in the anode ring and significantly increase their collision probability with gas molecules. As a result, positively charged ions are produced after the collisions and accelerated to the grounded cathode surface. The ions of an active gas, such as oxygen and nitrogen, chemically react with the Titanium atoms and form Titanium compounds on the cathode surface. In the meantime, Titanium atoms are sputtered either directly to the anode wall or form titanium compound by chemical reactions.

When the ion pump is normally operated, the ion current is in a proportional relationship with the vacuum pressure, which can free the system from the need to have a high-vacuum gauge. Depending on pump size, ion pumps can start pumping from $10^{-4}$ Torr or below. Ion pumps, together with the following NEG pumps, are the main pumps used in the QE chamber.

### 2.2.4 Cryogenic Pumps

The mechanism of cryogenic pumps is the physical capture of gas molecules on a cooled surface though either gas cooling or liquid cooling. They were used in the PVD system to reach a high vacuum environment. It binds gas molecules by van der Waals forces which are dependent on the temperature of the molecules. It requires a vacuum environment of

$10^{-3}$ Torr or below to start operating. This requirement avoids the overload of the refrigerant and an unnecessary thick condensate which would be caused by a large gas load[28].

## 2.2.5 Non-evaporable Getter Pumps

NEG pumps use very active alloys that contains Zr or Ti and chemically react with the active gas molecules such as oxygen, nitrogen, carbon monoxide, carbon dioxide and water molecules. In contrast to other pumps, NEG pumps are ideal for pumping hydrogen with highest pumping efficiency[29]. A pressure of or below $10^{-4}$ Torr is required for the operation of getter pumps.

## 2.2.6 Residual Gas Analyzer (RGA)

RGA is widely applied in UHV systems because of its capability to identify the gas composition in the vacuum environment. It can also serve as a leak testing system. The operation of RGA involves the ionization of the gas molecules in the vacuum through an ionizer inside the module. The mass of the ions is expressed by the mass number M in the unit of atomic mass unit (amu). An example of such a scan is shown in Figure 2.1. By identifying the species through the mass number, the component of gas molecules inside the vacuum system is analyzed. The height of the peak at each mass number gives the partial pressure of such molecule.  This is helpful to keep track of the gas components on the same vacuum system consistently.
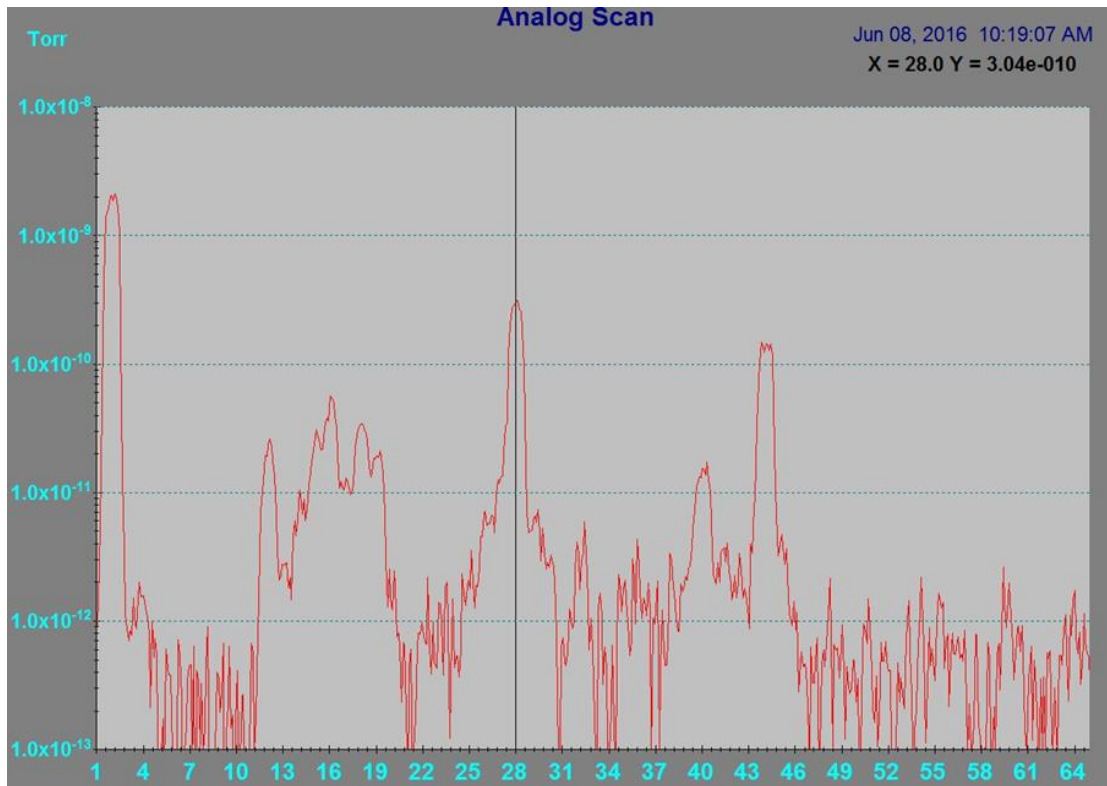
**Figure 2.1 An example of analog Scan of RGA with pressure versus M/Q.**

Although gas components in the vacuum system can be different, some typical gas species in our vacuum system are listed below. As is shown in Figure 2.1, a dominant partial pressure of hydrogen at M/Q = 2 is typical in the UHV system. Helium causes the peak at M/Q = 4.  $O^+$, $HO^+$ and $H_2O^+$, which are ionized from water molecules, contribute to the peaks at 16-18. Either nitrogen or carbon monoxide causes the peak at 28. Molecular oxygen causes the peak at 32. Argon causes the peak at 40. Carbon dioxide causes the peak at 44.  Doubly ionized $CO_2^{++}$ contributes to the peak at 22 and $C^+$ at 12.  A mass number in the range of 13-16 can be methane or a fraction of methane.

In spite of the application as a gas component analyzer, RGA is also frequently used in the detection of potential leaks. When assembling a UHV system, it is important to find and remove the existence of leaks before further baking of the whole system. The RGA monitors the partial pressure of single gas molecules during leak detection. Although RGA

21

does not require a specific gas to work as a leak detector, helium is often chosen for its small particle size that enables the detection of very small leaks (~$10^{10}$ Torr) on the UHV system[30].

2.3 Physical Vapor Deposition (PVD)

PVD is typically operated under a HV or UHV environment and involves physical processes with the source atoms. These processes start with the evaporation of source atoms into gas phase either by thermal heating or kinetic collision and are followed by the migration of evaporated source atoms to the substrate and lastly the condensation of the source atoms on the substrate surface. Two main evaporation methods used in PVD include evaporation deposition and magnetron sputtering deposition. Both are are discussed in the following section.

2.3.1 Evaporation Deposition

In evaporation deposition, the source atoms are evaporated by thermal heating. In this project, we use evaporation deposition in the activation of cathode by cesium. The rate of evaporation is related to the source's equilibrium vapor pressure. The equilibrium vapor pressure (thereafter called vapor pressure), is defined as the pressure exerted by a vapor in equilibrium with its solid or liquid state in a closed system at a certain temperature. The rate of evaporation become maximized when the vapor pressure is achieved and no gas molecules will return to the condensed state[31].

Different types of evaporation sources also affect the evaporated particles. For metals, atoms or clusters of atoms will evaporate from the source and condense at the destination. However, for the evaporation of compounds, molecules are often not preserved and this results in a different stoichiometry in the deposited film compared to that of the source.

Alloys evaporate the atoms of different metals nearly independently of each other and thus display a similar behavior to that of metal evaporation.

There are 2 types of heating mechanisms applied in the heater design for an evaporation process. One is resistance-heated evaporation and the other is electron-beam evaporation. For resistance-heated evaporation sources, the material of the heater should be free of contaminants to the source during the heating process. It should also avoid releasing active gases such as oxygen, nitrogen, hydrogen and should have a low vapor pressure at the evaporation temperature of the source.  Table 2.2 gives typical types of resistance-heated evaporation sources.

|  | Tungsten Wire Sources | Refractory Metal Sheet Sources | Sublimation Furnaces | Crucible Sources |
|---|---|---|---|---|
| Material | W | W, Ta, Mo | Ta | Crucibles |
| Note | Requires low-voltage, high-current power supply. | Requires low-voltage, high-current power supply. | For sulfides, selenides and some oxides deposition. | Crucibles are often surrounded by W for heating. |

**Table 2.2 Types of resistance-heated evaporation sources[31].**

Electron-beam evaporation is preferred for highly pure films. The electrons are produced from thermionic emission, field emission and accelerated by the filament cathode assembly biased from 4 to 20kV and directed into a curved path by an applied magnetic field. By this means, the electrons are focused on the grounded source and heat up a small area on the source surface for evaporation. An illustration of this process is in Figure 2.2[32].
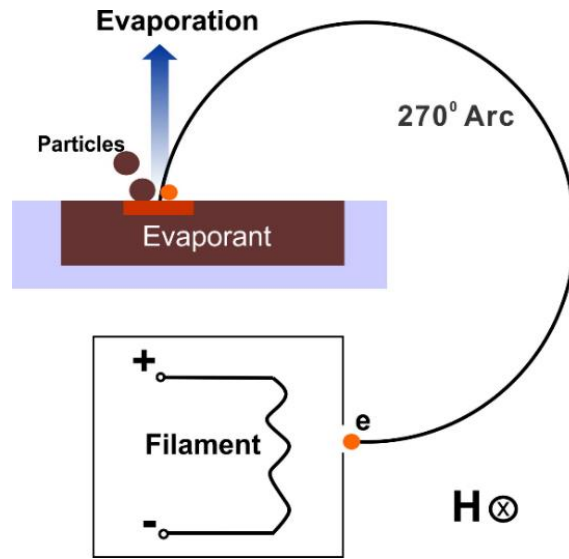
**Figure 2.2 Illustration of electron beam evaporation process[32].**

2.3.2 Magnetron Sputtering Deposition

In contrast, a magnetron sputtering deposition system evaporates the source atoms by kinetic collisions. Deposition of metallic grating thin films such as Ag are carried by magnetron sputtering deposition. In the deposition process, inert gas molecules with large molecular weight are initially introduced into the vacuum environment at a typical pressure of $10^{-3}$ Torr, and are then positively ionized and accelerated to the negative-biased target surface. These ions are called "bombardment ions". When the bombardment ions collide with the target surface, target atoms are ejected and condense at the substrate surface and nucleate into a film. The mechanism of the magnetron sputtering process is shown in Figure 2.3[33].

At the same time, secondary electrons are released and neutralization of bombardment ions also occurs. The secondary electrons are the electrons produced and ejected out of the target when ions collide with target surface. The magnetic field is engineered to be parallel to the target surface, as shown in Figure 2.4. The combination of electric and

magnetic field causes the electrons to drift above the target surface and increases the production of bombardment ions[34].

In applications, Ar is a typical choice for research and industry because of its heavy mass, chemical inertness and cost efficency[35]. Other rare gases such as Xe, Ne and Kr[36-38] have also been used, however with higher costs.
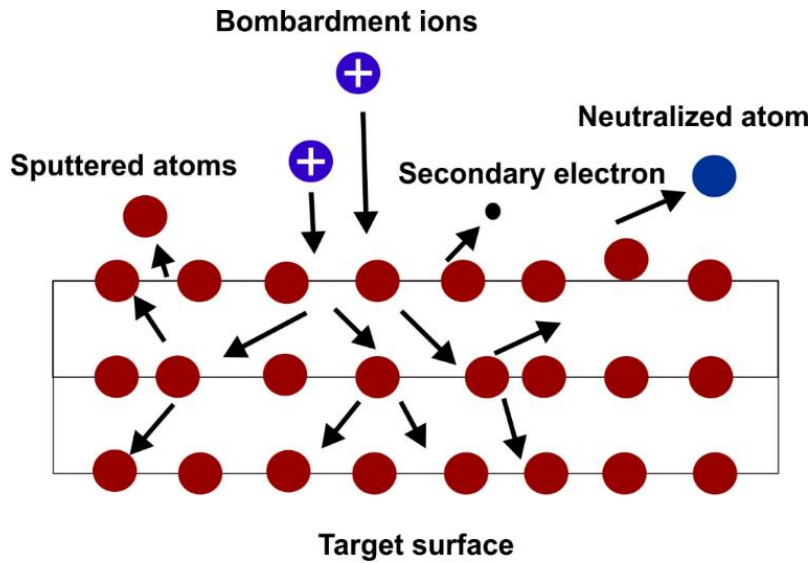


**Figure 2.3 Illustration of sputtering process from cross view. Blue particles are the bombardment ions and the red are target atoms. The black solid line shows the lattice planes of target material.**
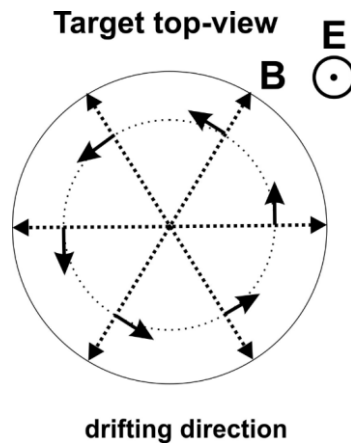


**Figure 2.4 Illustration magnetron sputtering: The top-view of magnetron. Secondary electrons are forced into the cycloidal orbits[34].**

One can characterize the sputtering process by the sputtering yield as in equation 2.2[33].

Here $Y$ is the sputter yield, $N_T$ is the number of ejected target atoms and $N_I$ is the number of incident bombardment ions.

$$Y = \frac{N_T}{N_I} \quad , \quad (2.1)$$

The sputtering yield depends on the energy regime of the bombardment ions[33], which is typically determined by the potential difference between substrate and cathode. At the low energy regime, the energy of the bombardment ions is lower than the binding energy of the target. Such ions can only sputter the loosely-bound atoms at the surface of the target and have a small sputtering yield of less than $10^{-2}$. At the medium energy regime, the ion energy is higher than the binding energy of the target, but still lower than the energy for ion implantation. The bombardment ions consequently can dislodge the surface and near-surface atoms and cause a series of collisions that result in the ejection of target atoms, which is shown in Figure 2.3. A typical sputtering yield of 0.1-3.0 is obtained for such energy regime and exhibits a linear relationship with the ion energy. For the high energy regime, which is typically higher than 1keV, the ions will be able to go to deep inside the target and cause deep-ion implantation. This causes a drop in the sputtering yield and is usually not adopted in normal sputtering deposition process for the benefit of cost-efficiency. A reference of surface binding energy can be found in reference 39. In practical experience, the medium energy regime is best for research and industrial applications.

For the deposition of insulating and metallic compounds, in many cases reactive sputtering deposition is preferred. The reactive sputter deposition starts from the sputtering of a pure metal target and is followed by the introduction of a reactive gas into the vacuum chamber in the presence of the inert gas. A list of compounds produced by reactive sputtering is shown in Table 2.3[40].

| Compounds | Gas | Examples |
|---|---|---|
| Oxides | Oxygen | $Al_2O_3$, $In_2O_3$, $SnO_2$, $SiO_2$, $Ta_2O_5$, $MgO$ |
| Nitrides | Nitrogen, Ammonia | $TaN$, $TiN$, $AlN$, $Si_3N_4$ |
| Carbides | Methane, acetylene, propane | $TiC$, $Wc$, $SiC$ |
| Sulfides | $H_2S$ | $CdS$, $CuS$, $ZnS$ |

**Table 2.3 Examples of compounds produced by reactive sputtering.**

In this project, DC magnetron sputtering was applied for the deposition of Ag thin film grating cathodes. Reactive magnetron sputtering was applied for the deposition of MgO thin film overlayers on Ag grating cathodes. And lastly, the evaporation method was applied in the deposition of Cs to activate the Ag cathodes for photoemission.

2.4 Oblique Angle Deposition (OAD) on Grating Patterns

A PVD based oblique angle deposition was applied later in the sample preparation of this project in Chapter 5. Different from the other methods such as lithography[41] or self-assembly[42,43] that are used to produce grating patterns, the OAD[44] adopts a large incident angle in the deposition of target atoms on an grating substrate. The large incident angle causes a so-called shadowing effect during the deposition and consequently alters the deposited grating profile. This is alteration in grating profile provides a way to enhance the plasmonic resonance on the metallic grating and thus can improve the quantum efficiency of the corresponding grating cathode. An illustration of the OAD mechanism is shown in Figure 2.5.
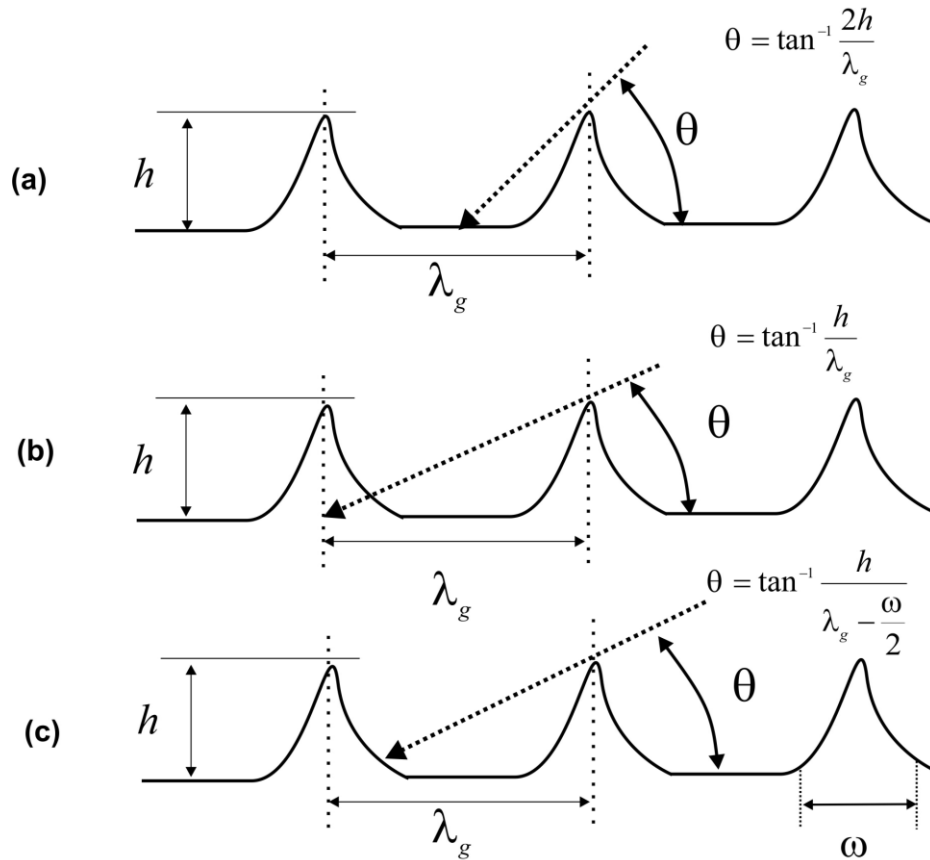
**Figure 2.5 Illustration of oblique angle selections with 3 different incident angles.**

In Figure 2.5, $\lambda_g$ is the grating periodicity and $h$ is the groove depth. $\omega$ is the grating

stripe width. $\theta$ is the complementary angle of the incident angle and it is in the plane that

is perpendicular to the grating stripes. At the very large incident angle of deposition atoms,

the grating groove is hardly coated because of the shadowing effect from the adjacent

stripe. Most depositions of target atoms occur on the stripe and cause an alteration of the

grating groove depth as well as width. A suitable deposition angle can be estimated as

shown in Figure 2.5. One possible estimation is as in Figure 2.10 (b), that the groove is

completely shadowed from the deposition atoms and almost all the atoms are

accumulated on the grating stripe. In this case, $\theta = \tan^{-1}\dfrac{h}{\lambda_g}$. For an angle $\theta$ that is

28

larger than this, the grating groove will be deposited as well. For an angle $\theta$ that is smaller than this, the stripe will show lack of coverage which might be undesirable in our case.  This serves as an upper limit estimate of the incident angle for the atomic flux.

Another estimation of this is as in Figure 2.5 (c), the angle $\theta = \tan^{-1} \dfrac{h}{\lambda_g - \dfrac{\omega}{2}}$ is suggested to ensure a complete coverage on the stripe and minimize the alteration of the width of stripe. However, Johnson *et al*[45]., found that the partially reflected atoms from the adjacent stripe play an important role in the film growth of shadowed side of the stripe. In such a geometry, the deposition from the reflected atoms could be excessive and alter the grating profile undesirably. Figure 2.5(a) shows another choice of deposition angle, where $\theta = \tan^{-1} \dfrac{2h}{\lambda_g}$. At such an angle, the target atoms can cover the center of the grating groove and will not enhance the grating groove very significantly. This can also ensure a full coverage of the substrate, which might be the most desirable for our project.

 If the deposition is only from one side, an asymmetric grating profile should be expected. OAD is typically used in combination with a rotational motor on the substrate holder to obtain a symmetric deposition.


2.5. Characterization Methods

2.5.1. Atomic Force Microscopy (AFM)

An atomic force microscope measures the force between the very top atoms of the tip of a cantilever and the surface atoms of the sample, as shown in Figure 2.6. As the tip scans along the surface, the cantilever "feels" the strength of the force that causes a deflection

on the cantilever. The initial design of the AFM involved the operation of Scanning

Tunneling Microscope (STM) that uses the tunneling current between the STM and

cantilever to measure the deflection. By maintaining a constant tunneling current[46], it

secures a constant force between the surface and the tip atoms. Most modern AFM

measures the cantilever deflection by optical detection, as shown in Figure 2.7. Such

optical deflection is typically realized by a red laser that shines on the cantilever. The

reflected beam is detected by a quadrant photodiode. By keeping a constant force through

implementation of a feedback system (PID), the tip follows the contour of the sample

surface and provides an image of the topography through the re-construction of the signal

in the software. The use of AFM provides a topography measurement of the surface that is

non-destructive. It is applicable not only to perceive the surface of conductive materials but

also insulators, which can't be readily accomplished using a STM.
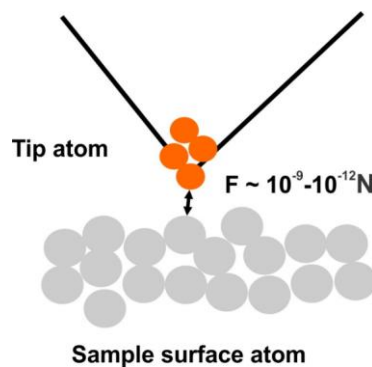


**Figure 2.6 Illustration of atomic force between sample surface atoms and tip atoms in an AFM.**

An example of the AFM composition is shown in Figure 2.9. The sample is loaded on the

sample holder above a piezo scanner. The piezo scanner is constructed by a piezoelectric

material that changes its geometry as a function of applied voltage. Typical piezoelectric

materials are $PdBaTiO_3$ or PZT[47]. The scanner is connected to a PID feedback control

loop to control the position of the sample surface.  When the distance between the tip and

sample surface varies, the cantilever deflection follows the variation. The PID will react and

adjust the piezo scanner position to keep a constant force between the tip and sample atoms. By scanning the sample surface with a raster scan pattern, the surface topography of the sample is obtained.
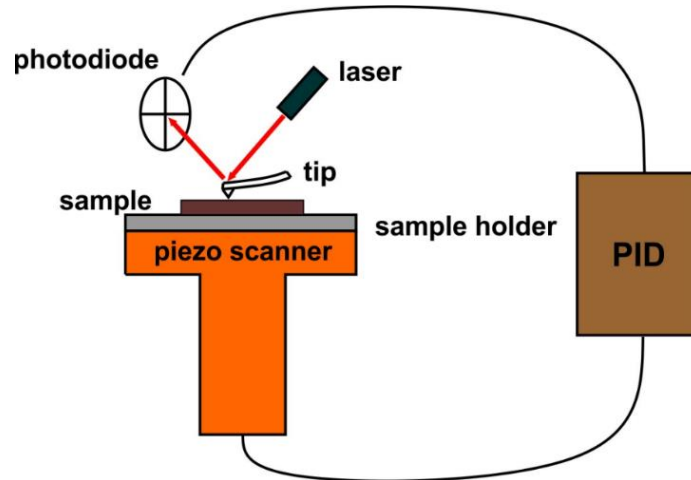


**Figure 2.7 An illustration of AFM operation system.**

2.5.2 Scanning Electron Microscopy (SEM)

Alternatively, the SEM uses an accelerated and focused electron beam to scan the surface of the sample. The electron beam is initially produced by an electron gun and accelerated between ~0.1keV and 50keV with beam diameter of 10 μm to 50 μm[48]. An electron gun is the equipment that provides stable and narrow electron beams. After going through a system of condensing lenses, the electron beam is focused to a much smaller beam crossover at the nanometer scale. After the condensing lenses, the electron beam is scanned by a deflection coil system that synchronizes with the electron beam in a cathode-ray tube (CRT). The electron beam will then go through the objective lenses and incident on the sample surface. Detectors for different electron-specimen interactions collect the signals and send them to the amplifiers and computer. The intensity of the CRT

is then adjusted by the detected signals drawn after the electron-specimen interactions and produce an image of specimen.

2.5.3. XRR (X-Ray Reflectometry)

X-ray reflectometry[49] is a technique that uses x-rays as a probe to retrieve sample information such as thickness, surface roughness, material density, etc. It is non-destructive and highly applicable to either crystalline or amorphous materials. For thin film samples, XRR can be used to measure the thin film thickness between 0.1nm to 1000nm and thus it can be used to calibrate the deposition growth rate of many materials.

Different from x-ray diffraction (XRD), the mechanism of XRR involves the constructive and destructive interference caused by the phase shift of reflected light at the atomic interfaces of the system. For X-ray wavelengths, the index of refraction n can be expressed as

$$n = 1 - \delta + i\beta \quad , \quad (2.2)$$

where $\delta$ has a magnitude of $10^{-5}$ for solids and a magnitude of $10^{-8}$ for air. $\beta$ is usually much smaller and has $10^{-1}$ or $10^{-2}$ of the magnitude of $\delta$, depending on the X-ray energy.

The critical angle for total external reflection of X-ray can be expressed as

$$\theta_c = \sqrt{2\delta} \quad , \quad (2.3)$$

For an incident angle below the $\theta_c$, the total external reflection will take place. The critical angle in XRR is often used to focus the x-ray beam. Note that the unit for equation (2.3) is in radians. The real part of the index of refraction is in proportion to the electron density of

the material. The critical angle is consequently in proportion to the square root of the real part of the electron density of the material. For a material with a higher electron-density, a larger critical angle is expected for the XRR measurement.

An illustration of the scattering geometry is shown in Figure 2.8. An incident x-ray with wave vector of $\vec{q}_i$ and reflected wave vector of $\vec{q}_f$ is shown. The momentum transfer in the z direction can be expressed as

$$q = \vec{q}_f - \vec{q}_i = q_z = 2k_0 \sin\theta \quad , \quad (2.4)$$

where $k_0 = \dfrac{2\pi}{\lambda}$, $\lambda$ is the wavelength and $\theta$ is as in Figure 2.8.
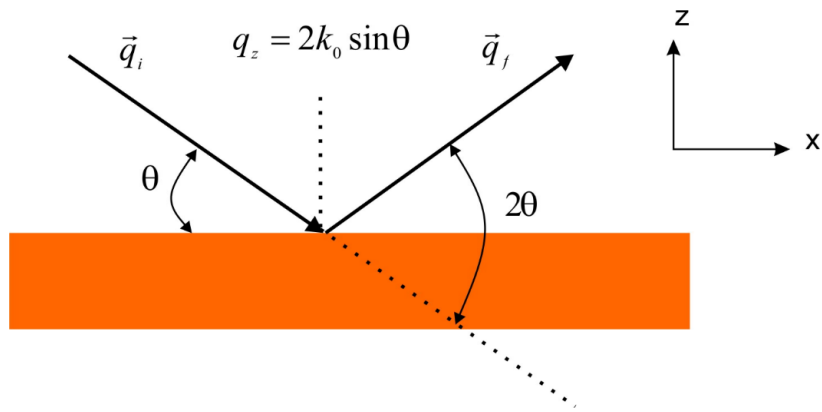


Figure 2.8 Illustration of scattering geometry for XRR.

The amplitude of reflectivity for a homogeneous and finite thickness slab in Figure 2.8 can be calculated as a sum of the reflected light between the top and bottom interfaces. By assuming the medium above and below the slab to be vacuum, the expression of the amplitude of reflectivity is

$$r_{slab} = \frac{r_{01}(1-p^2)}{1-r_{01}^2 p^2} \quad , \quad (2.5)$$

where $r_{01}$ is the amplitude of the reflectivity at the 0 and 1 interface, and where

$p^2 = \exp iq\Delta.$ $\Delta$ is the thickness of the slab. The intensity of the reflectivity $\left| r_{slab} \right|^2$

displays the so-called Kiessig fringes with the period of oscillation

$$P_Q = \frac{2\pi}{\Delta}. \quad (2.6)$$

This period can be used in the calculation of thickness from the measured fringe patterns.

In practical experience, the thickness, surface roughness as well as electron density for

the sample are obtained from fitting software provided with the XRR equipment and gives

a better analysis of the data than equation (2.6).

The roughness of the sample surface also affects the fringe patterns by decreasing the

reflected beam intensity exponentially. This is caused by diffused scattering on the

inhomogeneous surface of sample. This makes XRR very sensitive to the interface

roughness. The roughness of the sample interface is required to be smaller than 5nm[49] for

a good XRR measurement.

The XRR instrument that was used in this project is a PANalytical Empyrean series 2, as

shown in Figure 2.9. In addition to the application of XRR, it is also used to carry out XRD

measurements, which enables the identification of film components, lattice constants, etc.

Other technical information of this instrument can be found in reference 50.

**Figure 2.9 Instrument picture of PANalytical Empyrean series 2.**

2.6 Quantum Efficiency Measurement

2.6.1 Measurement Apparatus

The quantum efficiency (QE) measurement apparatus consists typically of an UHV system that can achieve a vacuum pressure of $10^{-11}$ to $10^{-12}$ Torr. Such a vacuum is sustained with the combined operation of pumps such as ion pump and non-evaporable getter pumps. The ion current serve as a good indication of the vacuum pressure in such system. A light source is required to excite the photoemission, such as a laser or a white light. A Faraday cup is positively biased (Figure 2.10(a)) by a DC power supply that is constructed from a series connection of 9V batteries. It is used to collect the electrons that are emitted from the cathode surface. A program written in LabView[51] was used to record the photocurrent

data. An RGA was also assembled into the vacuum system for the benefit of analysis of the gas molecules and leak testing.

Two choices of electrical configurations can be implemented, as shown in Figure 2.10. In Figure 2.10 (a), the Faraday cup is biased by a positive DC voltage and the cathode is grounded. It can also be configured with a negatively biased sample and the whole vacuum chamber serves as the Faraday cup for electron collection, as shown in Figure 2.10 (b). The electric potential difference between the Faraday cup and the cathode surface generates an electric field that is pointing from the Faraday cup to the cathode. As a result, electrons are attracted to the collector. The electron currents flow through the electric circuit and are measured by the picoammeter. In our project, we use the design as in Figure 2.10(a).
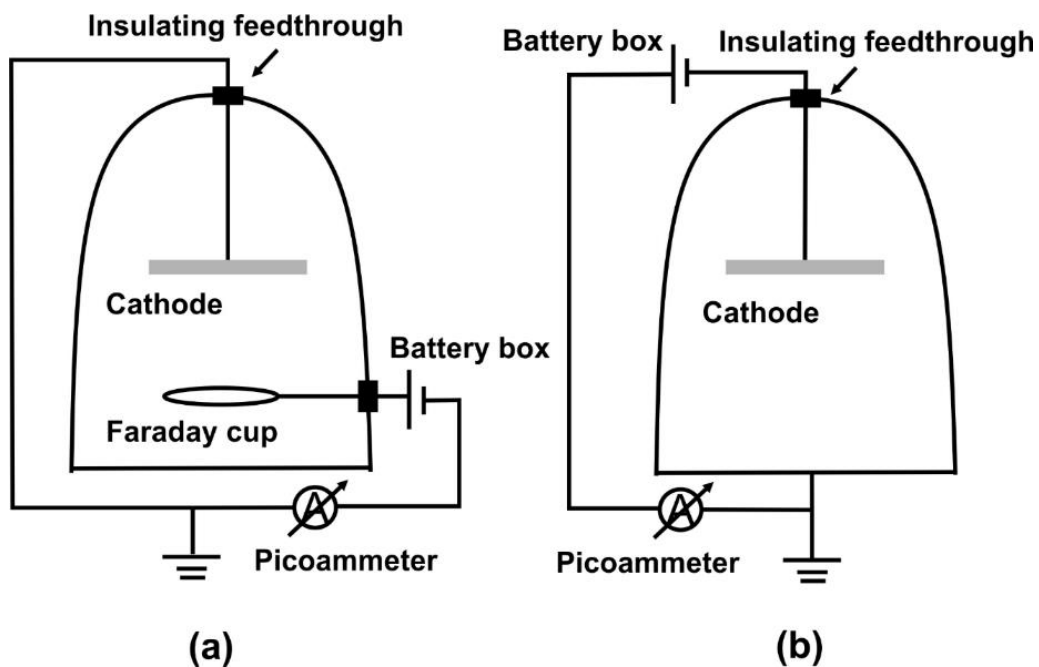


**Figure 2.10 The mechanism of the electron collection circuit: (a) Positively-biased Faraday cup and grounded cathode (b) Negatively-biased cathode and grounded chamber wall.**

A cesium filament is used to evaporate cesium on the silver cathode. Cesium is used to lower the work function of the photocathode by forming dipoles at the cathode surface,

which results in improvement in the resulting QE. A typical cesium dispenser can be obtained from SAES Getters. A typical working current starts from 4.5 to 4.7A[52] and heats the cesium atoms to above 600°C for evaporation deposition. Instead of the use of pure cesium to lower the work function, a reactive deposition of cesium and oxygen[53] can also be used for the same purpose through a so-called "yo-yo" deposition process. This includes the consecutive activation of cesium and oxygen molecules into the system and can produce the photocathode that has a longer life time and better QE[53].

In addition to the above apparatus, a setup for heating of the cathode is necessary for cleaning the cesium layer above the cathode surface. Cesium and cesium oxide desorb when heated up to some threshold temperature. Typically, a 266 °C baking temperature of 30 mins can sufficiently serve for cleaning purposes. In our setup, baking was implemented by the radiation energy from a light bulb below the cathode. The temperature of the cathode versus the working current of light bulb was measured by Jlab group and a typical working current of 4.0A was used to clean the cesium from the Ag cathode surface. For some setups, a circuit for pure nitrogen gas was used in the system to accelerate the cooling-down of the cathode. After heat cleaning, a very small amount of cesium was left on the cathode surface and resulted in a small photocurrent ~ 1nA.
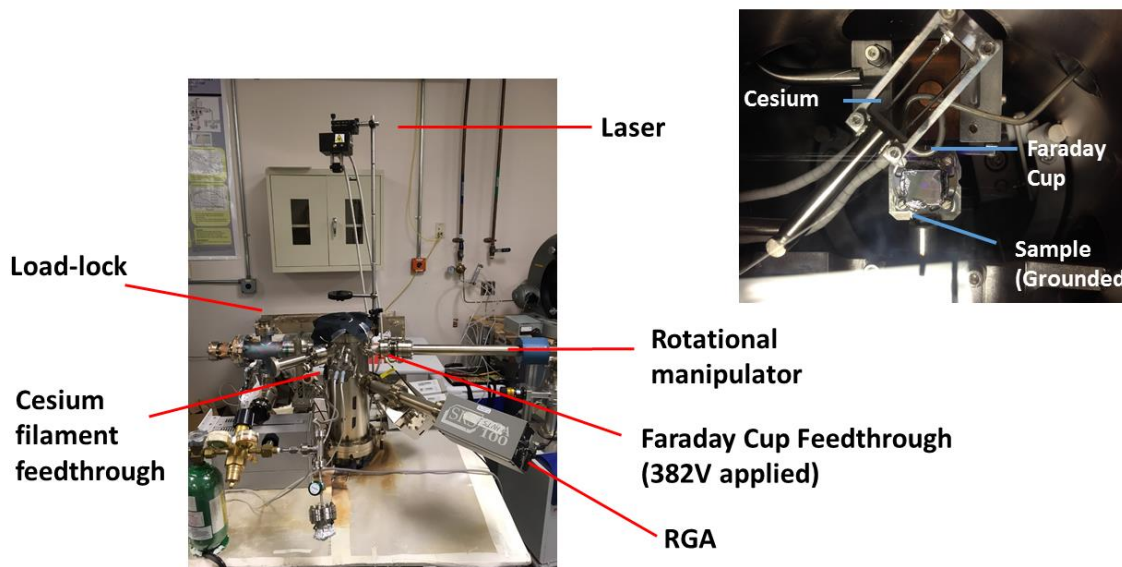
**Figure 2.11 Illustration of QE measurement system.**

The system for QE measurement which we used is shown in Figure 2.11. The Faraday

cup is positively biased with ~382V and the cathode is at ground potential. A conductive

silver paint was applied on the cathode surface to electrically conduct the cathode surface

with the aluminum support that wraps around the cathode. The aluminum piece was

grounded with the chamber. This forces the electric field to point from the Faraday cup to

the cathode surface and attracts the electrons to the collector. Oxygen is also released

from a leak valve when we attempted reactive deposition of cesium oxides. RGA was used

to analyze the gas-components in the vacuum chamber before and after the deposition

and leak testing.

2.6.2 Calculation of QE & Its Uncertainty

The calculation of the QE of a photocathode depends on the measurement of laser power,

laser wavelength, photocurrent and the power transmission rate of specific light, i.e. (laser

38

power at cathode surface after light goes through the top flange) / (laser power of the laser above the flange). The equation for the QE is

$$QE = \frac{hc}{\lambda} \frac{I}{\eta P} \quad . \quad (2.7)$$

Here, h is Plank's constant, c is the speed of light, $\lambda$ is the wavelength of the laser, $I$ is the photocurrent, $\eta$ is the transmission rate and $P$ is the power of the laser measured above the window.

To calculate the uncertainty of the QE, we use Δ to denote the uncertainty in each parameter. It is obvious that the measurements of $I$, $\lambda$, $P$, $\eta$ are independent of each other. If we assume a Gaussian distribution for each parameter, we can calculate the uncertainty of QE as

$$\left| \frac{\Delta QE}{QE} \right| = \sqrt{\left( \frac{\Delta I}{I} \right)^2 + \left( \frac{\Delta \lambda}{\lambda} \right)^2 + \left( \frac{\Delta P}{P} \right)^2 + \left( \frac{\Delta \eta}{\eta} \right)^2}. \qquad (2.8)$$

The uncertainty of QE and other parameters are displayed in Table 2.4.

| Laser (nm) | $\dfrac{\Delta I}{I}$ | $\dfrac{\Delta \lambda}{\lambda}$ | $\dfrac{\Delta P}{P}$ | $\dfrac{\Delta \eta}{\eta}$ | $\dfrac{\Delta QE}{QE}$ |
|---|---|---|---|---|---|
| 405 | 0.2% | 4.9% | 2.5% | 5% | 7.4% |

Table 2.4 Uncertainty for QE and other experimental parameters.

All our data on QE share an uncertainty of +/- 7.4%.

2.6.3 Space Charge

Space charge can appear when the potential difference between the Faraday cup and the cathode is low and this can depress the measurement results of QE. It can be described

by the Child-Langmuir Law which gives the space-charge limit current (SCLC) under a specific applied voltage and distance, as shown in equation 2.9.

$$J = \frac{4\varepsilon_0}{9} \sqrt{\frac{2e}{m_e}} \frac{V_a^{3/2}}{d^2} \quad , \quad (2.9)$$

where $V_a$ is the potential difference, and $d$ is the distance between Faraday cup and cathode surface, $e$ is the electron charge, and $m_e$ is the mass of electron, $\varepsilon_0$ is the vacuum permittivity.

In our setup, a 382V DC power supply is applied between the Faraday cup and ground potential. The distance between the Faraday cup and the cathode surface is ~ 2cm. An area of ~4 mm$^2$ is used in the calculation of the area that emits the electrons, which is based on the laser spot size. The SCLC is 1.37mA at such parameter. In our measurement, the photocurrent is maintained below 1uA, which is safely below this limit.

2.7. Plasmonic Measurement

2.7.1. Diode Laser

The system for powering the laser diode (LD) as well as for controlling the diode working temperature is shown in Figure 2.12. The specifications for the LD at 25$^0$ C are shown in Table 2.5. The LD is mounted on TCLDM9 that connects the diode with the LD working current controller LDC205C and LD working temperature controller TED200C. The LDC205C can control the LD current from 0 to 500 mA, and has an accuracy for the working current of $\pm$0.5 mA. A calibration of the working current as a function of the laser power is shown in Figure 2.13.

**Figure 2.12 Laser Diode system with LD mount TCLDM9, LD controller LDC205C and LD temperature controller TED200C[51].**
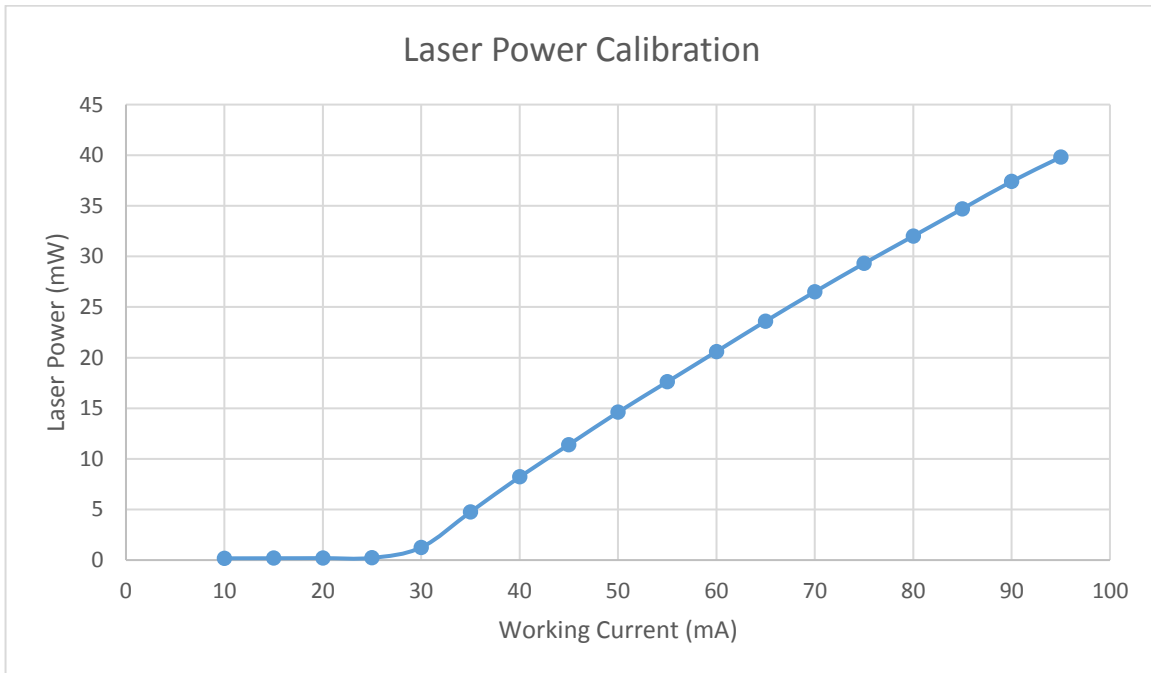


**Figure 2.13 Calibration of laser output power with working current.**

The TED200C can control the temperature from -40 °C to 100 °C, and has an accuracy of

±0.1 °C. For safety, an upper limit of 30mA was set in order to keep the power of the laser

below 1 mW.

| Parameter | | Condition | Min. | Typ. | Max. | Unit |
|---|---|---|---|---|---|---|
| Operating Temperature | | N/A | 0 | 25 | 75 | °C |
| Lasing Wavelength | | Po=40mW | 395 | 405 | 415 | nm |
| Beam Divergence | Perpendicular | | 16 | 19 | 23 | °|
| | Parallel | | 6 | 8 | 12 | |

**Table 2.5 Specifications of diode laser[54].**

2.7.2 Plasmonic Characterization by Measurement of Reflectivity

The earlier discussion of plasmonic resonances in Chapter 1 explained the concurrent

excitation of coherent behavior for the electrons near the surface of a metal grating. This

resonance is called the surface plasmon resonance, which can be observed through

measurements of the reflectivity at different incident angles. From equation 1.15, we note

that one can alter the incident light momentum at the surface varying the incident angle.

When the light momentum matches the requirement for excitation of SPR, the resonant

behavior will cause a complete transformation of light energy into electromagnetic energy

at the metal grating surface. As a result, the reflectivity at the resonance angle will display

a minimum. For angles that are away from the resonant position, the reflectivity follows the

diffraction efficiency of the grating. The measurements of reflectivity versus incident angle

can therefore identify the excitation of SPR. The resonance angle position and reflectivity

minimum are typical parameters that one should pay attention to. For the same grating

profile, the same resonance angle is expected. The reflectivity minimum can reveal the

strength of the plasmonic resonance indirectly. A deeper minimum can represent a better absorption of photon energy into the metal surface and near-surface atoms when transmission is negligible.

2.7.3 Reflectivity Measurement Apparatus

For the measurement of reflectivity, the samples were mounted on a rotational stage in a custom-built high-precision goniometer system. Each sample was mounted such that the grating grooves were normal to the incident plane of light. A p-polarized blue diode laser ( $\lambda = 405\text{nm}$ ) was modulated with a 255 Hz optical chopper mounted in the path of the illuminating incident beam, and the incidence angle was varied within the chosen regime, usually with an angle step size of $0.5^\circ$. A Si photodetector (Thorlabs DET10A) and a lock-in amplifier from Standard Research Systems (SR510) were used to measure the zero-order reflected beam. The sample surface was aligned near the center of rotation to ensure optimal measurements in the same region of the sample surface at all angles. A schematic illustration of the optical SPR setup is shown in Figure 2.17.
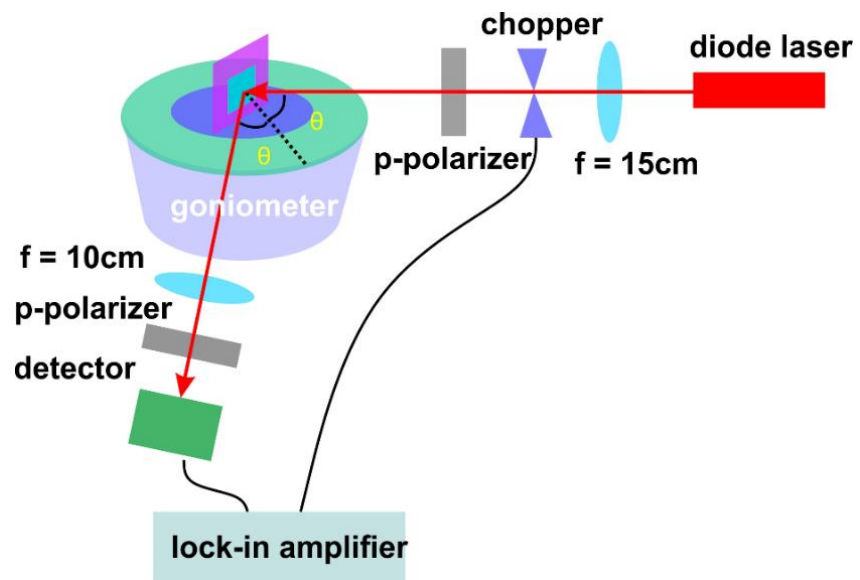
**Figure 2.14 An illustration of SPR setup for reflectivity measurement that is used to characterize the SPR performance.**

# Chapter 3 Lowering the Work Function of Ag Cathodes by MgO

The work function is the minimum photon energy required to liberate an electron from a metal surface via the photoelectric effect. In what follows, the effect of MgO overlayers on silver surfaces to that end will be discussed.

3.1 MgO on Ag (001)

The approach of growing oxide thin films on metal has drawn much attention because of their potential in magnetic tunnel junctions, high-k dielectric in electronic devices and as a support material in nanocatalysts[55-60], and in a wide variety of other applications. Studies of the characterization and preparation of such layered systems have been carried out for more than 20 years[61,62]. It has been reported that there is a substantial change in the work function of silver caused by a top magnesium oxide layer[63]. This opens the opportunity to study such an oxide/metal interface for the present application.

Traditionally, the Schottky model is used to explain the electronic structure of a metal-dielectric interface, where the main assumption is the absence of interactions between the metal and the dielectric material. When the metal/dielectric interface is formed, thermal equilibrium is required. Thus, the Schottky barrier height (SBH) $\xi$ is defined as the difference between the metal work function $\Phi_m$ and the gap width $E_g$ of dielectric material[64].

$$\xi = E_g - \Phi_m \qquad (3.1)$$

An illustration of such an energy barrier is shown in Figure 3.1[64].
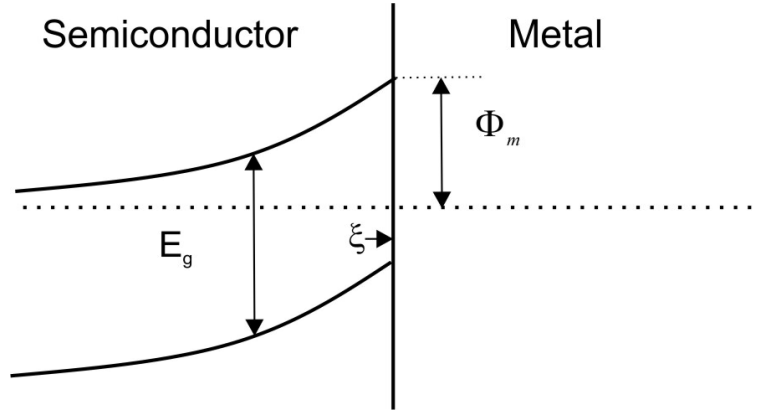
However, the Schottky model is generally not observed in many experimental results.

Heine[64] pointed out that surface states at the metal/dielectric interface can exist because

of the decay of the metal wave function into the dielectric. This gives rise to metal-induced

gap states (MIGs)[65-67], which have been invoked to understand SBH for various

metal/dielectric interfaces.

In particular, Livia[68] calculated the work function of oxide/metal combinations in four

different systems using density function theory (DFT). This includes the interfaces of

MgO/Ag(100), MgO/Mo(100), $TiO_2$(100), and $SiO_2$(112). Table 3.1[68] lists calculations

including charge transfer (CT), adhesion energy, surface dipole, system work function $\Phi_m$,

and work function shifts from the bulk metal $\Delta\Phi$. In these calculations, MgO lowers the

work function in metal substrates by 1- 2eV. At the same time, the charge transfer is found

to be relatively small. This is in contrast with $TiO_2$ and $SiO_2$ systems whose charge transfer

is ~5 times that of MgO systems. Note that the calculation of the Ag (100) work function is

4.3 eV, and the relevant experimental measurement result is 4.22 eV. The changes in the

work function of the MgO/Ag (100) and MgO/Mo(100) systems exhibit the same trend, i.e.

an overall decrease from the metallic work function. The growth of the first monolayer

displays a significant effect of this decrease. Further increasing the thickness of MgO

shows only a negligible influence on the work function of MgO/metal systems, including MgO/Ag(100) and MgO/Mo(100).

The shift in the work function is explained by the change of the surface dipole that can be caused either by charge transfer (CT) or induced polarization effects at the interface[69]. Livia[68] points out that for the MgO/metal system, charge transfer is insufficient as the main cause of the surface dipole change, because of the negligible amount of charge transfer. Livia further proposed that induced polarization is the main cause for the work function change in MgO/metal systems, resulting from charge compression at the interface, which has been found in atomic or molecular adsorbates on metal surfaces [70-72]. The interface causes a reduction of the surface electron density overspill and consequently changes the interface dipole, which is shown in Figure 3.2b[73]. The charge compression effect is important for highly ionic materials. Conversely, for non-ionic dielectrics that form chemically-bonded interfaces, charge transfer is a dominant contribution to the surface dipole, as shown in Figure 3.2a. In general, charge transfer and compression effects may work together and result in either an additive or a subtractive effect on the work function.

Experimental measurements of the work function on MgO/Ag(100) have also been carried out together with topographic studies of the system. Konig, et al.[74] have applied three independent methods *in-situ* to measure the work function of the MgO/Ag(001) system with 0.5ML, 3ML and 8ML MgO thicknesses. These methods include Kelvin probe force microscopy to measure the contact potential difference (CPD), and the exponential dependence of the tunneling current *I(z)* as well as the field emission resonances (FER). Images of surface topography were obtained in-situ from Scanning Tunneling Microscopy (STM).[74]
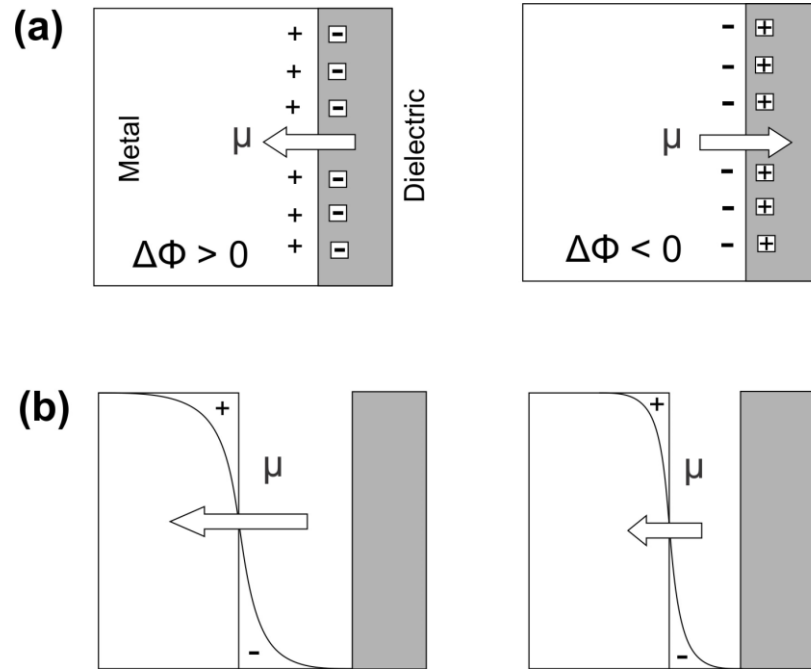
**Figure 3.2 Mechanisms of change on surface dipole: (a) charge transfer at the interface (b) compression effect of surface electron density for highly ionic materials[73].**

| Model | Number of Layer | Surface Dipole (e/Å) (x10³) | Adhesion Energy/S (eV/Å²) | Charge Transfer/S (e/Å²) (x10²) | $\Phi m$ (eV) | $\Delta \Phi$ (eV) |
|---|---|---|---|---|---|---|
| MgO/Ag(100) | 1L | 5.3 | 0.031 | 1.02 | 3.29 | -1.01 |
| | 2L | 6.5 | 0.022 | 0.54 | 3.10 | -1.20 |
| | 3L | 6.4 | 0.023 | 0.55 | 3.12 | -1.18 |
| MgO/Mo(100) | 1L | 9.7 | 0.153 | 1.61 | 2.52 | -1.67 |
| | 2L | 11.8 | 0.135 | 0.90 | 2.05 | -2.14 |
| | 3L | 11.8 | 0.136 | 0.93 | 2.05 | -2.14 |
| TiO2/Mo(100) | 1L | -1.6 | 0.167 | -5.19 | 4.35 | +0.20 |
| | 2L | -6.2 | 0.093 | -6.13 | 5.19 | +1.04 |
| | 3L | -7.0 | 0.174 | -5.73 | 5.34 | +1.19 |
| SiO2/Mo(112) | 1L | -1.1 | N/A | -5.87 | 4.69 | +0.42 |
| | 2L quartz | -4.5 | N/A | -5.93 | 5.30 | +1.02 |

**Table 3.1 Calculation results of oxide/metal systems with charge transfer, work function and shifts on system work function[68].**

Experimental measurements from three independent methods and the comparison with

theoretical values are shown in Table 3.2 (extracted from reference 74). The experimental

results for different thickness of MgO agree with the calculations and show the same trend

of lowering the work function of the metal. The work function of thicker MgO on Ag(100) also follows a similar trend decreasing the silver work function, which was predicted in the DFT calculations.

| Number of MgO layers on Ag (100) | Theory | Experiment | | |
|---|---|---|---|---|
| | $\Delta\Phi$ (eV) | CPD $\Delta\Phi$ (eV) | I(z) $\Delta\Phi$ (eV) | FER $\Delta\Phi$ (eV) |
| MgO island | -0.94 (calculated for 1ML) | -0.5 | -2.0 | -1.2 |
| 3 | -1.27 | -1.1 | -1.4 | -1.4 |
| 8 | N/A | -1.1 | -1.2 | -1.3 |

Table 3.2 Theoretical and experimental results for 0.5ML, 3ML, 8ML MgO on Ag(001)[74].

Further investigation on the MgO thickness effect on the work function was carried in the experiments by T. Jaouen et al[75]. Jaouen used ultraviolet photoelectron spectroscopy (UPS) to measure the work function of MgO layers with thickness ranging from 2 to 12 monolayers (ML) on Ag (001) as shown in Figure 3.3[75]. The work function was ~ 3.05 ± 0.05 eV from 2ML to 5ML and rose to ~3.3 ± 0.05 eV from 8ML to 12ML. The difference in the work function, despite the big range of thickness considered, is comparatively small. At 8ML and 12ML, the difference in the work function is ~1.1eV and corresponds to a deposition of 3.3 nm to 5 nm MgO on Ag (001).
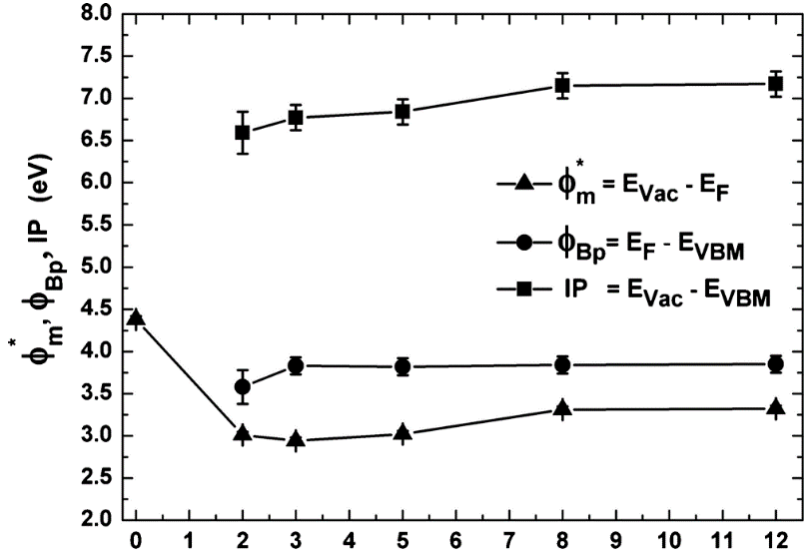
**Figure 3.3 The experimental results of work function measurement of MgO(NL)/Ag(001) systems. Solid triangle data points: work function; solid round data points: the p-type Schottky barrier height(SBH); solid square data points: ionization potential (IP) [75].**

In constrast, Polycrystalline Ag has a reported work function of ~ 4.26 eV[76].

Photoemission from a pure silver surface would therefore require photons in the ultraviolet region of the spectrum. Although there have been many studies on the work function of MgO/Ag(001) systems, as well as other crystalline orientations, there are no significant reports on the work function for MgO/Ag polycrystalline systems, which would be useful for our studies. In any case, for the present work, we sputter-deposited polycrystalline silver coatings onto thin film polycarbonate grating substrates, hoping that by thereafter depositing very thin layers of MgO over such polycrystalline Ag films, we might observe a significant lowering effect in the work function. This would provide an opportunity to create efficient photoemissive silver-based cathodes that would operate in the visible (blue) region, where powerful short-pulse lasers are more readily available.

3.2 Experimental MgO/Ag/Grating Photocathodes

3.2.1 Sample Preparation

Commercial polycarbonate substrates (made from DVD) were loaded in the thin film deposition system and deposited with 50nm Ag coatings under an environment of Ar of 7.5 E-3 Torr. The Ag surface was then *in-situ* coated with MgO for layer of 2 nm, 5 nm and 10 nm, respectively, using DC magnetron reactive sputtering of magnesium and oxygen-enriched environment.  The Ar pressure for such deposition was 4.5 E-3 Torr and oxygen pressure was added by 0.1 E-3 Torr.

3.2.2 Reflectivity Measurement

Measurements of reflectivity on each sample, as well as from a bare Ag deposition on a similar grating substrates, is shown in Figure 3.4 for comparison. The reflectivity measurement was taken at a 0.5° resolution. Reflected beam intensity is detected by the silicon detector and recorded by the output voltage level. The reading of the voltage was truncated from the smallest stable digit available, which is at 0.01V. The reflectivity measurements in Figure 3.4 shows that the resonance is excited when the incident light angle is ∼ 25°.
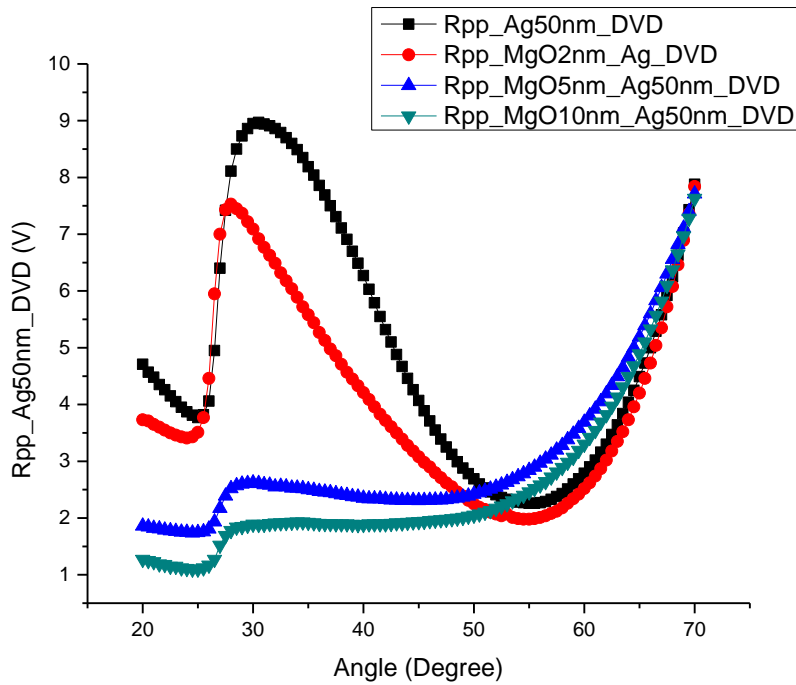
**Figure 3.4 Reflectivity measurement on different thickness of MgO on Ag50nm grating samples. Black: bare 50nm Ag grating; Red 2nm MgO on 50nm Ag grating; Blue: 5nm MgO on 50nm Ag grating; Green:10nm MgO on 50nm Ag grating. The plasmon resonance is extracted at ~25°.**

The existence of MgO has a damping effect on the intensity of the plasmonic resonance as we discussed in chapter 1. As the thickness of MgO grows, the resonance is reduced. The largest drop of intensity occurs between thicknesses of 2nm MgO and 5nm MgO. A large reduction of the associated electric field at the interface of the silver metal is also expected at MgO thicknesses from 5nm and above. We note that Jaouen's report[75] on the work function for MgO thickness from 2ML to 12ML shows a consistent work function reduction for the Ag(001). Although we can't conclude that the MgO thickness will have the same exact effect on polycrystalline Ag, it seems reasonable to keep the MgO thickness at very thin levels.

3.2.3 Photoemission measurements

Photocurrent measurements were taken under a vacuum pressure of $10^{-8}$ Torr using a (blue) laser at 405 nm.The data for a MgO2nm/Ag50nm/grating sample are shown in Table 3.3. This includes the current without the laser shining on the grating cathode (noise) and the measurements with laser on.  The data were taken at different times for consistency checks. For a MgO/Ag planar cathode, the quantum efficiency at 266nm (4.66 eV) has been reported as ~ 0.01% to 0.06%. For a 1 mW and 405 nm (3.05 eV) laser light, the expected quantum efficiency would be much smaller if substantial lowering of the work function were not successful.

| Data Set 1 (nA) | | Data Set 2 (nA) | | Data Set 3 (nA) | | Data Set 4 (nA) | |
|---|---|---|---|---|---|---|---|
| Laser Off | 3.832 | Laser Off | 4.234 | Laser Off | 3.849 | Laser Off | 3.849 |
| 1 | 3.829 | 1 | 4.234 | 1 | 3.849 | 1 | 3.850 |
| 2 | 3.830 | 2 | 4.234 | 2 | 3.849 | 2 | 3.849 |
| 3 | 3.832 | 3 | 4.234 | 3 | 3.849 | 3 | 3.851 |
| 4 | 3.832 | 4 | 4.234 | 4 | 3.848 | 4 | 3.848 |

**Table 3.3 Photocurrent measurement results on MgO2nm/Ag50nm/grating with different attempts and noise measurement.**

To prove the existence of photoemission current, a noticeable difference between the noise and the signal is required. Our measurements in Table 3.3 haven't shown a good proof of photo-electron emission. The current level is almost the same as the noise current

with a very slight difference of ~3pA at most in Data set 1. The high level of noise current (3~4nA) compared to the possible level of photoelectron current (<nA) makes it very hard to identify a real photoelectron current. One possibility is that the MgO deposition on the grating structure of silver did not accomplish significant reduction of the work function of Ag due to incomplete coverage or perhaps non-uniform conformal deposition. A possible remedy for this is to choose a higher photon energy laser or change the cap layer for a more efficient one to lower the work function of silver and to achieve better signal to noise results. We have followed the latter path and considered alternative cap-layers discussed in next chapters.

However, it is beneficial to bring attention to the recent successful measurement of QE on MgO/Ag(100) system by T. Droubay[77]. By using a continuous-wave (CW) laser at 266 nm (4.66 eV), they measured the photoemission of planar 3MLMgO/Ag(001) to be 7 times greater than forclean Ag(001). This makes the measurement of QE on 3MLMgO/Ag on grating structure system at such wavelength of laser light a promising path to follow.

# Chapter 4 Normal Deposition Silver Grating Cathodes

4.1 Planar Silver Cathode

Beginning with this chapter, we will focus on the study of Ag grating cathodes with evaporated cesium (Cs) overlayers, which have been widely used to lower the work function in metals[78,79]. A 100 nm Ag film was deposited on a planar bulk polycrystalline aluminum (Al) substrate in at 7.5x10$^{-3}$ Torr of Ar by DC magnetron sputtering deposition.

The activation of the cathode includes the evaporation of Cs onto the surface. A 405 nm laser is incident on the sample at 0° to monitor the photocurrent change during activation. The quantum efficiency (QE) results after activation are shown in Table 4.1 for three different laser powers.

|  | 1 | 2 | 3 |
|---|---|---|---|
| Laser Power (mW) | 3.5 | 1.38 | 1.47 |
| QE (%) | 0.0873 | 0.12 | 0.123 |

Table 4.1. Quantum efficiency of 100 nm Ag/Al cathode with different activation laser powers.

The QE values are in agreement with the result of A. Balter[80], who gives a QE of ~0.1% for Cs/Ag at 405 nm. It is interesting that the laser power may have an effect on the QE value. For similar laser powers of 1.38 and 1.47 mW, the resulting QE is 0.12% and 0.123%, respectively. For a higher laser power of 3.5 mW, the QE is much smaller – only 0.0873%, about 37% smaller than at the other two values. This effect is also found to be true for the QE of grating cathodes when measured at normal incidence. However, this effect is not because of the existence of space charge, since our photocurrent is safely below the limit.

56

All the uncertainties in the measurement of Table 4.1 can be referred in section 2.6.2. The QE has a systematic uncertainty of 7.4% (section 2.6.2).

4.2 Normal Deposition (ND) Ag50nm/grating

50 nm of Ag was grown on a diffraction grating from Edmund Optics, which consists of a glass grating with a commercially-deposited layer of Al on top of the sinusoidal surface. These same substrates were used as substrates for the QE measurements discussed in Chapter 5. The film was deposited in $7.5 \times 10^{-5}$ Torr of Ar at room temperature. The sample was then taken to to atmosphere and transferred to the UHV QE measurement system at Jefferson Lab. Note that a very thin layer of AgO was expected to appear on the cathode surface due to the transportatin atmosphere. Other adsorbates on the surface may have appeared as well for the same reason.

4.3 Topography Measurements

Topography measurements for the substrate grating are shown in Figure 4.1(a). The grating was scanned by a non-contact atomic force microscopy (AFM) over a 5x5 $\mu m^2$ scan. The sample was placed with the stripe direction close to the horizontal scan direction to avoid possible error in the grating groove measurement that might be caused by the extreme up-and-down movements of the tip. In the direction perpendicular to the grating stripe, a line-scan was extracted from the topography to determine the periodicity and grating groove dimensions (Figure 4.1(b)). The measured average periodicity for the grating is 488.2 nm, and the groove depth is 209.3 nm. The standard values of grating parameters can be found in Table 4.2
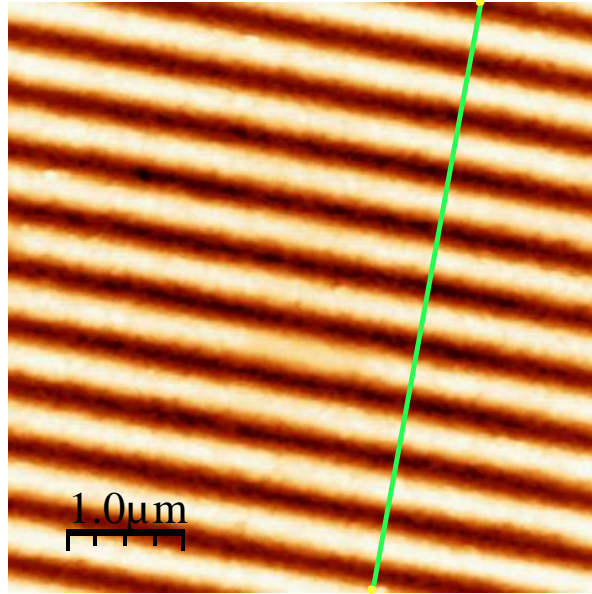
**Figure 4.1(a). Topography measurements showing grating structure of bare grating.**
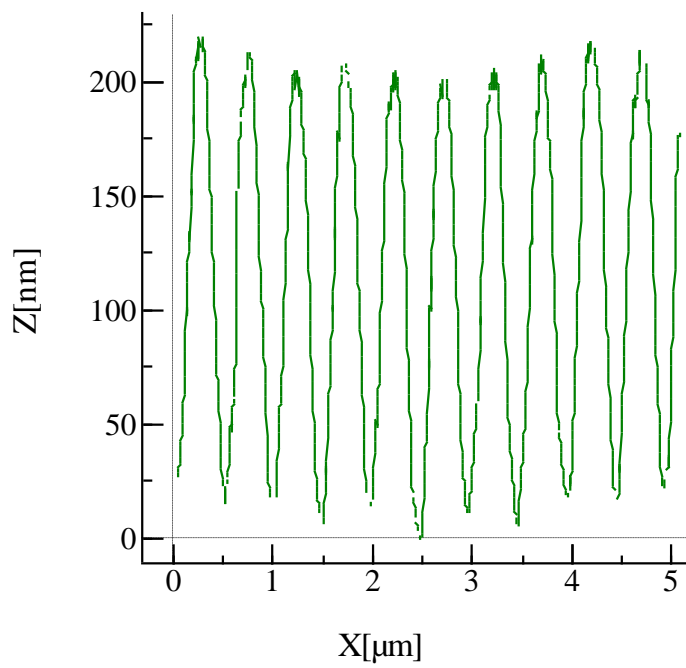


**Figure 4.1(b). Line scan extracted from topography of the substrate grating.**

| Grating Profile | Periodicity(λ) | Groove Depth(h) |
|---|---|---|
| Sinusoidal | 555nm | 201nm |

Table 4.2. Diffraction grating substrate standard description.

Topography measurements and a line-scans taken after the deposition of 50 nm of Ag on the same type of grating substrate are shown in Figure 4.2(a) and Figure 4.2(b). A full coverage of Ag on the grating substrate can be seen in Figure 4.2(a). As it is shown, the deposited Ag follows the grating structure of the substrate, i.e. it is conformal. The average periodicity and groove depth are 525 nm and 205 nm, respectively. The periodicity measurement shows a small change of approximately 7% from the substrate, and the grating groove depth is almost the same as the substrate.
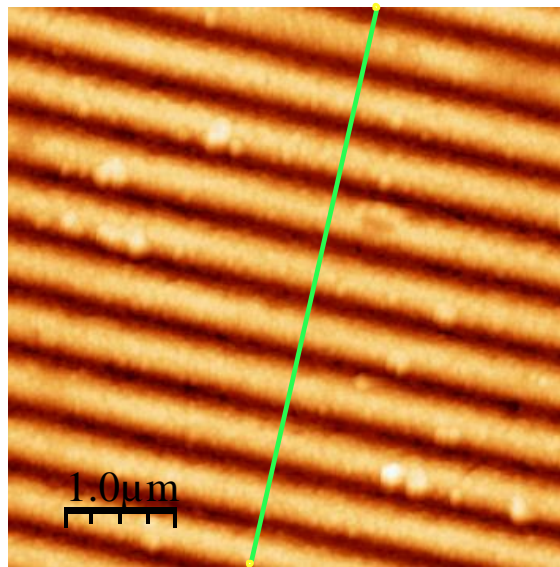


Figure 4.2(a) Topography of 50 nm Ag/grating.

## 4.4 Reflectivity Measurement

Reflectivity measurements were carried out on the 50 nm Ag sample to observe its plasmonic resonance performance. The result is shown in Figure 4.3.Two resonance positions are found in the reflectivity measurement. One is at 14.5° and the other is at 25°. If a plasmonic effect on the QE exists, then a maximum in QE at these angles should be observed.
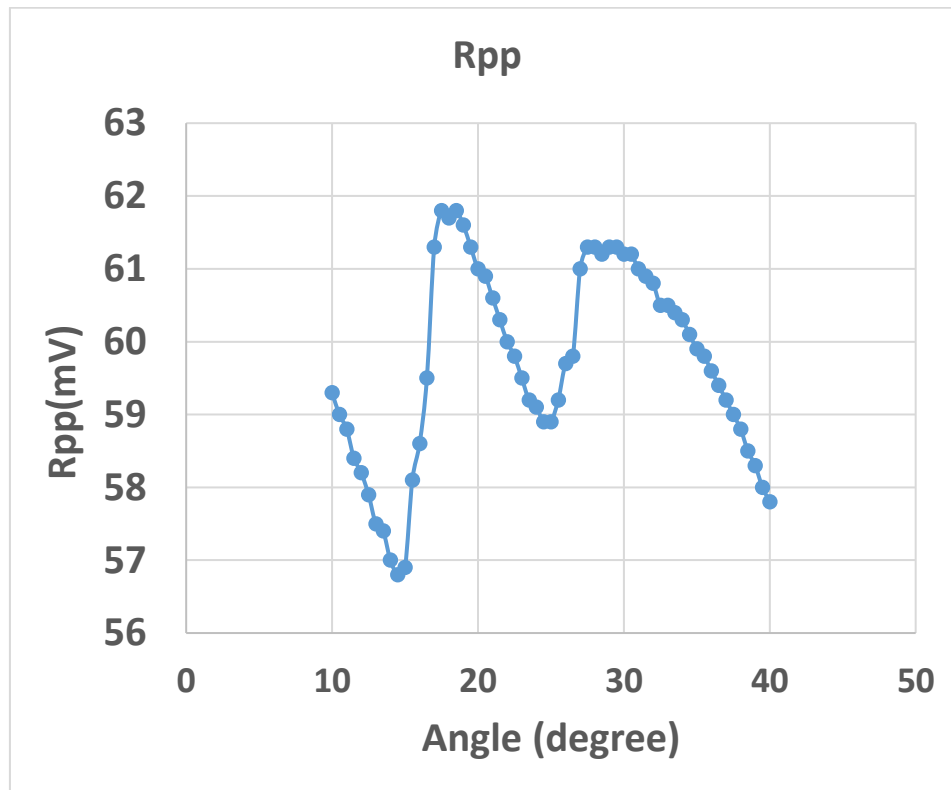
**Figure 4.3 Experimentally-determined reflectivity of the 50 nmAg/grating sample.**

## 4.5. Quantum Efficiency Measurement

### 4.5.1 Overview

The 50 nm Ag/grating sample was placed on a sample holder and held in place with a thin aluminum sheet that was mechanically wrapped around the holder. Silver paint[81] was applied to electrically connect the surface of the cathode to the aluminum wall and ultimately to the grounding potential. A picture of sample and sample holder is shown in Figure 4.4. The purple color is the 405 nm light reflected from the cathode surface and is not the color of the cathode material.

One can observe that the cathode surface has a "whitish" contamination. This is found

after a baking process at 200°C carried out on the chamger, which releases water and

other gas molecules stuck in the walls from the system and to be pumped way from the

vacuum chamber so that it will ultimately reach the UHV environment needed for cathode

activation. As we discussed in Section 4.2, the cathode surface was open to the

atmosphere for a short time, so it is quite possible that adsorbates on the cathode surface

have reacted with the released gas molecules to form contaminants on the cathode

surface. This contamination could lower the lifetime of the cathode significantly, but one

can reduce the contamination by improving the chamber baking process and have it

carried out ata lower temperature and for less time. Thus, we reduced the temperature

from 200°C to less than 150°C and the time from 72 hours to 18 hours and found a visibly

noticeable difference in the sample appearance. An example of a cathode surface that

was baked under the new conditions is shown in Figure 4.4(b). The lifetime of this cathode

increased from less than 20 hours to 49 hours with laser light on. The lifetime is the time it

takes when QE falls from the maximum of QE to its 1/e. This 150°C chamber baking temperature was applied to all later samples.
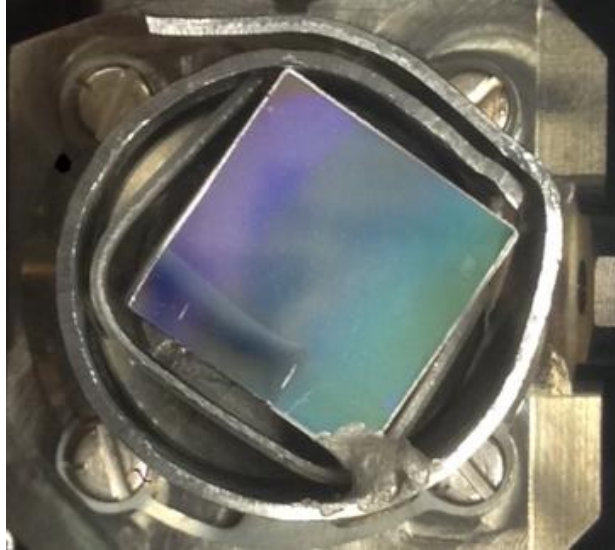


Figure 4.4(b) Cathode on sample holder after chamber baking at 150°C.

The sample holder is mounted on a rotational fork, which can move the sample in either the longitudinal or the transverse direction. The ability to rotate the sample in the transverse direction is critical for our studies, as we are looking at the angular dependence of the QE for this grating cathode.

One technical difficulty in precisely measuring the angular dependence of the QE lies in the positioning of the sample above the rotational center of the sample holder. Figure 4.5 shows the problem in detail. The design in the QE measurement system has aligned the sample holder with the rotational center, but the sample is placed above the sample holder on a 6 mm-thick substrate. This creates a limitation on the available angular range in the transverse direction. In Figure 4.5, when the sample is rotated, the surface of the cathode moves away from the original incident light spot. As the degree of rotation increases, the incident light will reach close to the edge of the cathode. The maximum incident angular

range is from $0^0$ to approximately $33^0$. Consequently, the actual QE measurements will include the possible effect of an uneven distribution of Cs in the transverse direction, since the incident light travels across the cathode surface. However, the incident angles should not be affected much because of the parallel edge of the rectangular shaped substrate. In our experiment, the angle positions are recorded as absolute values, which were shown on the scale in the magnetic manipulator. This absolute angle position can change after changing the sample in the loadlock, which can be seen at Table 5.3(a). However, relative angles are more important to us, which represents the incident angle for the laser on cathode surface.
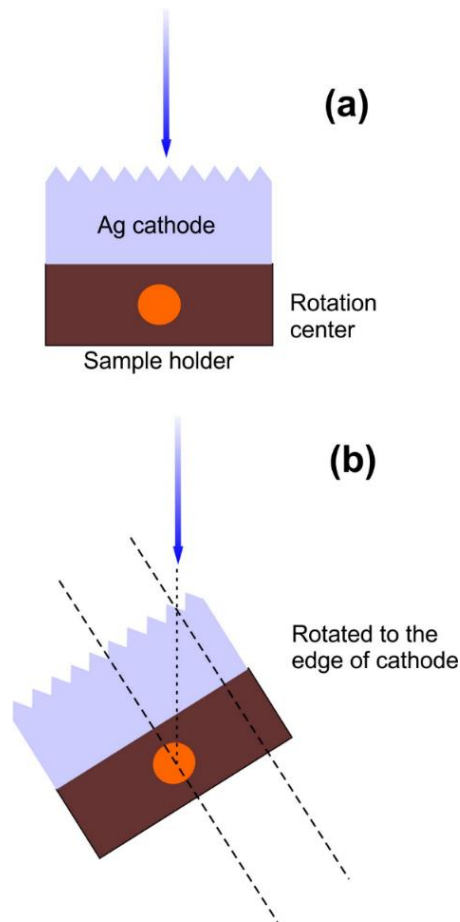


**Figure 4.5. (a) Illustration of the direct incident beam and the different position of cathode surface and rotational center. (b) Illustration of the limitation on the measurable angle in the transverse direction due to the displacement of the sample from the rotational center.**

64

4.5.2 Activation with Cesium

Cs is deposited on the 50 nm Ag/grating sample to lower the cathode work function. A Cs filament from SAES Getters is connected to a DC power supply to provide a current of 4.7 A for the evaporation deposition. A 405 nm light is incident at the cathode surface for the activation process, and the power of the laser was kept very small (~11.2 µW) to benefit the cathode lifetime. In a traditional activation on a GaAs photocathode, the QE performance will reach a maximum when a monolayer of Cs is formed on the cathode surface[53]. Further deposition of Cs will then increase the work function of the system and thus lower the QE. However, it is not the same in our case on a Ag cathode. The deposition of Cs on the Ag grating cathode is found to increase the QE initially and reach a plateau where further addition of Cs does not affect the QE. The formation of contamination on the Ag surface when the cathode is exposed to atmosphere may have caused this effect.

4.5.3 Quantum Efficiency

Photocurrents are excited by an incident 405 nm light on the cesiated grating cathodes. During the Cs activation, the cathode surface is placed horizontally with a 405 nm laser incident at close to 0° on the cathode surface. As the Cs accumulates on the Ag surface, a photocurrent starts to appear and is measured by a picoammeter. This photocurrent eventually reaches the maximum plateau with little increase where further deposition of Cs does not affect the QE performance. This was observed on all silver grating samples. At this point, the Cs deposition is stopped and the QE is measured on the activated cathode. Several positions are chosen longitudinally along the rotational axis to take QE measurements in order to find an average value (Figure 4.6). At each longitudinal position, one can find multiple maximum or minimum values as one rotates the cathode in the

transverse direction (Figure 4.6). Some of these are relative maxima or minima, rather than absolute one. Table 4.3 shows a set of data for four longitudinal positions with their maximum and minimum.
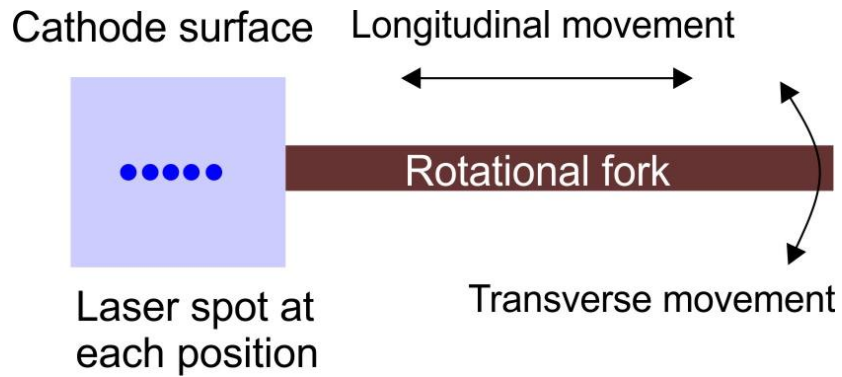


Figure 4.6 Illustration of 5 positions in the longitudinal direction.

| | Position 1 | | | Position 2 | | | Position 3 | | | Position 4 | | | Average |
|---|---|---|---|---|---|---|---|---|---|---|---|---|---|
| QE | Max | $145^0$ | 0.367 | Max | $144^0$ | 0.366 | Max | $144^0$ | 0.345 | Max | $144^0$ | 0.361 | 0.360 |
| (%) | Min | $123^0$ | 0.306 | Min | $123^0$ | 0.304 | Min | $121^0$ | 0.285 | Min | $121^0$ | 0.307 | 0.300 |
| Δ (%) | 19.9% | | | 20.4% | | | 21.1% | | | 17.6% | | | 19.8% |

Table 4.3 QE of a Cs/Ag/grating cathode at four longitudinal positions, and increase Δ (%) between max and min.

The measurement of QE after the initial activation of the cathode is shown in Table 4.2. This includes the absolute maximum and minimum found at four different longitudinal positions, which are at least 1 mm or more separate from each other. One can see that there is an average increase of 19.8% from the absolute minimum QE to the maximum

QE. This increase in QE is calculated as in Equation (2.7). Note that the angular rotation has an uncertainty of ~2 degrees.

The angle positions of the absolute maxima of QE for five consecutive longitudinal positions agree well with each other. The absolute maximum appears when the cathode rotates to 144~145$^{o}$ on the angular scale. The measurement of QE at such positions also show similar results and gives an average of 0.36% for the maximum QE. Similar behavior was also seen for the absolute minima. At an angular position of around 122$^{0}$, the minima of the QE appeared with an average value of 0.3%. Specifically, the maximum QE at position 1 is ~0.367%.  The QE values at position 3 are lower than those at other positions - it has a maximum value of 0.345% and minimum value of 0.285%. This difference of QE distribution in the longitudinal direction may indicate the existence of a slightly uneven Cs deposition on the cathode surface.

Re-activation of the cathode after heat cleaning was carried out in order to make more detailed QE angular distribution measurements. The angular distribution of the QE shows unequivocal proof of plasmonic effects on the QE of the cathode. Figure 4.7 shows the data on five longitudinal positions with the angular distribution near the maxima and minima of the QE.
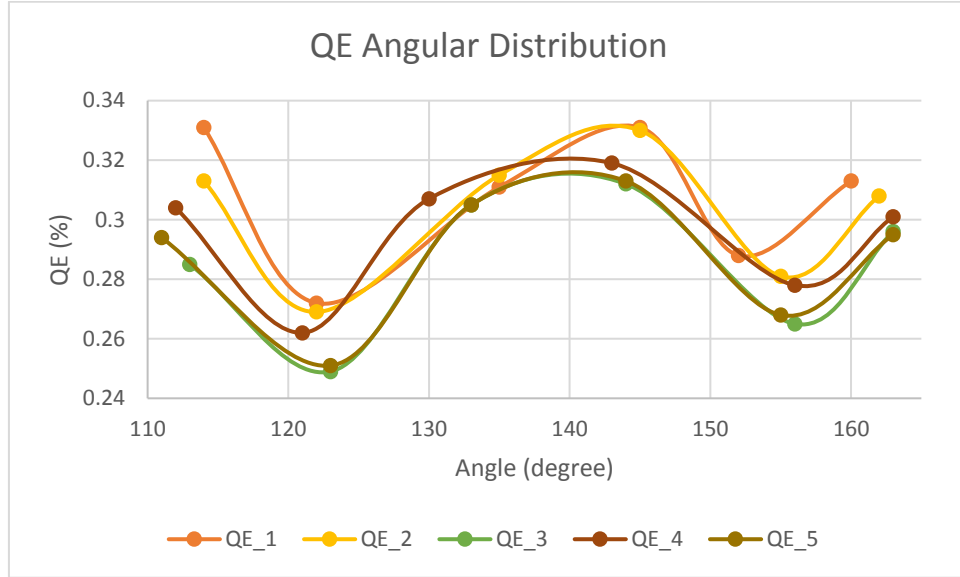
**Figure 4.7 QE angular distribution of a Cs/Ag/grating cathode after re-activation.**

| Extreme | Avg Angle ($^0$) | Incident Angle ($^0$) | Avg QE (%) |
|---------|------------------|------------------------|------------|
| *Max* | 162.2 | 23.5 | 0.303 |
| *Min* | 154.8 | 16.1 | 0.276 |
| *Max* | 144.2 | 5.5 | 0.321 |
| *Max* | 133.2 | -5.5 | 0.309 |
| *Min* | 122.2 | -16.5 | 0.261 |
| *Max* | 112.8 | -25.9 | 0.305 |
| *ZERO* | 138.7 | | |

**Table 4.4 Average angular dependence of QE for a ND 50 nm Ag/grating sample after reactivation.**

One can observe a somewhat symmetrical distribution of angular positions of the QE maxima and minima. This agrees with the reflectivity measurement of Figure 4.3(a). In the data, two plasmonic resonance positions are observed. One is at ~14.5° and the other is at ~25⁰, with a maximum of reflectivity in-between. If we assume the effect of Cs on the Ag grating cathode will not cancel the resonance effect on the cathode, we can expect the measurement of QE to display a maximum, minimum, and maximum sequence. This

should also apply when the light is shining from the other side of the incident plane and this cause the symmetrical distribution of the angular positions of QE extreme values.

 As shown in Figure 4.3, the first resonance has a smaller minimum than the second one. We observe a similar effect in the angular distribution of QE. The two maxima in the middle of 6 angular positions show larger QE values than the ones that are away from the center and indicates the plasmonic influence on the QE of grating cathode.

To calculate the incident angle, we start by calculating the average angle positions from 5 different sets of data. Once we find the average angle positions, we calculate the normal incident angle position by averaging the angle positions of the two adjacent maxima in the middle. For example, the average of 144.2° and 133.2° gives 138.7° to be the 0° of incident angle. This is because the middle two maxima's angle positions should have same incident angles as explained above. The 0° position was then used to calculate the incident angles by the difference from the angle position of each maximum/minimum, which is shown in Table 4.4. The sign of the incident angles are following the definition in Figure 4.8.
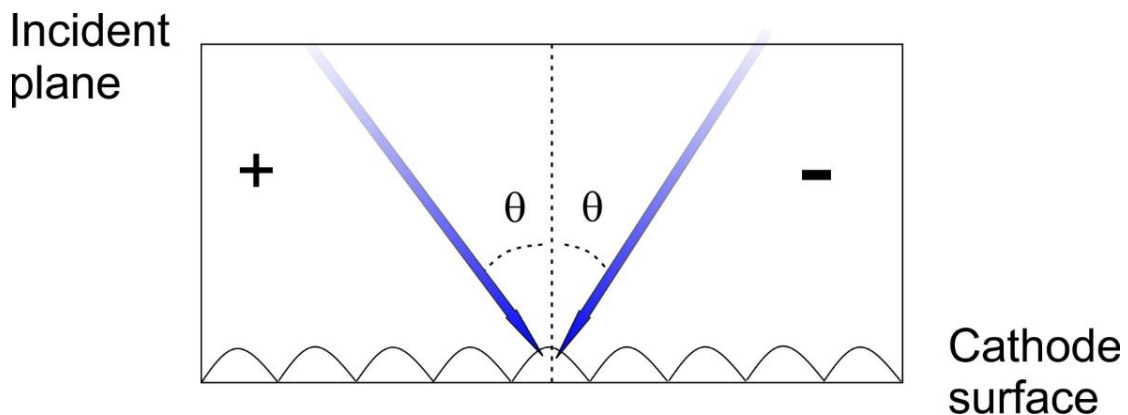


Figure 4.8 Illustration of the definition of incident angle in the incident plane.

From the result of incident angles (Table 4.4), one can clearly see that the calculated

incident angles from either direction are very close. For the minimum positions, the

difference of the incident angle is ~ 0.4°. For the maximum positions that are far from 0°,

the difference of the incident angle is ~1.5°.

The average QE for each incident angle is also shown in Table 4.4. One can see that the

absolute maximum and absolute minimum of QE after re-activation have decreased from

that of the initial activation. The absolute maximum of QE drops from 0.360% to 0.321%

and the absolute minimum of QE drops from 0.300% to 0.261%. It is suspected that the

cesium atoms that form cesium compounds on the cathode surface during baking is the

cause for this QE drop.

The life time is measured and calculated as

$$QE^f = QE^i \exp(-\frac{t}{\tau}) \quad , \quad (4.1)$$

Where $QE^i$ is the initial QE and $QE^f$ is the final QE in the measurement. $t$ is the

measured length of time and $\tau$ gives the life time. A lifetime of 50.6 hrs was calculated

after the re-activation process with light shining on the cathode surface.

4.5.4 Substrate Annealing

Substrate annealing was also carried during the sample preparation process to see the

effect of such treatment on the QE. Because of the possible existence of water molecules

on the surface of the substrate, we annealed the substrate at 250°C for one hour in the

deposition chamber and then cooled it down to room temperature before deposition of

50nm Ag. One example of a QE measurement at near-zero incident angle for a sample without substrate annealing and a sample with substrate annealing is shown in Table 4.5. We can see that the substrate annealing enhances the QE from ~0.26% to ~0.4% at first activation.

| Substreate Annealing (Y/N) | QE with Cs Deposition (%) | QE Re-Activation After Heat Cleaning (%) |
|---|---|---|
| N | 0.26 | 0.14~0.15 |
| Y | 0.4 | 0.22 |

Table 4.6 QE at zero incident angle with and without substrate annealing during deposition process.

4.5.5 An Attempt to Grow Cesium Oxides

We also looked for the best method to form cesium oxides/sub-oxides on the Ag grating cathode. One successful example was carried with the "yo-yo" process[53] described in Chapter 2 and is shown in Figure 4.7.
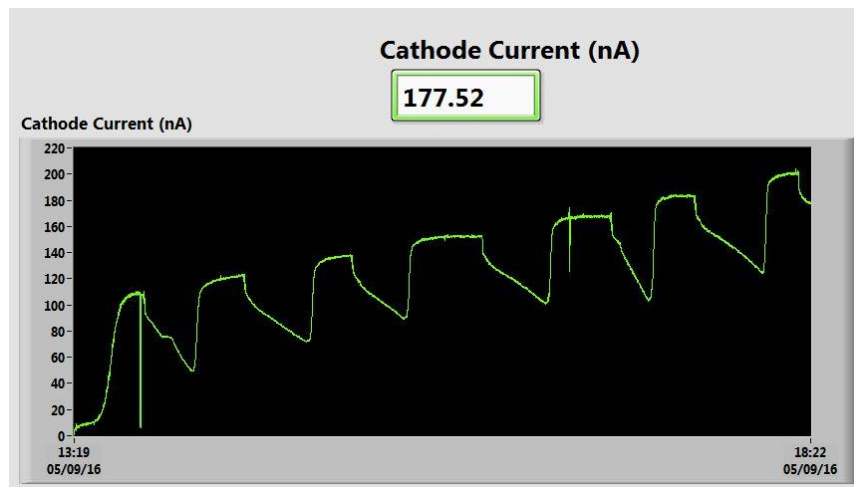


Figure 4.9 Example of "yo-yo" process of CsO on a Ag grating cathode with photocurrent v.s. time.

As is mentioned before, the photocurrent during the activation will reach a plateau as the Cs thickness grows. The dropping of the QE in one cycle as shown in Figure 4.8 is caused by the oxygen added into the system with partial pressure $\sim10^{-8}$ Torr. After the oxidation of Cs on cathode surface, further deposition of cesium causes an increase of the maximum plateau of QE. Repetitions of such process will give a much larger QE. In this example, the QE is increased from 0.15% to 0.28% after six cycles. However, this yo-yo process is very time-consuming . Each cycle requires approximately 40 minutes. For a yo-yo process of six cycles, the total activation will take nearly 5 hours.

# Chapter 5 Oblique Angle Deposition Silver Grating Cathodes

5.1 Oblique Angle Deposition (OAD)

We have discussed the QE performance of the grating cathode under normal deposition of magnetron sputtering. The thin film follows the grating structure of the substrate when it is deposited at normal deposition. Thus, the grating profile of the silver cathode is determined by the substrate grating profile. However, it is also beneficial to have a look at other deposition angles, such as an oblique angle deposition and its effect on the resulting grating profile. Such oblique angle deposition (OAD) method is also called the glancing angle deposition (GLAD)[82]. It has wide applications in producing nanostructures because of its ability to engineer a column micro-structure for porous thin film deposition. The OAD method was also proposed to engineer the grating thin film structure by Johnson[83], et al. They found that by the shadowing effect that is caused by the large incident angle, the atoms will accumulate on one side of the stripe and cause the other side of stripe to have less deposition. As the deposition continues, the shadowing effect will become more noticeable, and eventually will block the atoms from reaching full deposition coverage on the grating structure. If the angle is chosen to have little coverage on the grating groove and much coverage on the grating stripe, one can expect a deeper grating thin film than that of normal deposition.

An illustration of the angle set up in OAD is shown in Figure 5.1 (a). Figure 5.1(b) shows an example of the shadowing effect during deposition on a grating substrate.
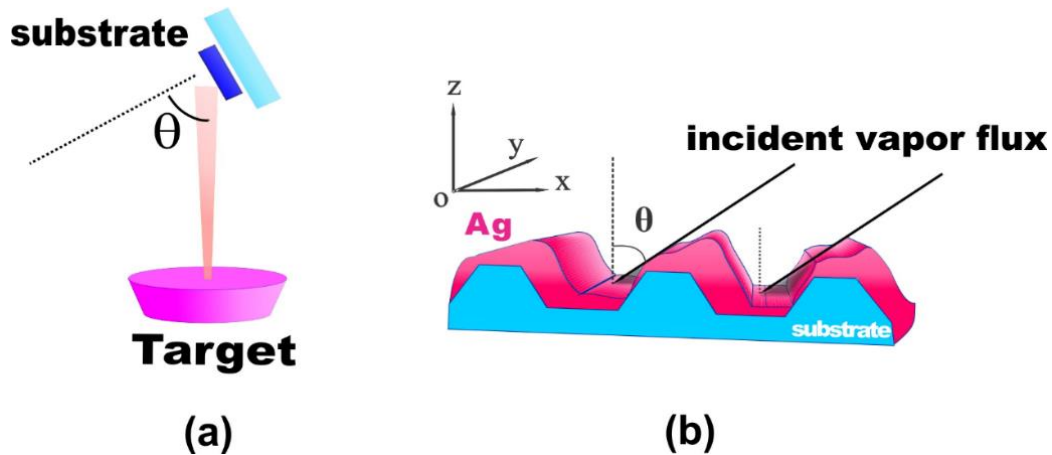
**Figure 5.1 (a) Illustration of oblique angle set up in the PVD system. (b) An example of shadowing effect caused by the large incident angle during PVD.**

The oblique deposition angle can be easily reached using a bracket as described below. We used an aluminum 6061 sheet as raw material. We cut the sheet into a 1 inch wide and ~ 2 inches long rectangle piece. The piece was divided into 2 parts in our design. One is the part that was fastened to the sample holder. This part was machined with a longitudinal slot in order to add flexibility when adjusting the sample position. The other part was used to support the substrate. The substrate was fastened through a screw with a piece of foil. The whole aluminum piece was mechanically bent to reach a desirable deposition angle, such as an incident angle of ~$77^0$ for the initial experiments of OAD on polycarbonate substrates. The bending angle of the aluminum piece was later modified when it was used in the Ag deposition on another type of grating substrate. The illustration of the OAD setup is shown in Figure 5.2.

**Figure 5.2 Illustration of the OAD setup, including the top view (top), the substrate position (bottom left) and the slot (bottom right).**

5.2 ND and OAD Ag50nm/grating

To test the effect of OAD on the plasmonic resonance, we prepared two samples under both ND and OAD geometries. Note that these samples were deposited on polycarbonate grating substrates, which has a standard grating periodicity of 740nm.  An AFM measurement of the grating substrate is shown in Figure 5.3(a) and the line scan is in Figure 5.3(b). From the line-scan, we can observe a grating groove depth of 66nm and a FWHM of ~611nm. This measurement of the grating profile was used in the later simulations of the grating substrate.
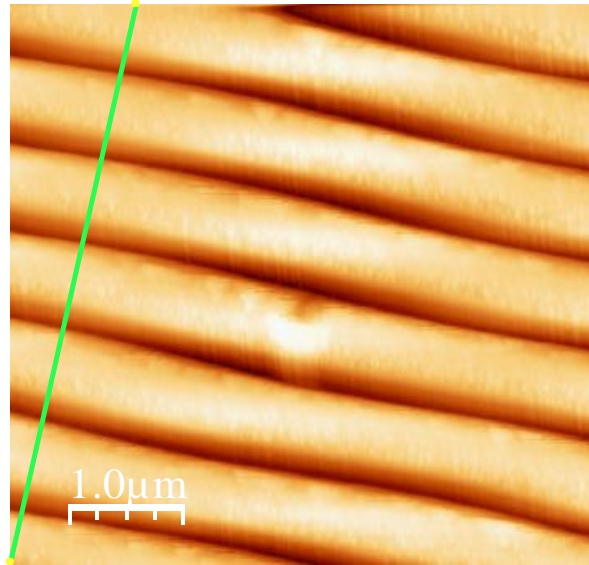
Figure 5.3 (a) Topography image from AFM measurement on the polycarbonate grating.
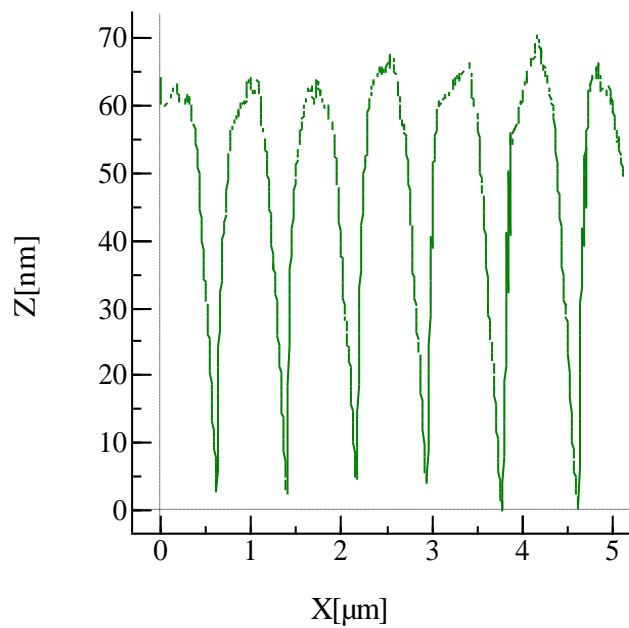


Figure 5.3(b) Linescan drawn from topography measurement showing the grating groove depth and FWHM of grating substrate.

We deposited a sample of 59nm ND and 50nm OAD separately under the same Argon pressure of 7.5 x $10^{-3}$ Torr with a 2.0 x $10^{-6}$ base pressure.

76

## 5.3 Topography Measurements

The topography and linescan for both samples are shown in Figure 5.4 (a), (b) and (c), (d).
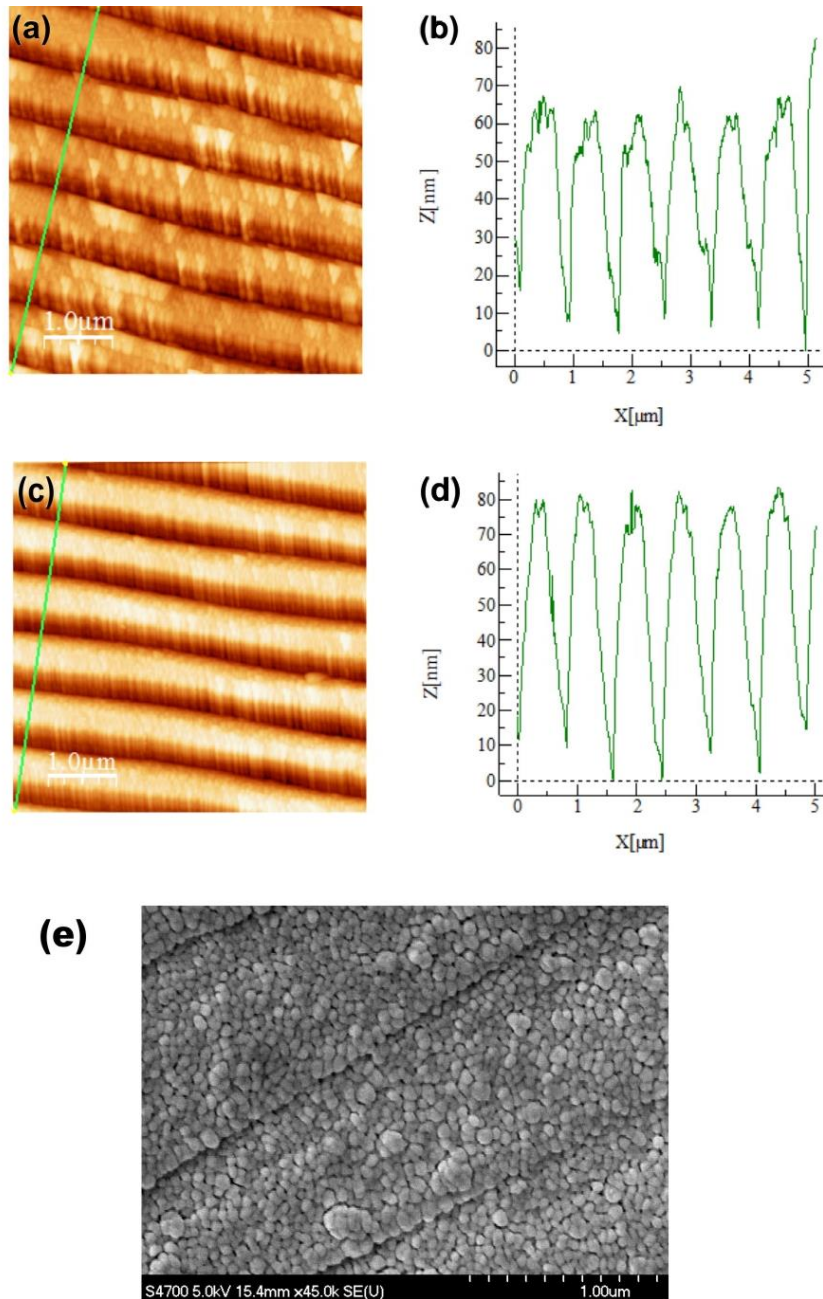


**Figure 5.4 (a) Topography of ND sample. (b) Linescan drawn from topography of ND (c) topography of OAD sample. (b) Linescan drawn from topography of OAD. (e) SEM image of OAD sample showing full coverage on grating substrate.**

The AFM images show a clear difference in grating amplitude for these two different types of samples. For the OAD sample, the grating amplitude of the deposited Ag thin film (~80 nm) is 15 nm higher than that of the sample grown under normal incidence geometry (~65 nm). This difference is due to shadowing effects from the underlying pattern stemming from the large incident angle ( $\theta \approx 77°$ ) of the Ag influx onto the grating substrate during deposition. Note here that because of the steepness of the trajectory of the AFM tip during scans over the grating surface, the actual groove depth values for both samples could have been experimentally under-estimated.

5.4 Reflectivity Measurement

The p-polarized reflectivity versus incident light angle was experimentally investigated on both types of samples. The samples were illuminated with 405 nm p-polarized light, with the plane of incidence perpendicular to the direction of the grooves in the patterned surface. The incidence angle was varied between 20º and 38º to obtain reflectivity vs incident-angle data. The experimental reflectivity results for typical OAD and ND samples are shown in Figure 2(a). We observe a significant difference in the shape of the reflectivity curve at the SPR angle between these two samples. A narrower and sharper resonance is noticed for the sample grown using OAD compared to the ND one. We point out that the experimental results for both samples were normalized with the same parameters such as the maximum and minimum reflectivity achieved with the OAD sample.  We followed the same normalization method in all the simulations. This normalization was carried out to aid the comparison between samples and between experimental results and simulations.
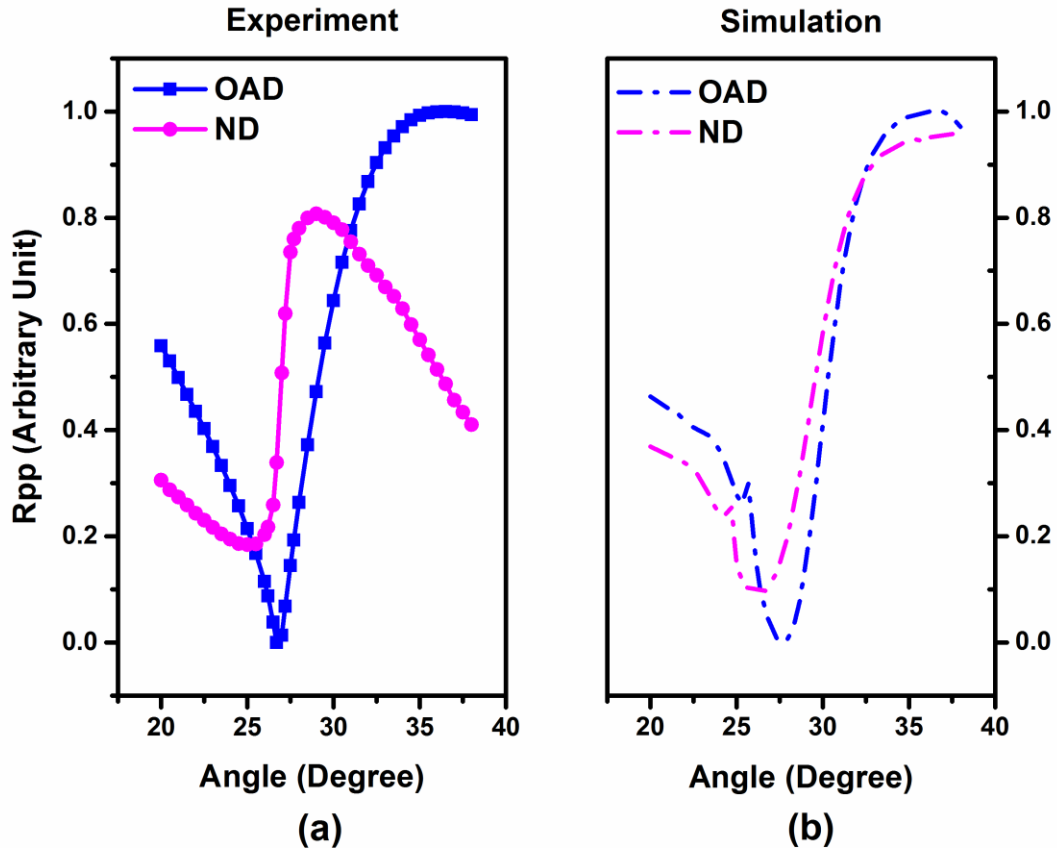
**Figure 5.5 (a) Reflectivity measurement for ND (magneta) and OAD (blue) samples showing plasmonic resonance angle positions.**

5. 5 Simulation Results

We carried out simulations of both grating structures using the amplitude and pitch experimentally obtained under both thin film deposition geometries using the EM Explorer software[81]. Using the dimensions obtained from the AFM line scan profile measurements across the surface topography of uncoated gratings, we simulated an isosceles trapezoidal profile using the same nominal dimensions for the substrate grating profile in both types of samples. The dimensions of the Ag film layer for each of the two simulated structures were set according to the AFM measurements for the OAD and ND samples. An illustration of the grating profile used in both cases is shown in Figure 5.6.
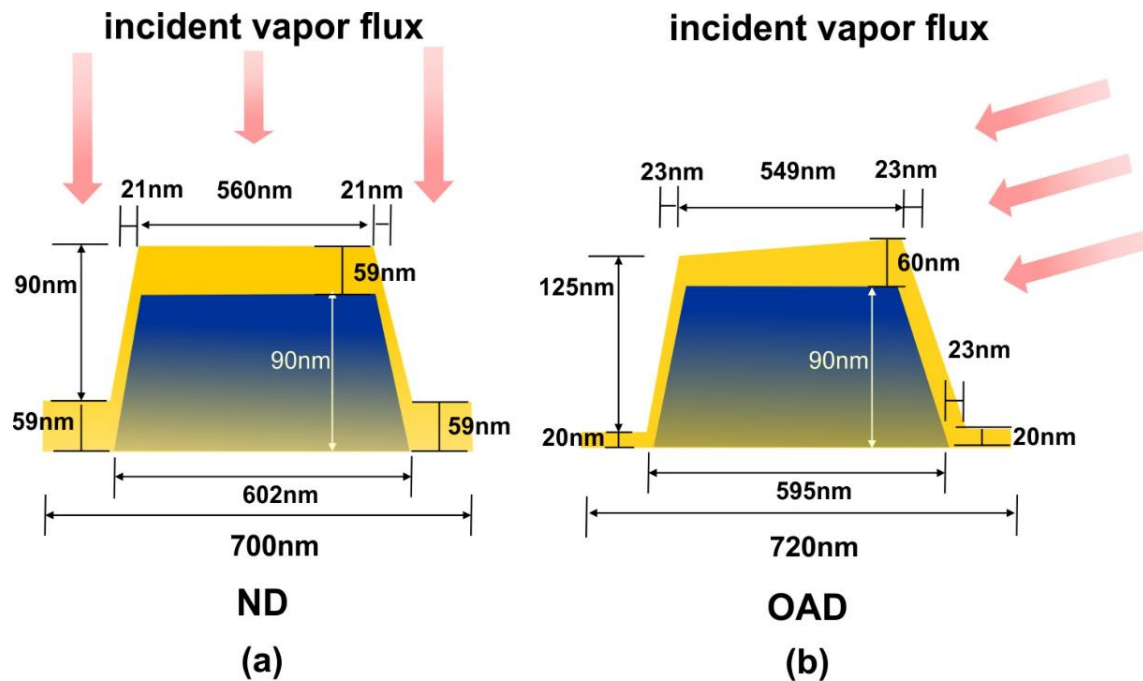
**Figure 5.6 (a) Simulation model for 59nmAg/Grating ND sample. (b) Simulation model for 50nmAg/Grating OAD sample.**

The reflectivity curves achieved with such simulations for both types of samples are shown in Figure 5.5(b) and compared to the experimental results in Figure 5.5(a). For the simulations, the Ag thin film follows the trapezoidal structure of the grating substrate homogeneously in the ND sample, while the Ag thin film in the OAD sample was distributed asymmetrically on either side of the stripe to accommodate for the shadowing effects of the oblique deposition. The average thickness of the Ag thin films was set at ~60 nm for the simulated structures, agreeing with the measured profiles in the real samples. The geometrical distribution of the Ag film used to simulate the ND and OAD samples are indicated in Figure 5.6(a) and Figure 5.6(b), respectively.  Note that the grating period used to better fit the ND sample results has been set at 700 nm while for the OAD, the grating pitch is set at 720 nm, an acceptable difference that is within the 5% variability of our commercial grating substrates (standard periodicity 740nm). The simulated Ag thin film structures therefore accurately represent the two types of samples and account for the different deposition geometries investigated. The refractive index used for the simulation of

the ND sample was n = 0.17, k = 2.10, while for the OAD sample n = 0.17, k = 2.20, was used.  We kept the optical constants very close to each other in the simulations.  In this way, we are able to examine the effect of a changing grating profile on the resonance, which is expected to have a more important role since we kept the Ag thickness very similar on both samples. We note though, that the measured Ag thickness is slightly different between the two samples.  This can be attributed to a different growth mode, e.g. different incident angles affecting growth rates, but we do not expect this to be a substantial effect on the measurements. The value of the index of refraction used for the substrate was n = 1.56 for the simulations of both samples. Detailed information for both grating models can be observed in Figure 5.6. Note that the very slight difference in the grating substrate dimensions for the OAD and ND models (e.g. 7nm difference in the bottom width) is due to the slightly different resolution used in the simulations but this doesn't affect the results. All the values of dielectric constants are within reasonable margins (<5%) from those obtained from reference[82].

We also want to point out that the simulation model used for the OAD sample is justified because the actual profile of the grating substrate should allow full coverage of the Ag thin film coating even if not uniform. This is expected because reflections of incident atoms from the adjacent grating groove can also occur, allowing coating of the shadowed side of the groove considered. This full coverage of the groove is shown in Figure 5.6 (b) and Figure 5.4 (e).

To understand the physical mechanisms governing our experimental optical observations regarding the difference between OAD and ND samples, we consider the process of a Fano resonance in a grating coupler. In the Fano resonance, a bright mode which is a radiative mode excited by the far-field illumination interferes with a dark mode or a

localized mode. The total response is often found to be asymmetric around the resonance as it is shown in both the OAD and ND reflectivity curves (Figure 5.5(a)). The main limitation of the original Fano resonance expression is that it lacks accounting of intrinsic losses due to dark modes. Here we adopt Gallinet and Martin's description of the Fano resonance[22-24], including consideration of intrinsic damping as shown in Eq. (5.1). This treatment enables understanding the influence of electromagnetic interactions on the resonance through the information drawn from a Fano profile.

The line profile for the localized mode is described in Eq. (5.1).

$$r_a(\omega) = \frac{(\frac{\omega^2 - \omega_a^2}{2W_a\omega_a} + q)^2 + b}{(\frac{\omega^2 - \omega_a^2}{2W_a\omega_a})^2 + 1}, \qquad (5.1)$$

where $\omega$ is the angular frequency of the incident light, $\omega_a$ is the resonance central spectral frequency, $W_a$ is the approximation of spectral width where $W_a << \omega_a$ , $b$ represents the damping of the Fano resonance and affects the contrast of the resonance profile and $q$ characterizes the asymmetry of the resonance profile.

The radiative mode can be constructed by a pseudo Lorentzian form as in Eq. (5.2)

$$r_s(\omega) = \frac{a^2}{(\frac{\omega^2 - \omega_s^2}{2W_s\omega_s})^2 + 1}, \qquad (5.2)$$

where $a$ is the maximum amplitude, $\omega_s$ is the resonance frequency, and $W_s$ is the approximation spectral width if $W_s << \omega_s$. The total response of the system is Eq. (5.3),

given by the product of Eq. (5.1) and Eq. (5.2), and can be applied in measurable

quantities for fitting parameters.

$$R(\omega) = r_a r_s \quad (5.3)$$

When light shines on a grating coupler, its horizontal component of momentum can be

expressed as

$$k_{//} = \frac{\omega}{c} \sin \theta + N \frac{2\pi}{\lambda_G} \quad (5.4)$$

where $\theta$ is the incident angle, $\lambda_G$ is the grating periodicity, $N$ is the diffraction order,

and $c$ is the speed of light. We measured the 0th order reflectivity, and the SPR appears

when the 1st diffraction order vanishes. Thus we set $N$ as 1 and the grating periodicity as

the standard value $\lambda_G = 740\text{nm}$. The reflectivity response of the incident angle in Fig.

5.4(a) is caused by the dependence of $k_{//}$ on the incident angle. Thus, we first calculate

the value of $k_{//}$ for each $\theta$ of 405 nm light by Eq. 5.4. The reflectivity can now be

expressed as a function of $k_{//}$. To better analyze the physics mechanism of this Fano

resonance, we propose a pseudo frequency $\omega_{psd}$ and a pseudo incident angle $\theta_{psd}$, and

use $\omega_{psd}$ to represent the effect of incident angle on the $k_{//}$ after setting a $\theta_{psd}$. We

calculate (in Eq. 5.4) the value of a pseudo frequency $\omega_{psd}$ under each $k_{//}$. In this way, we

convert the reflectivity data to a function of $\omega_{psd}$. One can plot the reflectivity versus

pseudo-angular frequency $\omega_{psd}$ as in Figure 5.7(solid lines). The new reflectivity curves are

then fitted by Eq. 5.3 using OriginLab[83]. We show the fitting parameters along with the

standard errors in Table 5.1 and the fitting curves dashed in Figure 5.7 (red). Note that we

set incident angles for both samples at their respective resonance angles. We find that

varying the pseudo incident angle from 20 to 38 degrees has very little effect on the result

of $b$ and $q$ for both types of samples, evidencing a characteristic relationship between

these two parameters and the Fano profile itself within the considered angle range. The

dark mode and bright mode for each sample are plotted as in Figure 5.7 as an example.

Note that the term including grating periodicity is cancelled during the calculations for each

sample and the only changing part in equation (5.4) is the term with $\omega_{psd}$, thus it doesn't

affect the fitting results.
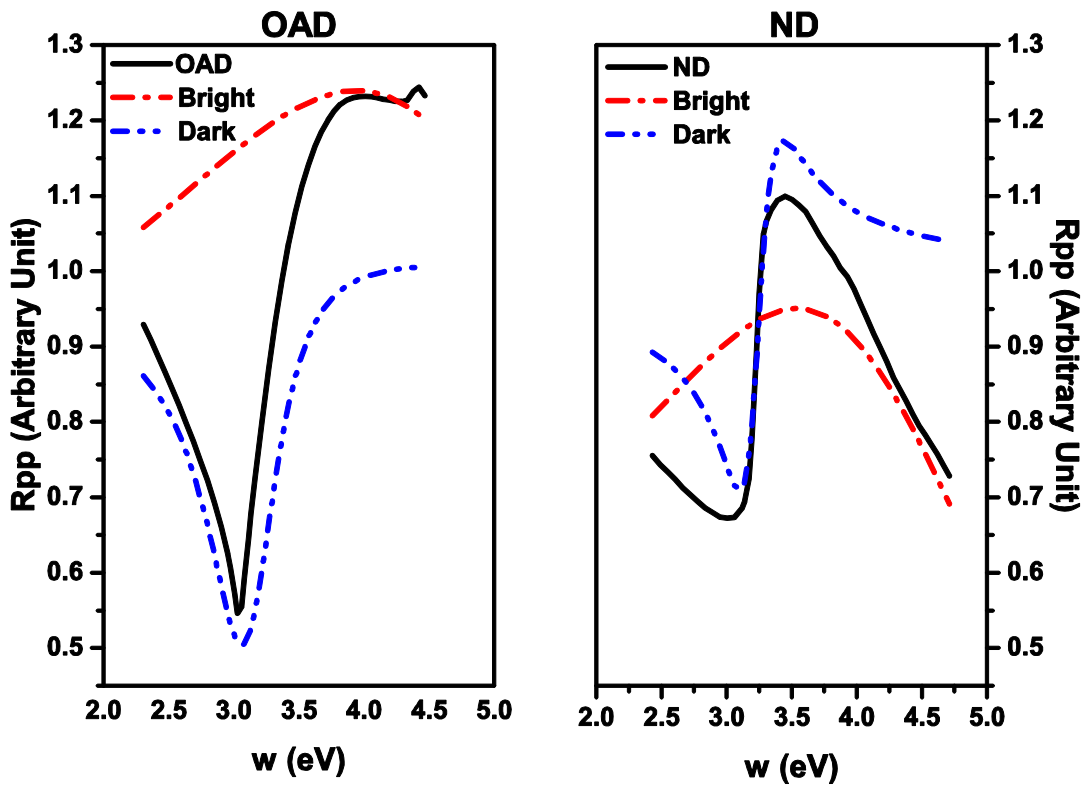


**Figure 5.7 Fitted reflectivity of radiative (bright) modes and localized (dark) modes for OAD (left) and ND (right) samples. Black is experimental data, red is the radiative (bright) mode, and blue is the localized (dark) mode.**

| | OAD | | ND | |
|---|---|---|---|---|
| | **Fitted Value** | **Standard Error** | **Fitted Value** | **Standard Error** |
| $w_a$ | 3.10575 | 0.01979 | 3.22967 | 0.00828 |
| $w_s$ | 3.94352 | 0.10329 | 3.53975 | 0.03437 |
| $W_a$ | 0.32953 | 0.01436 | 0.16508 | 0.00885 |
| $W_s$ | 3.12978 | 0.52405 | 2.22655 | 0.11962 |
| $q$ | 0.06475 | 0.02458 | 0.22555 | 0.0093 |
| $b$ | 0.5083 | 0.00914 | 0.83131 | 0.02203 |
| $a$ | 1.11337 | 0.00989 | 0.97496 | 0.00477 |

**Table 5.1. Fitting Parameters of Fano Resonance Profile of Eq. (5.3), both incident angles of OAD and ND sample at its SPR angle, respectively. Standard errors are defined as in OriginLab Non-linear Fitting.**

We see that, in our fitting results, the asymmetry parameter $q$ for the OAD samples is much smaller than for the ND samples and its reflectivity shows a near symmetric resonance profile. On the other hand, the value of the modulation damping parameter $b$ for the OAD samples is noticeably lower than that of the ND samples with good accuracy. The imaginary part of the dielectric permittivity in a metal would be accountable for the damping effect when there is interference between bright and dark modes, and it is considered an intrinsic loss. This damped interference displays either incomplete construction or destruction effects on the Fano profile, and the $b$ parameter evaluates such effect by comparing the ratio between the intensity lost to the metallic structure and the intensity transferred from the radiative mode to a localized mode. When $b$ equals 0, the intrinsic losses would fully disappear and the reflectivity should reach 0 at the resonance angle. A lower value of the $b$ parameter indicates a lower ratio of intrinsic losses coupling radiative and localized modes. In our case, with the consideration of similar dielectric

permittivity, a stronger coupling between radiative modes and localized modes in the OAD samples should be the cause of the lower damping compared to the ND samples. Thus, we can conclude that the main enhancement effect in the resonance is due to lower damping in the samples grown by OAD than that of the ND ones. Such a scenario suggests the existence of an associated enhanced electromagnetic field in the OAD samples, which could benefit many applications, such as photoemission from metallic photocathodes, etc. We believe that the bright mode in the Fano resonance corresponds to the 1st order diffraction in the grating as discussed in Reference 18. After diffraction of incident light, the 1st order diffraction is generated and couples to the surface plasmon resonance, which is a localized mode in the Ag grating. The first order diffraction generated also diffracts and contributes to the homogenous zeroth order. As a result, the zero order diffraction is the superposition of the two interactions mentioned above.

To examine this effect in both the OAD and ND samples, we also simulated the electromagnetic field profile based on the previous model described. These simulations were carried out under the same illumination conditions as in our experiments, i.e., at the same wavelength, fluence, and critical angle as experimentally determined. The magnitude of the electric fields computed by these simulations are shown in Figure 5.8. The expected stronger EM fields near the surface of the deeper-grooved (OAD) sample compared to the shallower grooved sample (ND) is confirmed, and it is attributed to a lower damping of the Fano resonance, which indicates a stronger coupling of the first diffraction order with the SPR excited on the grating structure[9]. Thus, we can conclude that the OAD method offers a viable approach to tailor local electromagnetic field enhancements near the surface in grating-induced Fano resonances, due to our ability to control the damping processes.
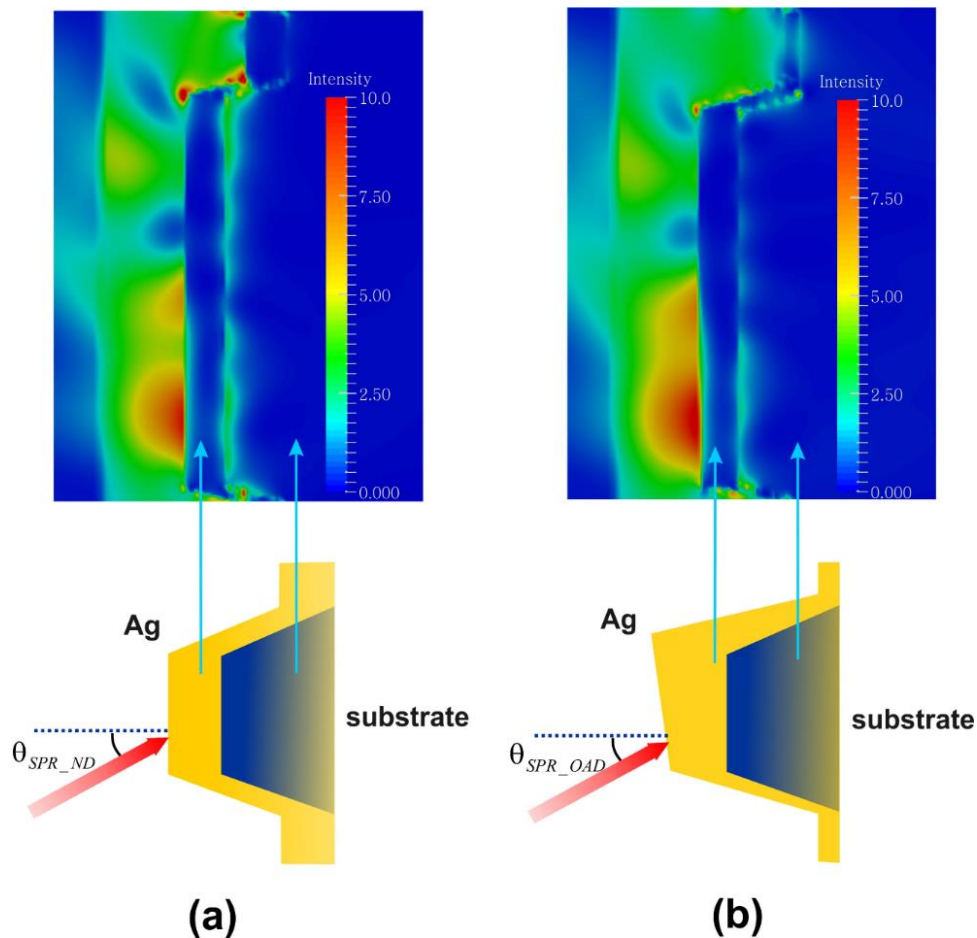
**Figure 5.8 (a) Simulation of EM field on ND cathode at its plasmonic resonance angle. (b) Simulation of EM field on OAD cathode at its plasmonic resonance angle.**

## 5.6 Quantum Efficiency

### 5.6.1 Introduction

Based on the theoretical prediction of a larger electric field on the OAD sample, we carried

out the measurement of the QE on the OAD Ag50nm/grating cathodes. The first QE

measurement of OAD sample was on a 50 nm Ag thin film on the polycarbonate grating

substrate as is described in section 5.2. However, a detrimental difficulty for measurement

of QE on such a cathode is that the polycarbonate substrate has quite a low melting point at ~ 150C. The alteration of grating structure will happen earlier before the temperature reaches 150C, and would cause deformation of the cathode. However, the baking of the vacuum loadlock is necessary to reach a good UHV. This makes the polycarbonate grating substrate an unsuitable option. An optical diffraction grating was then brought into the project for such reason.

The standard information of the grating substrate can be found at Table 4.2. Such grating was also used in ND grating cathodes of Chapter 4.

## 5.6.2 Sample Preparation

The OAD sample was prepared in the Veeco system at a base pressure of $1.2 \times 10^{-5}$ Torr. Grating substrates were ultrasonically cleaned firstly in an acetone bath and then a methanol bath. Silver was deposited on the substrate in an Ar pressure $7.5 \times 10^{-3}$ Torr by DC magnetron sputtering deposition. The oblique incident angle was at ~60$^\circ$.  After deposition, the OAD 50nm cathode was also taken to atmosphere to be transferred to the QE measurement system.

## 5.6.3 Activation with Cs

To compare the QE of the OAD cathode with the ND cathode, we kept the parameters for activation consistent for both OAD and ND cathodes. These parameters include the cesium evaporation working current, cesium evaporation length of time and laser power for activation. In particular, cesium was evaporated at a working current of 4.7A. The 405 nm laser power for activation at OAD sample was ~12.2 uW. A deposition of 1 hr and 20 mins Cs on the cathode brings the QE to the maximum value. This ensures the same deposition

thickness of cesium on the OAD cathode compared to that of ND cathode.  A measurement of QE was carried out after all the hydrogen outgassing due to the heat of Cs dispenser were pumped away.

5.6.4 Quantum Efficiency Results

Figure 5.9 shows the angular dependence of the QE for the OAD sample. It is interesting to notice that the angle positions of maximum and minimum QE also follow a similar trend as for the ND sample. The five measurable angle positions for QE extreme values follow a sequence from top to bottom as maximum, minimum, maximum, maximum, minimum. The angle position at lower than 285 degree is, however, not measurable, due to the same reason shown in Figure 4.5. i.e. because the cathode surface is above the rotational center, the incident spot will scan across the surface as the cathode rotates in the transverse direction and will reach the edge of the cathode.
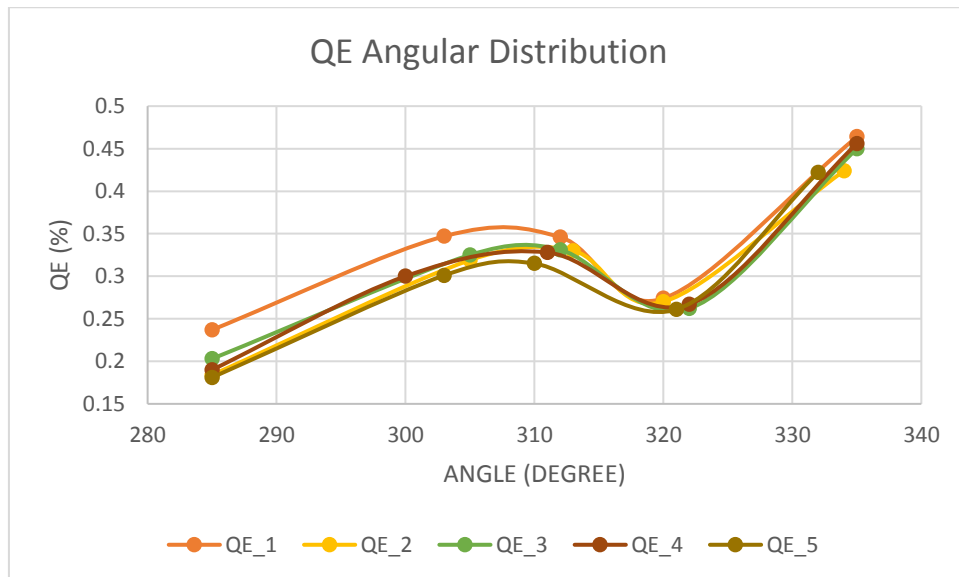


Figure 5.9. Angular Dependence of QE for OAD 50nmAg/Grating sample.

| Extreme | Avg Angle ($^0$) | Calculated Incident Angle ($^0$) | Avg QE (%) |
|---------|------------------|----------------------------------|------------|
| *Max* | 334.2 | 26.9 | 0.443 |
| *Min* | 321.0 | 13.7 | 0.267 |
| *Max* | 311.6 | 4.3 | 0.330 |
| *Max* | 303 | -4.3 | 0.318 |
| *Min* | 285 | -22.3 | 0.199 |
| *ZERO* | 307.3 | | |

Table 5.2  Average angular dependence of QE for OAD 50nmAg/Grating sample.

To get a closer view of the angular dependence of QE, we followed a similar analysis method as in chapter 4. We took the calculations of average angle position for each extreme QE. The 0º incident angle position was decided as the middle position between adjacent maximums (i.e. 311.6$^0$ and 303.0$^0$). The incident angles were calculated by the difference from the 0º incident angle, which are shown in Table 5.2. The positive and negative sign of the angle represents the two half-spaces in the incident plane, as shown in Figure 4.7.

As shown in chapter 4, the incident angle distribution of QE for ND cathode follows a symmetrical distribution. However, this is not true for the OAD cathode. An anisotropy appears in the angular distribution of QE for OAD cathode, which is shown in Table 5.3(b). The incident angles for two minimum positions have a ~8.6º difference, which is apparently not because of the 2º resolution of the angular measurement on the apparatus.

 One can think that this results from the effect of a large incident deposition angle. In the real sputtering deposition, the deposition rate relies on the distance between the substrate and the target. The deposition rate at a close distance is larger than the one that is far from the target. At the normal deposition, the difference of the distance for the two edges of the substrate is negligible. This gives an even coverage of the silver thin film on the grating substrate. However, when the deposition angle is oblique, the substrate has one edge that is measurably closer than the other. For our grating substrate, a ~12.7 mm

distance is expected. This leads to a slowly decreasing deposition rate along the substrate surface. For the side that is close to the target, a larger deposition rate should be expected and vice versa. Because we placed the substrate in such a manner that the grating stripes are in the perpendicular direction to the deposition flux, a small gradient in the thickness should show in the same direction. In the QE measurement, the cathode is also placed in the direction where the transverse scan direction is perpendicular to the grating stripes. Thus, the rotation in the transverse direction moves the laser on the cathode surface along the direction that is perpendicular to the stripe. The plasmonic QE performance is suffering from this small gradient of thickness, which could result in the shifting of resonance positions.

It is also noticeable that the average absolute maximum of the QE of the OAD sample is 0.443% at $26.9^0$ of incident angle. The single maximum of QE of OAD sample is 0.464%. The lifetime of the cathode at this attempt is 43hrs. The ND sample has an average maximum QE of 0.36% and single maximum of 0.367% (Table 4.3). Thus, the enhancement of QE for OAD is noticeable ~23.1% for the average and a maximum of ~26.4% for the single measurement.

5.6.5 The Effect of Heat Cleaning

We also observed the effect of heat-cleaning on the angular dependency of QE of OAD cathode. After cleaning the Cs at ~266 C for 30 mins, the photocurrent from the remnant Cs on the cathode was ~0.1 nA. The re-activation of the cathode was carried after the cathode cooled down to room temperature (RT). A current of 4.7A for the Cs filament was used and the deposition lasted the same amount of time as for the previous activation (~1hr 20mins). The laser power for the activation of cathode was also the same (~11.2 μW).
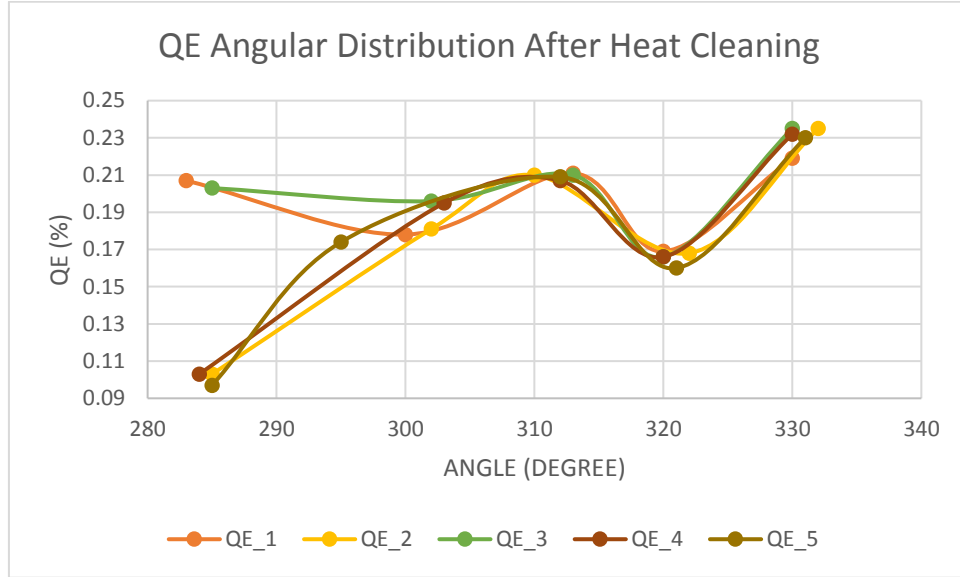
**Figure 5.10 Angular Dependence of QE for OAD 50nmAg/Grating sample after re-activation.**

| Extreme | Avg Angle ($^0$) | Incident Angle ($^0$) | Avg QE (%) |
|---|---|---|---|
| *Max* | 330.6 | 24.4 | 0.2302 |
| *Min* | 320.6 | 14.4 | 0.1658 |
| *Max* | 312 | 5.8 | 0.2094 |
| *Max* | 300.4 | -5.8 | 0.1848 |
| *Min* | 284.4 | -21.8 | 0.1026 |
| *ZERO* | 306.2 | | |

**Table 5.3 Average angular dependence of QE for OAD 50nmAg/Grating sample after re-activation.**

The QE results of OAD cathode after re-activation are shown in Figure 5.10. The calculation results for incident angle positions as well as the respective average QE values are shown in Table 5.3. We can notice that the incident angles calculated in Table 5.3 for OAD cathode after re-activation are close to the ones in Table 5.2, and have an average difference of $1.08^0$ from the initial activation results. The plasmonic effect on the QE also

has a similar trend and gives a similar difference of QE at the absolute maximum angle when it is compared to the absolute minimum of QE.

However, one can observe that the QE values after re-activation were noticeably reduced (Figure 5.11). The average absolute maximum of QE after re-activation is 0.2302% at 24.4$^0$ (Table 5.4), in comparison with 0.4432% after initial activation of cesium. The QE drop for OAD cathode at its average maximum value is ~48%. For ND sample, the drop is ~11%. We can observe that OAD cathode shows a larger QE drop from the baking of the sample. The life time after re-activation is 25 hrs, which is also much shorter than the one after initial activation.
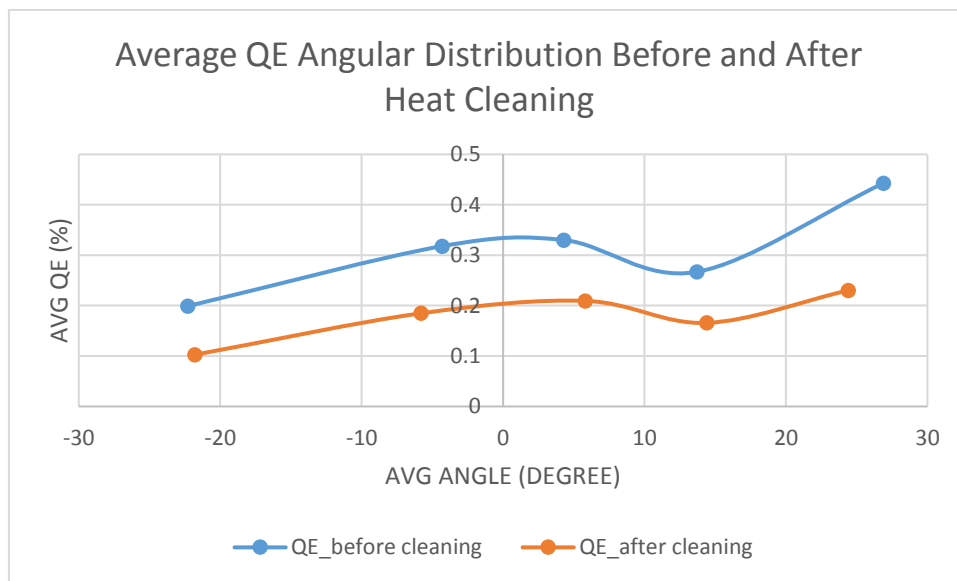


Figure 5.11 Average QE v.s. average incident angles : before (blue) and after heat cleaning (orange).

In spite of the possible cause of the QE drop that was discussed in Chapter 4, the reason why the OAD cathode suffers a larger effect from the heating is unclear. One possible process is that the silver thin film was annealed during the heat cleaning. One may argue that the annealing has modified the grating structure of the silver thin film and smoothened the OAD enhanced grating structure, which then causes a drop of QE. However, it was

also observed that the enhancement between the absolute maximum and minimum in Table 5.10 is similar with that of Table 5.9. This indicates that the plasmonic enhancement is not much affected, which argues against the existence of significant distortion of OAD grating profile. Further experiments are required for a better understanding of such phenomenon.

In particular, the QE performance can be improved by annealing of the substrate. As is discussed in chapter 4, annealing the substrate to 250 C for 1 hr shows a significant improvement on the QE of the ND cathode, which would improve the QE of OAD to a higher level. A better deposition of cesium oxide, or cesium fluoride is also of interest in improvement of the QE. Such cesium compound has the effect of doubling the QE of that of cesium and lengthen the life time of the cathode (Figure 4.8), which are of significant interest for application purposes.

# Chapter 6 Conclusions

We have discussed plasmonic silver grating cathodes, especially the influence of the plasmonic resonance on the QE of grating cathodes. This chapter will summarize the studies that were previously discussed. It will also start a brief discussion of a silver-based magnetic material that is called "silmanal", in the hope of enabling future plasmonic silmanal cathodes for production of polarized electrons, which is important for future large accelerator facilities.

6.1 MgO/Ag/grating Photocathodes

We have discussed the theoretical calculation and experimental measurement on the work function of MgO/Ag(100) systems. Calculations that are based on DFT have shown a decrease in work function ~1 eV from that of bulk Ag. Experimental results from Jaouen gives the work function of 5ML MgO/Ag(100) to be 3.017eV. The mechanism for such a lowering effect is explained by the change of charge dipole at the interface, which is caused by the reduction of the silver electron density at the interface, which was shown in Figure 3.2b.

The thickness of MgO is found to be less important for the lowering the work function, as shown in both theoretical and experimental results. For a thickness of 5 ML or higher (>2 nm thickness of MgO), the work function is barely changed, as shown in Figure 3.3. However, such a statement is not true for the plasmonic performance. Measurement on the reflectivity of MgO/50nmAg/grating shows a big resonance damping when thickness of MgO changes from the 2 nm to the 5 nm. A 2 nm (5 ML) thickness of MgO was chosen in the design of the plasmonic cathode for this reason.

However, this lowering effect of MgO on polycrystalline silver was not observed in our experiment. In the hope of a similar effect of MgO on polycrystalline silver thin films, we prepared and measured the QE of a MgO2nm/Ag50nm grating cathode. We were not able to demonstrate proof of photoemission in our measured results, which may be limited either by the laser photon energy (3.05eV) or the signal-to-noise ratio of our system. An upgrade of the photon energy would be preferred for better experimental results on such system, such as the recent measurement done by Droubay[77].  Their measurements of the QE in a planar MgO/Ag(100) system at 4.66eV laser excitation shows to be 7 times greater than of clean Ag(100). Further plasmonic effects on the QE of MgO/polycrystalline Ag system would be interesting to examine.

6.2 ND Cs/Ag50nm/Grating

Adding cesium to lower the work function was described in both chapter 4 and chapter 5. Characterization of the topography of ND 50nmAg/grating sample shows a complete coverage of silver thin film on the substrate. Optical measurement of reflectivity shows two reflectivity minima that are related to the plasmonic resonance on such a system. Later measurement of the angular distribution of QE on the ND cathode shows an agreement of the maximum/minimum angle positions with the reflectivity measurements. Interestingly, a symmetrical behavior of the incident angles is also shown in the QE measurements, which indicates the existence of plasmonic effects on the QE measurement. For the ND cathode, an average maximum QE of ~ 0.360% is observed. Heat-cleaning of the cesium causes a decrease of the QE in the ND cathode. After the re-activation, the QE maximum was ~ 0.321% and gave a life time of 50.6 hrs.

## 6.3 OAD Cs/Ag50nm/Grating

OAD was also discussed and introduced in the sample preparation for additional benefit of the enhanced plasmonic effect. Such a cathode was shown to have a stronger plasmonic performance in the measurement of reflectivity. Simulation based on EM Explorer also shows a prediction of strong electric field at the surface of the silver cathode, which may indicate an enhancement of the QE of a OAD cathode compared to the ND ones. Further measurements of QE show an average of 0.443% at the initial activation and a life time of ~48hrs. The angular distribution of the maximum/minimum of QE follows the same trend as that of ND, except that the calculated incident angles don't follow the symmetrical behavior of ND. This was explained by the existence of a small thickness gradient of Ag along the direction that is perpendicular to the grating stripe, which is caused by the deposition at oblique angle. The measurement of QE after re-activation shows a greater drop than that of ND. The specific reason for such effect is unknown. However, the difference of the absolute maximum and minimum of QE follows a similar value, which indicates the existence of a similar grating structure after heat cleaning.

Improvements in the QE of OAD cathodes are also possible. As discussed in chapter 4, the annealing of the substrate at 250 C gives a significant increase of QE of the ND cathode, which may be applied to the OAD cathode.  Careful deposition of cesium oxdies/fluorides is also of interest, after considerations regarding their ability of doubling the QE (Figure 4.8) and providing a longer lifetime.

## 6.4 Silmanal

Silmanal is one of the Heusler alloys that are usually made from Mn and other added materials such as Cu, Al, Ag, etc[87]. For silmanal, Mn, Al and Ag follow a recipe of ~86.75%

Ag, 8.80% Mn and 4.45% Al to provide the correct composition. The Heusler alloys are a type of material that belongs to the half metallic magnets (HFM). It has drawn much attention because of its unique electronic structure, where the material is metal in one spin direction and semiconductor in the other. This implies a hypothetically 100% spin polarization of electrons in when one assumes a 0 K temperature and neglects the spin-orbital interactions[88].  Experimental measurements of Heusler alloys give spin polarizations of 50% ~ 81%[89-91].

 The current state-of-the-art superlattice semiconductor photocathodes have a typical QE near 1% at the maximized polarization ~85%. For the silver grating cathode, with the consideration of the QE of OAD silver grating cathode at ~ 0.443%, and the potential of improving the QE by substrate annealing as well as by cesium oxide/ cesium fluoride, a plasmonic silmanal photocathodes have a potential to reach a QE higher than 1%, which would be beneficial for application in future accelerator facilities.

It is worth noting that recent measurement of distributed Bragg reflector (DBR) structures of GaAs/GaAsP photocathodes from Liu[92] gives a 6.4% QE and 84% polarization at 776nm. This opens another hopeful path of finding suitable photocathodes for future electron ion colliders through semiconductor photocathodes.

# Tailored Fano resonance and localized electromagnetic field enhancement in Ag gratings

Zhaozhu Li[1], J. Michael Klopf[1,2], Lei Wang[1,3], Kaida Yang[1] & Rosa A. Lukaszew[1]

Metallic gratings can support Fano resonances when illuminated with EM radiation, and their characteristic reflectivity versus incident angle lineshape can be greatly affected by the surrounding dielectric environment and the grating geometry. By using conformal oblique incidence thin film deposition onto an optical grating substrate, it is possible to increase the grating amplitude due to shadowing effects, thereby enabling tailoring of the damping processes and electromagnetic field couplings of the Fano resonances, hence optimizing the associated localized electric field intensity. To investigate these effects we compare the optical reflectivity under resonance excitation in samples prepared by oblique angle deposition (OAD) and under normal deposition (ND) onto the same patterned surfaces. We observe that by applying OAD method, the sample exhibits a deeper and narrower reflectivity dip at resonance than that obtained under ND. This can be explained in terms of a lower damping of Fano resonance on obliquely deposited sample and leads to a stronger localized electric field. This approach opens a fabrication path for applications where tailoring the electromagnetic field induced by Fano resonance can improve the figure of merit of specific device characteristics, e.g. quantum efficiency (QE) in grating-based metallic photocathodes.

Fano resonances were first introduced theoretically by Ugo Fano to explain the phenomenon of auto-ionization of Helium atoms[1]. The Fano resonance occurs when the continuum or bright mode in an electromagnetic wave interferes constructively and destructively with a discrete dark mode. Experimentally the angle-dependent reflectivity of such resonance typically exhibits an asymmetric line-shape profile. This type of resonance has been observed in several systems such as coupled clusters of metallic nano-particles[2–4], metallic photonic crystals[5] and metamaterials[2,6–9], etc. It is worth noting that this type of resonance can be used in applications including sensing[10,11], optical modulators[12–14], selective optical polarizers[15], etc., because of its unique properties. However, classical optical phenomena such as the Wood anomaly resulting from the interference between Surface Plasmon Resonance (SPR) with radiative diffraction orders have only recently been clearly understood[2,16].

We have investigated geometric effects on the Fano resonance excited on grating couplers due to its high sensitivity to the surrounding optical environment[17,18]. Several technologies for studying grating couplers have been investigated in recent times, including lithography methods[19], self-assembly[20,21], and physical vapor conformal deposition onto patterned substrates. Here we apply oblique angle deposition[22] (OAD) to the Ag vapor flux using DC sputtering to form a film conformal to a patterned substrate. Such approach might offer advantages[23] over traditional lithographic techniques for large-scale thin film fabrication.

We also investigated the enhancement of the electromagnetic field in such Ag-coated gratings and compare it with samples where the film has been deposited at normal Ag influx deposition (ND) onto identically patterned substrates. In order to correlate the optical response of such structures with the grating geometry, the surface morphology was probed using atomic force microscopy (AFM) in both cases, while the optical properties were characterized by experimental measurements of the reflectivity to detect the effect of the Fano resonance excitation on the SPR response. Electromagnetic simulations corresponding to the two types of grating structures have also been performed to better understand how the grating structure affects the localized electric field.

[1]The College of William and Mary, Department of Physics, Williamsburg, VA, 23187, USA. [2]Helmholtz Zentrum Dresden-Rossendorf, Institute for Radiation Physics, Dresden, 01324, Germany. [3]University of Virginia, Dept. of Mechanical & Aerospace Engineering, Charlottesville, VA, 22904, USA. Correspondence and requests for materials should be addressed to Z.L. (email: zli@email.wm.edu)

## Results

### Surface morphology and grating structure.
The surface morphology of both types of samples was investigated by imaging the surfaces using atomic force microscopy (AFM), shown in Fig. 1. The AFM images show a clear difference in grating amplitude for these two different types of samples. For the OAD sample, the grating amplitude of the deposited Ag thin film (~80 nm) is 15 nm higher than that of the sample grown under normal incidence geometry (~65 nm). This difference is due to shadowing effects from the underlying pattern stemming from the large incident angle ($\theta \approx 77°$) of the Ag influx onto the grating substrate during deposition. Note here that because of the steepness of the trajectory of the AFM tip during scans over the grating surface, the groove depth values for both samples could have been experimentally under-estimated.

### Reflectivity measurements.
The p-polarized reflectivity versus incident light angle was experimentally investigated on both types of samples. The samples were illuminated with 405 nm p-polarized light, with the plane of incidence perpendicular to the direction of the grooves in the patterned surface. The incidence angle was varied between 20 and 38 degrees to obtain reflectivity vs incident-angle data. The experimental reflectivity results for typical OAD and ND samples are shown in Fig. 2(a). We observe a significant difference in the shape of the reflectivity curve at the SPR angle between these two samples. A narrower and sharper resonance is noticed for the sample grown using OAD compared to the ND one. We point out that the experimental results for both samples were normalized with same parameters such as the maximum and minimum reflectivity achieved with the OAD sample. We followed the same normalization method in the simulations. This normalization was carried out to aid the comparison between samples and between experimental results and simulations.

### Simulation results.
We carried out simulations of both grating structures using the amplitude and pitch experimentally obtained under both thin film deposition geometries using EM Explorer software[24]. Using the dimensions obtained from the AFM line scan profile measurements across the surface topography of uncoated gratings, we simulated an isosceles trapezoidal profile using the same nominal dimensions for the substrate grating profile in both types of samples. The dimensions of the Ag film layer for each of the two simulated structures were set according to the AFM measurements for the OAD and ND samples. An illustration of the grating profile used in both cases is shown in Fig. 3. The reflectivity curves achieved with such simulations for both types of samples are shown in Fig. 2(b) and compared to the experimental results in Fig. 2(a). For the simulations, the Ag thin film follows the trapezoidal structure of the grating substrate homogeneously in the ND sample, while the Ag thin film in the OAD sample was distributed asymmetrically on either side of the stripe to accommodate for the shadowing effects of the oblique depostion[25]. The average thickness of the Ag thin films was set at ~60 nm for the simulated structures, agreeing with the measured profiles in the real samples. The geometrical distribution of the Ag film used to simulate the ND and OAD samples are indicated in Fig. 3(a) and (b), respectively. Note that the grating period used to better fit the ND sample results has been set at 700 nm while for the OAD, the grating pitch is set at 720 nm, an acceptable difference that is within the 5% variability of our commercial grating substrates (standard periodicity 740 nm). The simulated Ag thin film structures therefore accurately represent the two types of samples and account for the different deposition geometries investigated. The refractive index used for the simulation of the ND sample was n = 0.17, k = 2.10, while for the OAD sample n = 0.17, k = 2.20, was used. We kept the optical constants very close to each other in the simulations. In this way, we are able to examine the effect of a changing grating profile on the resonance, which is expected to have a more important role since we kept the Ag thickness similar on both samples. We note though, that the measured Ag thickness is slightly different between the two samples. This can be attributed to a different growth mode, e.g. different incident angles affecting growth rates, but we do not expect this to be a substantial effect. The value of the index of refraction used for the substrate was n = 1.56 for the simulations of both samples. Detailed information for both grating models can be observed in Fig. 3. Note that the very slight difference in the grating substrate dimensions for the OAD and ND models (e.g. 7 nm difference in the bottom width) is due to the slightly different resolution used in the simulations but this doesn't affect the results. All the values of dielectric constants are within reasonable margins (<5%) from those obtained from ref. 26.

We also want to point out that the simulation model used for the OAD sample is justified because the actual profile of the grating substrate should allow full coverage of the Ag thin film coating even if not uniform., This is expected because reflections of incident atoms from the adjacent grating groove can also occur, allowing coating of the shadowed side of the groove considered. This phenomenon was observed in ref. 22 where the authors referred to it as "excessive deposition". This full coverage of the groove is shown in Figs 1(e) and 3(b).

To understand the physical mechanisms governing our experimental optical observations regarding the difference between OAD and ND samples, we consider the process of a Fano resonance in a grating coupler. In the Fano resonance, a bright mode which is a radiative mode excited by the far-field illumination interferes with a dark mode or a localized mode. The total response is often found to be asymmetric around the resonance as it is shown in both the OAD and ND reflectivity curves (Fig. 2(a)). The main limitation of the original Fano resonance expression is that it lacks accounting of intrinsic losses due to the dark mode. Here we adopt Benjamin Gallinet and Olivier J. F. Martin's description of the Fano resonance[27–29], including consideration of intrinsic damping as shown in Eq. (1). This treatment enables understanding the influence of electromagnetic interactions on the resonance through the information drawn from a Fano profile.

The line profile for the dark mode is described in Eq. (1).

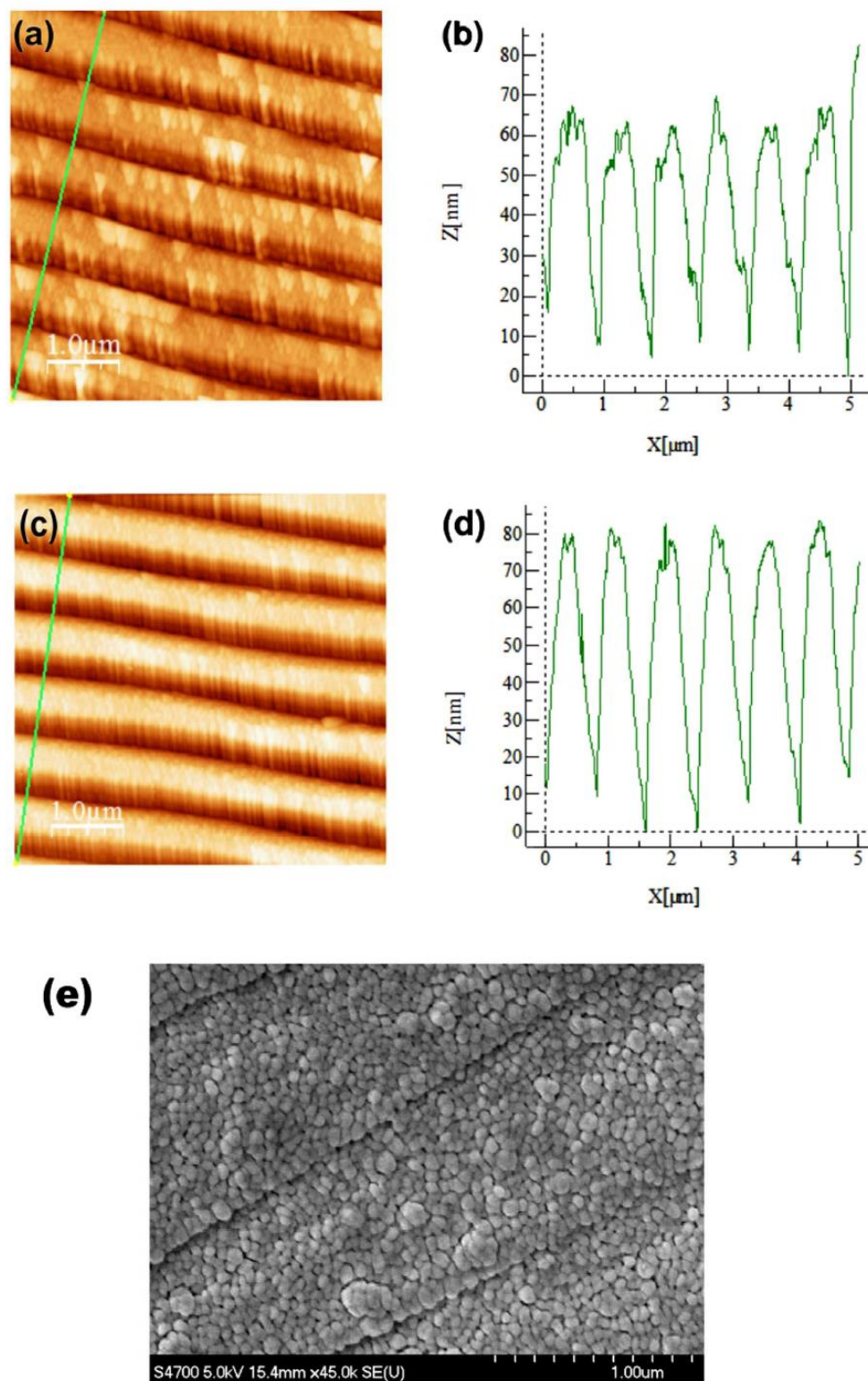**Figure 1.** (**a**) Topography image ($5\,\mu m \times 5\,\mu m$) for an ND Ag 59 nm grating sample. (**b**) Line scan along the path shown in green in (**a**). (**c**) Topography image ($5\,\mu m \times 5\,\mu m$) for an OAD Ag 50 nm grating sample. (**d**) Line scan along the path shown in green in (**c**). (**e**) SEM image of OAD sample which shows full coverage of silver thin film.
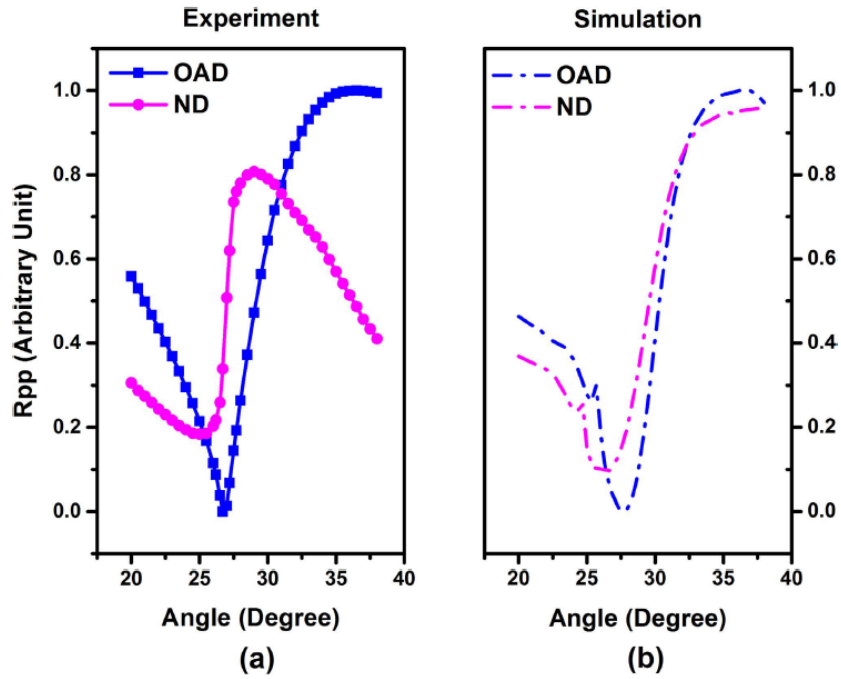
**Figure 2.** Reflectivity (Rpp) vs incidence angle (**a**) Experimental measurements and (**b**) simulations for OAD (blue) and ND (magenta) samples.
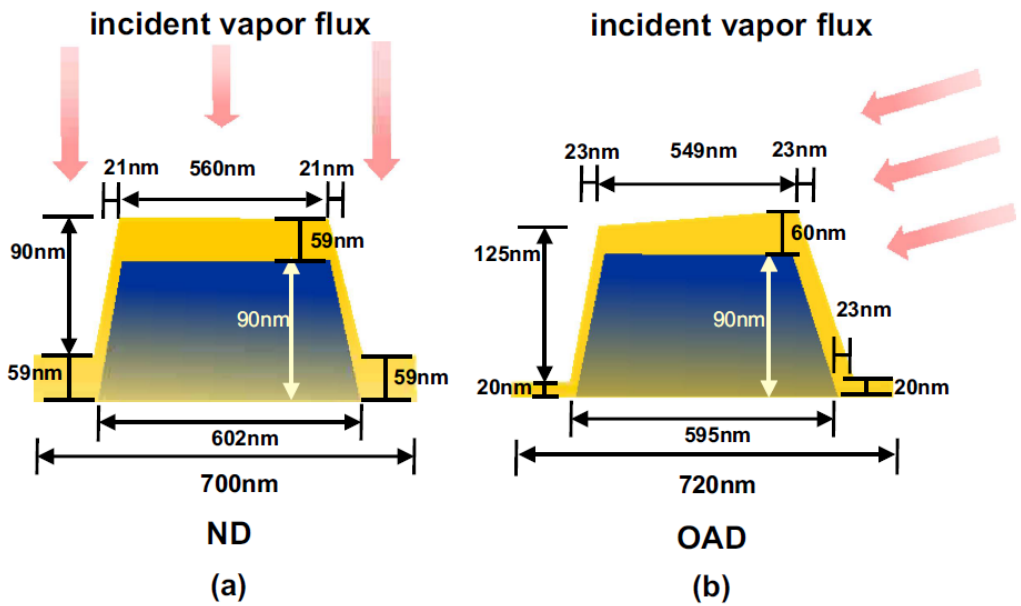


**Figure 3.** Illustration of the simulated grating profile: (**a**) ND with a nominal Ag thickness of 59 nm and (**b**) OAD with an uneven Ag deposition thickness from 20 to 60 nm.

$$r_a(\omega) = \frac{\left(\frac{\omega^2 - \omega_a^2}{2W_a\omega_a} + q\right)^2 + b}{\left(\frac{\omega^2 - \omega_a^2}{2W_a\omega_a}\right)^2 + 1}$$

(1)

**Figure 4.** Fitting results of Fano resonance for reflectivity data for ND (a) Blue: Rpp data and red: fitting curve and OAD (b) magenta: Rpp data and red: fitting curve.

Here, $\omega$ is the angular frequency of the incident light, $\omega_a$ is the resonance central spectral frequency, $W_a$ is the approximation of spectral width where $W_a \ll \omega_a$, $b$ represents the damping of the Fano resonance and affects the contrast of the resonance profile and $q$ characterizes the asymmetry of the resonance profile.
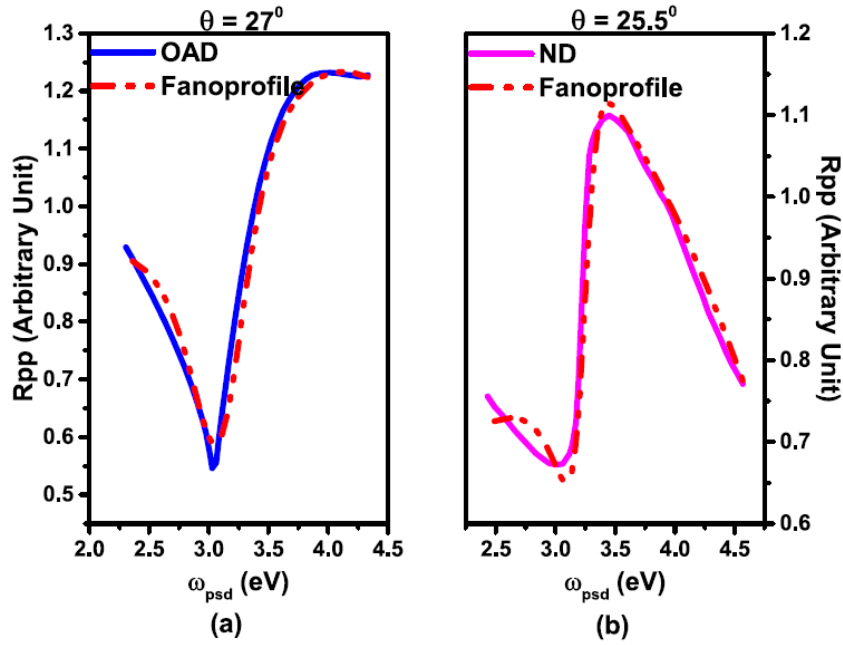
The bright mode can be constructed by pseudo Lorentzian form as in Eq. (2)

$$r_s(\omega) = \frac{a^2}{\left(\frac{\omega^2 - \omega_s^2}{2W_s\omega_s}\right)^2 + 1}$$

(2)

where $a$ is the maximum amplitude, $\omega_s$ is the resonance frequency, and $W_s$ is the approximation spectral width if $W_s \ll \omega_s$. The total response of the system is Eq. (3), given by the product of Eqs (1) and (2), and can be applied in measurable quantities for fitting parameters.

$$R(\omega) = r_a r_s$$

(3)

when light shines on a grating coupler, its horizontal component of momentum can be expressed as

$$k_{//} = \frac{\omega}{c}\sin\theta + N\frac{2\pi}{\lambda_G}$$

(4)

where $\theta$ is the incident angle, $\lambda_G$ is the grating periodicity, $N$ is the diffraction order, and $c$ is the speed of light. We measured the 0th order reflectivity, and the SPR appears when the 1st diffraction order vanishes. Thus we set $N$ as 1 and grating periodicity as the standard value $\lambda_G = 740$ nm. The reflectivity response of the incident angle in Fig. 2(a) is caused by the response of $k_{//}$ on incident angle. Thus we first calculate the value of $k_{//}$ for each $\theta$ of 405 nm light by Eq. 4. The reflectivity can now be expressed as a function of $k_{//}$. To better analyze the physics mechanism of this Fano resonance, we propose a pseudo frequency $\omega_{psd}$ and a pseudo incident angle $\theta_{psd}$, and use $\omega_{psd}$ to represent the effect of incident angle on the $k_{//}$ after setting a $\theta_{psd}$. We calculate (in Eq. 4) the value of a pseudo frequency $\omega_{psd}$ under each $k_{//}$. In this way we convert the reflectivity data to a function of $\omega_{psd}$. One can plot the reflectivity versus pseudo-angular frequency $\omega_{psd}$ as in Fig. 4 (solid lines). The new reflectivity curves are then fitted by Eq. 3 using OriginLab[30]. We show the fitting parameters along with the standard errors in Table 1 and the fitting curves dashed in Fig. 4 (red). Note that we set incident angles for both samples at their respective resonance angles. We find that varying the pseudo incident angle from 20 to 38 degrees has very little effect on the result of $q$ and $b$ for both types of samples, evidencing a characteristic relationship between these two parameters and the Fano profile itself within the considered angle range. The dark mode and bright mode for each sample are plotted as in Fig. 5 as an example. Note that the term including grating periodicity is cancelled during the calculations for each sample and the only changing part in eq. (4) is the term with $\theta$ thus it doesn't affect the fitting results.

We see that, in our fitting results, the asymmetry parameter $q$ for the OAD samples is much smaller than for the ND samples and its reflectivity shows a near symmetric resonance profile. On the other hand, the value of the

| | OAD | | ND | |
|---|---|---|---|---|
| | Fitted Value | Standard Error | Fitted Value | Standard Error |
| $w_a$ | 3.10575 | 0.01979 | 3.22967 | 0.00828 |
| $w_s$ | 3.94352 | 0.10329 | 3.53975 | 0.03437 |
| $W_a$ | 0.32953 | 0.01436 | 0.16508 | 0.00885 |
| $W_s$ | 3.12978 | 0.52405 | 2.22655 | 0.11962 |
| $q$ | 0.06475 | 0.02458 | 0.22555 | 0.0093 |
| $b$ | 0.5083 | 0.00914 | 0.83131 | 0.02203 |
| $a$ | 1.11337 | 0.00989 | 0.97496 | 0.00477 |

**Table 1.** Fitting Parameters of Fano Resonance Profile of Eq. (3), both incident angles of OAD and ND sample at its SPR angle, respectively. Standard errors are defined as in OriginLab Non-linear Fitting.
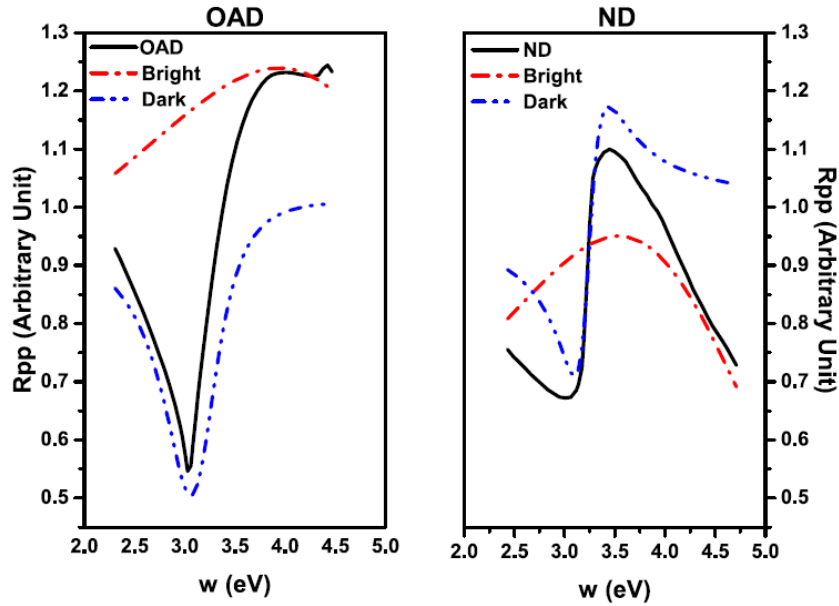


**Figure 5.** Fitted bright modes and dark modes for OAD (left) and ND (right) samples.

modulation damping parameter $b$ for the OAD samples is noticeably lower than that of the ND samples with good accuracy. The imaginary part of the dielectric permittivity in a metal would be accountable for the damping effect when there is interference between bright and dark modes, and it is considered an intrinsic loss. This damped interference displays either incomplete construction or destruction effects on the Fano profile, and the $b$ parameter evaluates such effect by comparing the ratio between the intensity lost to the metallic structure and the intensity transferred from the radiative mode to a localized mode. When $b$ equals 0, the intrinsic losses would fully disappear and the reflectivity should reach 0 at the resonance angle. A lower value of the $b$ parameter indicates lower ratio of intrinsic losses coupling radiative and localized modes. In our case, with the consideration of similar dielectric permittivity, a stronger coupling between radiative modes and localized modes in the OAD samples should be the cause of lower damping compared to the ND samples. Thus, we can conclude that the main enhancement effect in the resonance is due to lower damping in the samples grown by OAD than that of the ND ones. Such scenario suggests the existence of an associated enhanced electromagnetic field in the OAD samples, which could benefit many applications, such as photoemission from metallic photocathodes, etc. We believe that the bright mode in the Fano resonance corresponds to the 1st order diffraction in the grating as discussed in ref. 16. After diffraction of the incident of the light, the 1st order diffraction is generated and couples to the surface plasmon resonance, which is a localized mode in the Ag grating. The first order diffraction generated also diffracts and contributes to the homogenous zeroth order. As a result, the zero order diffraction is the superposition of the two interactions mentioned above.

To examine this effect in both the OAD and ND samples, we also simulated the electromagnetic field profile based on the previous model described. These simulations were carried out under the same illumination conditions as in our experiments, i.e., at the same wavelength, fluence, and critical angle as experimentally determined. The magnitude of the electric fields computed by these simulations is shown in Fig. 6. The expected stronger EM fields near the surface of the deeper-grooved (OAD) sample compared to the shallower grooved sample
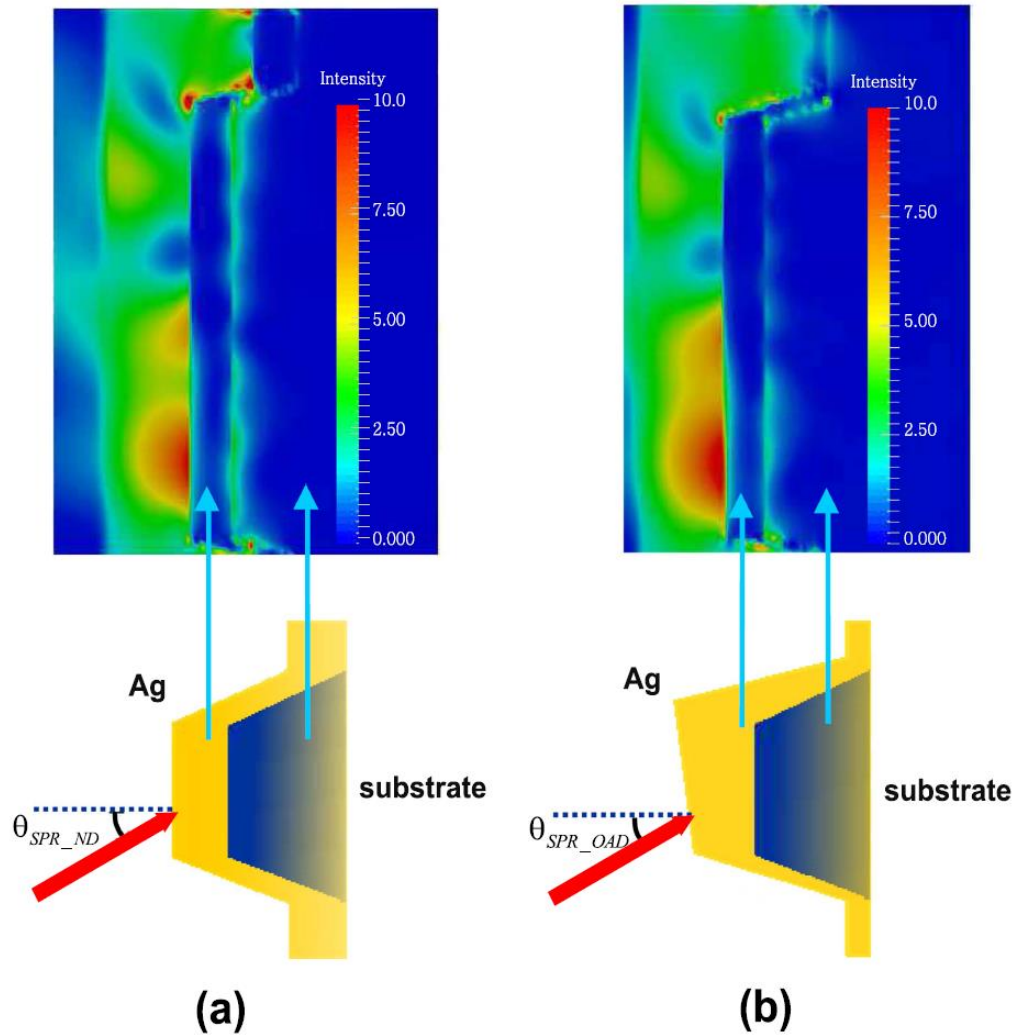
**Figure 6. Electric field intensity of both samples at its resonance angle.** (a) ND Ag sample, nominal deposition thickness of Ag 59 nm. (b) OAD Ag sample, nominal deposition thickness of Ag 50 nm. All intensities that are higher than 10 are set as red.

(ND) is confirmed, and it is attributed to a lower damping of the Fano resonance which indicates a stronger coupling of the first diffraction order with the SPR excited on the grating structure[16]. Thus we can conclude that the OAD method offers a viable approach to tailor local electromagnetic field enhancements near the surface in grating-induced Fano resonances due to our ability to control damping processes.

## Conclusion

In conclusion, we have applied conformal thin film growth techniques using different influx geometries during film deposition to tailor Ag thin film gratings using DC sputtering onto commercial optical gratings. We have compared the experimental surface topography and reflectivity curves for samples fabricated under OAD and ND geometries. Analysis of the topography reveals a somewhat deeper groove pattern for the sample obtained by OAD compared to the one obtained by ND. The enhanced optical response of the OAD sample is demonstrated by a deeper and narrower dip in the measured reflectance at the resonance angle when the Fano resonance is excited and by the higher localized electric field computed in the simulations. This enhanced Fano resonance mode is attributed to lower damping caused from stronger coupling of bright and dark modes in Ag thin film grating structures in OAD samples. These results demonstrate the possibility of enhancing the quantum efficiency in devices such as metallic photocathodes by tailoring the surface profile and hence the associated damping mechanisms at play when using plasmonic approaches such as the ones described here.

## Methods

**OAD method and sample preparation.** An illustration of OAD deposition is shown in Fig. 7(a). The sputtered beam flux is incident at angle $\theta \approx 77°$ relative to the normal direction of the grooved substrate. Because of shadowing effects from the underlying grating groove (Fig. 7(a)), asymmetric accumulation of impingent flux
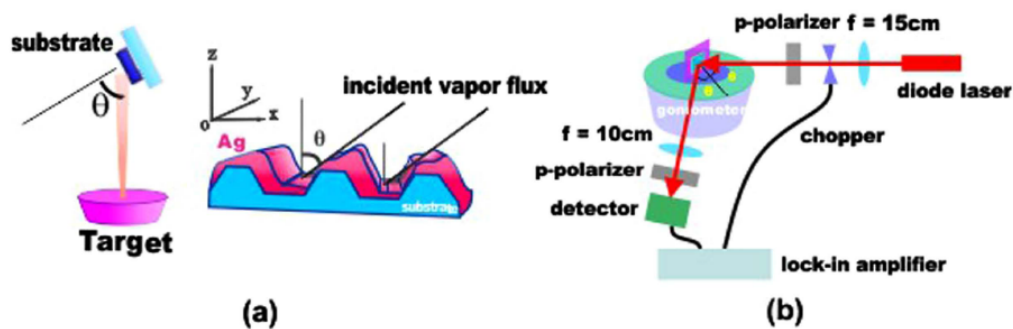
**Figure 7.** (a) Illustration of OAD method and its shadowing effects of sputtering deposition on gratings. (b) Experimental setup to measure SPR on Ag grating samples.

on the grating allows for tailoring of the resulting structure as indeed we observed. The substrates for both OAD and ND samples were loaded into a vacuum chamber with base pressure at 2.0 E-6 torr and the Ag films were grown under an Ar pressure of 7.5 E-3 torr using DC magnetron sputtering, from the same Ag target (99.9% pure) onto commercial patterned substrates, i.e., polycarbonate diffraction optical gratings. The Ag film deposition was carried out to achieve similar thickness films for both samples – around 60 nm since this thickness region was previously demonstrated to follow conformal growth. The nominal periodicity of the grating substrate is 740 nm with a 5% tolerance.

**Experiment setup for SPR measurement.** The OAD and ND structure samples were mounted on a rotational stage in a custom-built high-precision goniometer system. Each sample was mounted such that the grating grooves were normal to the plane of light incidence. A p-polarized blue diode laser ($\lambda = 405$ nm) was modulated with a 255 Hz optical chopper mounted in the path of the illuminating incident beam, and the incidence angle was varied from 20° to 38° in 0.5° increments. We used a Si photodetector (Thorlabs DET10A) and a lock-in amplifier from Standard Research Systems (SR510) to measure the zero-order reflected beam. The sample surface was aligned to the center of rotation to ensure optimal measurements in the same region of the sample surface at all angles. A schematic illustration of the optical SPR setup is shown in Fig. 7(b).

## References

1. Fano, U. Effects of configuration interaction on intensities and phase shifts. *Phys. Rev.* **124**, 1866–1878 (1961).
2. Luk'yanchuk, B. *et al.* The Fano resonance in plasmonic nanostructures and metamaterials. *Nature Mater.* **9**, 707–715 (2010).
3. Mirin, N. A., Bao, K. & Nordlander, P. Fano resonances in plasmonic nanoparticle aggregates. *J. Phys. Chem. A* **113**, 4028–4034 (2009).
4. Bao, K. *et al.* Fano resonances in planar silver nanosphere clusters. *Appl. Phys. A.* **100**, 333–339 (2010).
5. Rybin, M. V. *et al.* Fano resonance between Mie and Bragg scattering in photonic crystals. *Phys. Rev. Lett.* **103**, 023901 (2009).
6. Liu, N. *et al.* Plasmonic analogue of electromagnetically induced transparency at the Drude damping limit. *Nature Mater* **8**, 758–762 (2009).
7. Zhang, S. *et al.* Plasmon-Induced Transparency in Metamaterials. *Phys. Rev. Lett.* **101**, 047401 (2008).
8. Artar, A., Yanik, A. & Altug, H. Multispectral Plasmon Induced Transparency in Coupled Meta-Atoms. *Nano Lett* **11**, 1685–1689 (2011).
9. Fedotov, V. A., Rose, M., Prosvirnin, S. L., Papasimakis, N. & Zheludev, N. I. Sharp trapped-mode resonances in planar metamaterials with a broken structural symmetry. *Phys. Rev. Lett.* **99**, 147401 (2007).
10. Chen, C. Y., Un, I. W., Tai, N. H. & Yen, T. J. Asymmetric coupling between subradiant and superradiant plasmonic resonances and its enhanced sensing performance. *Opt. Express* **17**, 15372–15380 (2009).
11. Lahiri, B., Khokhar, A. Z., De La Rue, R. M., McMeekin, S. G. & Johnson, N. P. Asymmetric split ring resonators for optical sensing of organic materials. *Opt. Express* **17**, 1107–1115 (2009).
12. Mario, L. Y., Darmawan, S. & Chin, M. K. Asymmetric Fano resonance and bistability for high extinction ratio, large modulation depth, and low power switching. *Opt Express* **26**, 12770–12781 (2006).
13. Emani, N. K. *et al.* Electrical Modulation of Fano Resonance in Plasmonic Nanostructures Using Graphene. *Nano. Lett.* **14**, 78–82 (2014).
14. Piao, X., Yu, S. & Park, N. Control of Fano asymmetry in plasmon induced transparency and its application to plasmonic waveguide modulator. *Opt. Express* **17**, 18994–18999 (2012).
15. Christ, A., Tkhodeev, S. G., Gippius, N. A., Kuhl, J. & Giessen, H. Waveguide-plasmon polaritons: Stong coupling of photonic and electronic resonances in a metallic photonic crystal slab. *Phys. Rev. Lett.* **91**, 183901 (2003).
16. Sarrazin, M., Vigneron, J. & Vigoureus, J. Role of Wood anomalies in optical properties of thin metallic films with a bidimensional array of subwavelength holes. *Phys. Rev. B.* **67**, 085415 (2003).
17. Yang, Y. *et al.* Nonlinear Fano-Resonant Dielectric Metasurfaces *Nano Lett.* **15**, 7388–7393 (2015).
18. Cai, D. *et al.* Fano Resonances Generated in a Single Dielectric Homogeneous Nanoparticle with High Structural Symmetry *J. Phys. Chem. C.* **119**, 4252–4260 (2015)
19. Vieu, C. *et al.* Electron beam lithography: resolution limits and applications *Appl. Surf. Sci.* **164**, 111–117 (2000).
20. Hashimoto, M., Mayers, B., Garstecki, P. & Whitesides, G. M. Flowing lattices of bubbles as tunable, self-assembled diffraction gratings. *Small* **2**, 1292–1298 (2006).
21. Ye, L., Terry, B., Mefford, O. T., Rinaldi, C. & Crawford, T. M. All-nanoparticle concave diffraction grating fabricated by self-assembly onto magnetically-recorded templates. *Opt Express* **21**, 1066–1075 (2013).
22. Johnson, L., Ingersoll, K. & Kammlott, G. An oblique shadow deposition technique for altering the profile of grating relief patterns on surfaces. *Appl. Phys. Lett.* **34**, 578, doi: 10.1063/1.90873 (1979).
23. He, Y. Z., Fu, J. X. & Zhao, Y. P. Oblique angle deposition and its applications in plasmonics. *Front Phys-Beijing* **9**, 47–59 (2014).

24. EM Explorer EM Explorer: 3D FDTD EM solver, California, USA. URL http://www.emexplorer.net/ (2015).
25. Barranco, A., Borras, A., Gonzalez-Elipe, A. R. & Palmero, A. Perspectives on oblique angle deposition of thin films: From fundamentals to devices *Prog. Mater Sci.* **76**, 59–153 (2016).
26. Palik, E. *Handbook of Optical Constants of Solids* Vol. 1 (ed. Palik, E.) Ch. 11, 350 (Academic Press, 1998).
27. Gallinet, B., Lovera, A., Siegfried, T., Sigg, H. & Martin, O. J. F. Fano resonant plasmonic systems: Functioning principles and applications. *AIP Conf. Proc.* **1475**, 18–20 (2012).
28. Gallinet, B. & Marin, O. J. F. *Ab initio* theory of Fano resonances in plasmonic nanostructures and metamaterials. *Phys. Rev. B.* **83**, 235427 (2011).
29. Gallinet, B. & Martin, O. J. F. Influence of electromagnetic interactions on the line shape of plasmonic Fano resonances. *ACS Nano* **5**, 8999–9008 (2011).
30. OringinLab. Northampton, Massachusetts, USA. URL http://originlab.com/.

## Acknowledgements

## Author Contributions

Z.L., J.M.K., and K.Y. contributed to the experiments. J.M.K., R.A.L., and Z.L. analyzed the data. L.W. and Z.L. performed the numerical simulations and prepared the figures in the manuscript. Z.L. wrote the main manuscript. R.A.L. designed the experiments and supervised the project. All authors reviewed the manuscript.

## Additional Information

**Competing Interests:** The authors declare no competing financial interests.

**How to cite this article:** Li, Z. *et al.* Tailored Fano resonance and localized electromagnetic field enhancement in Ag gratings. *Sci. Rep.* **7**, 44335; doi: 10.1038/srep44335 (2017).

**Publisher's note:** Springer Nature remains neutral with regard to jurisdictional claims in published maps and institutional affiliations.

## Another Setup for QE Measurement

Before we use the described experimental setup in Jefferson Lab, we also designed and established the system in our vacuum system as in Figure 1. The mechanism of this system is the same as described in section 2.6.1.

1 Transport Fork

2 A New Arm: Manipulator

3 Faraday Cup

4 Sample holder and sample

5 Laser light

6 Additional fork to help transport the sample

Sample preparation *in-situ* under ultra high vacuum ~ E-9 torr
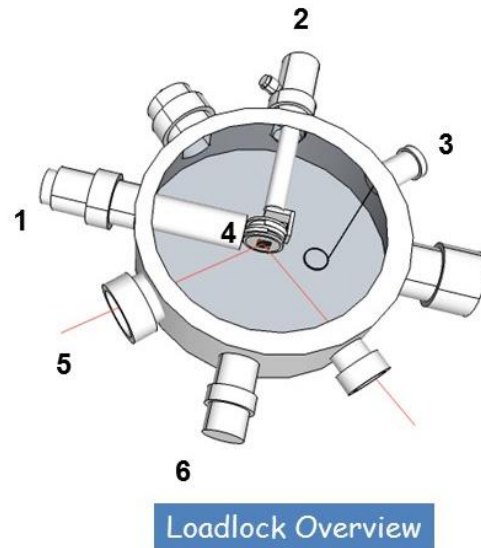
Loadlock Overview

**Figure 1 A schematic design of the QE measurement setup.**

This measurement system was located in the loadlock of a UHV system, and is in connection to the deposition chamber. It contains a new arm that receives the cathode from a transport fork. The Faraday cup was made by the copper wire and was placed ~ 2cm above the cathode surface. The laser light was incident through the window at position five. This system was used in the QE measurement of MgO/Ag/grating samples.

Before we had grown the MgO/Ag/DVD samples, we grew the silver grating cathodes on CD grating substrates. Figure 2 is the plasmonic characterization of such samples. Preliminary measurement showed a result of ~0.1pA.
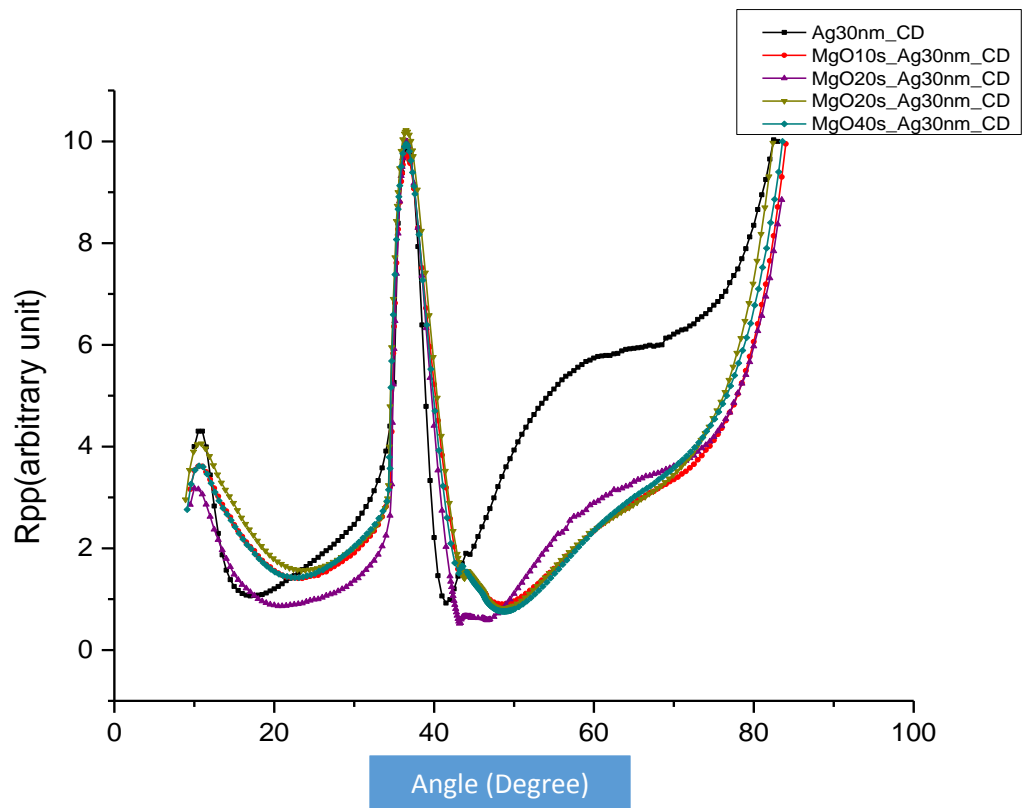
**Figure 1 Reflectivity measurement of different deposition time of MgO on Ag30nm/CD samples.**

# REFERENCES

1. C. Prescott, et al., Phys. Lett. B 84, 524 (1979).

2. T. Maruyama, et al., Appl. Phys. Lett. 85, 2640 (2004).

3. C. Berglund and W. Spicer, Phys. Rev. A 136, 1030 (1964).

4. H. Raether, Surface Plasmons on Smooth and Rough Surfaces and on Gratings, Springer (1986).

5. C.J. Powell, J.B. Swan, Phys. Rev. 118, 640 (1960).

6. B. Luk'yanchuk, et al., Nature Mater. 9, 707 (2010).

7. A. Mirin, K. Bao, & P. Nordlander, J. Phys. Chem. A 113, 4028 (2009).

8. K. Bao, et al., Appl. Phys. A. 100, 333 (2010).

9. M. Rybin, et al., Phys. Rev. Lett. 103, 023901 (2009).

10. N. Liu, et al. Nature Mater 8, 758 (2009).

11. S. Zhang, et al. Phys. Rev. Lett. 101, 047401 (2008).

12. A. Artar, A. Yanik, H. Altug, Nano Lett 11, 1685 (2011).

13. V. Fedotov, et al., Phys. Rev. Lett. 99, 147401 (2007).

14. C. Chen, et al., Opt. Express 17, 15372 (2009).

15. B. Lahiri, et al., Opt. Express 17, 1107 (2009).

16. L. Mario, S. Darmawan, M. Chin, Opt Express 26, 12770 (2006).

17. N. Emani, et al., Nano. Lett. 14, 78 (2014).

18. X. Piao, S. Yu, N. Park, Opt. Express 17, 18994 (2012).

19. A. Christ et al., Phys. Rev. Lett. 91, 183901 (2003).

20. M. Sarrazin, J. Vigneron, J. Vigoureus, Phys. Rev. B. 67, 085415 (2003).

21. U. Fano, Phys. Rev. 124, 1866 (1961).

22. B. Gallinet, et al., AIP Conf. Proc. 1475, 18 (2012).

23. B. Gallinet, et al., Phys. Rev. B. 83, 235427 (2011).

24. B. Gallinet et al., ACS Nano 5, 8999 (2011). (Chapter 1 ends)

25. John O, A User's Guide to Vacuum Technology, Chapter 7, page 173 (1980).

26. John O, A User's Guide to Vacuum Technology, Chapter 11, page 301(1980).

27. http://www.gammavacuum.com/index.php/theory-of-operation/

28. Milton Ohring, The Materials Science of Thin Films, Chapter 2, page 68 (1992).

29. https://www.saesgetters.com/sites/default/files/Principle%20of%20Operation_0.pdf

30. http://www.thinksrs.com/downloads/PDFs/Manuals/RGAm.pdf

31. Milton Ohring, The Materials Science of Thin Films, Chapter 3, page 82 (1992).

32. https://en.wikipedia.org/wiki/Electron_beam_physical_vapor_deposition.

33. Ed. K. Seshan, Handbook of Thin Film Deposition, Chapter 4, page 56 (2012).

34. Ed. K. Seshan, Handbook of Thin Film Deposition, Chapter 4, page 62 (2012).

35. S. Hwang Lein, D. Robert, D. Morgan. Kirk Othmer Encyclopedia of Chemical Technology, page 343 (2005).

36. A. Oliva-Florio. et al., P.R.B, 35, 5 (1987).

37. D. Donnet, et al., J. Appl. Phys. 79 (8) (1996).

38. X. Liu, A. Morisako, J. Magn. Magn. Mater. 310, e916 (2007).

39. Y. Kudriavtsev et, al., Appl. Surf. Sci. 239 273–278 (2005).

40. M. Ohring, The Materials Sciencen of Thin Films, Chapter 3, page 126 (1992).

41. Vieu, C. et al., Appl. Surf. Sci. 164,111–117 (2000).

42. M Hashimoto,et al., Small 2, 1292-1298 (2006).

43. L. Ye et al., Opt Express 21, 1066-1075 (2013).

44. A. Barranco et al., Prog. Mater Sci. 76, 59 (2016).

45. L. Johnson, K. Ingersoll, G. Kammlott, Appl. Phys. Lett. 34, 578 (1979).

46. G.Binnig and C.F. Quate, Phys. Rev. Lett., 56, 930 (1986).

47. P. Eaton and P. West, Atomic Force Microscopy, Oxford University Press, Chapter 2, page 15 (2010).

48. L.Reimer, Scanning Electron Microscopy, Physics of Image Formation and Microanalysis, 2nd Edition, Springer, Chapter 1, page 1 (1998).

49. https://www.bruker.com/fileadmin/user_upload/8-PDF-Docs/X-rayDiffraction_ElementalAnalysis/XRD/Webinars/Bruker_AXS_Good_Diffraction_Practice_I_-_X-ray_Reflectometry.pdf

50. http://www.panalytical.com/Empyrean/Features.htm

51. http://www.ni.com/labview/

52. https://www.saesgetters.com/

53. J. Uebbing, and L. James, J. Appl. Phys. 41, 4505 (1970).

54. http://www.thorlabs.com/

55. 52. S.S.P. Parkin, et al., Nat. Mater. 3,862 (2004).

56. S.Yuasa, et al., Nat. Mater. 3, 868-871(2004).

57. K. McKenna, P. Sushko and A. Shluger, J. Phys. Chem. C. 111,2823 (2007).

58. C. Harding, et al., J. Am. Chem. Soc.,131, 538 (2009).

59. J. Goniakowski, et al., J. Chem. Phys. 130, 174703 (2009).

60. C.R. Henry, Surf. Sci. Rep. 31,231 (1998).

61. S. Schintke and W.-D. Schneider, J. Phys.: Condens. Matter 16, R49 (2004).

62. S. A. Chambers, Surf. Sci. Rep. 39, 105 (2000).

63. G. Pacchioni, L. Giordano, and M. Baistrocchi, Phys. Rev. Lett. 94, 226104 (2005).

64. V. Heine, Phys. Rev. 138, A1689 (1965).

65. J. Tersoff, Phys. Rev. B 32, 6968 (1985).

66. S. G. Louie, J. R. Chelikowsky, and M. L. Cohen, Phys. Rev. B 15, 2154 (1977).

67. W. Mönch, J. Vac. Sci. Technol. B 17, 1867 (1999).

68. L. Giordano, F. Cinquini and G. Pacchioni, Phys. Rev. B., 73, 045414 (2006).

69. J. Goniakowski and C. Noguera, Interface Sci. 12, 93 (2004).

70. L. G. M. Pettersson and P. S. Bagus, Phys. Rev. Lett. 56, 500 (1986).

71. A. Michaelides, et al., Phys. Rev. Lett. 90, 246103 (2003).

72. A. Migani, C. Sousa, and F. Illas, Surf. Sci. 574, 297 (2005).

73. S. Prada, U. Martinez, G. Pacchioni, Phys. Rev. B., 78, 235423 (2008).

74. T Konig., et al., J. Phys. Chem. C, 113, 11301 (2009).

75. T. Jaouen, et al., App. Phys. Lett., 97, 232104 (2010).

76.  M. Akbi and A. Lefort J. Phys. D: Appl. Phys. 31, 1301, (1998)

77. T. Droubay, et al., Phys. Rev. Lett. 112, 067601 (2014). (Chapter 3 ends)

78. M. Burt and V. Heine, J. Phys. C: Solid State Phys. 11 961 (1978).

79. G. Tompa, W. Carr, and M. Seidl, Appl. Phys. Lett. 49, 1511 (1986).

80. https://ireap.umd.edu/sites/default/files/documents/Balter_0.pdf

81. https://www.tedpella.com/semmisc_html/sempaint.htm#anchor16062.

82. Hawkeye, M., Brett, M., J. Vac. Sci. Technol., A 25, 1317 (2007).

83. Johnson, L., Ingersoll, K., Kammlott, G., Appl. Phys. Lett. 34, 578 (1979).

84. EM Explorer (2015). EM Explorer: 3D FDTD EM solver, California, USA. URL

   http://www.emexplorer.net/

85. Palik, E. Handbook of Optical Constants of Solids Vol.1 (ed. Palik, E.) Ch. 11, 350

   (Academic Press, 1998).

86. OringinLab. Northampton, Massachusetts, USA. URL http://originlab.com/

87. N. Hannay, Electronic Materials, Chapter 16, Page 443 (2012).

88. R. A. D. Groot, et al., Physical Review Letters, 50(25) (1983).

89. Lu, Y. et al., Phys. Rev. B 54, R8357 (1996).

90. J. Z. Sun, et al., Appl. Phys. Lett. 70, 1769 (1997).

91. G. L. Bona, et al., Solid State Commun. 56, 391 (1985).

92.  W. Liu, Appl. Phys. Lett. 109, 252104 (2016).

# VITA

**Zhaozhu Li**

Zhaozhu Li was born in Qiqihar, Heilongjiang, China. She developed a special interest in Physics since she was a teenager. She received her B.S. in 2009 and began her pursuit of advanced studies of Physics at the College of William and Mary in that same year. She joined Professor Lukaszew's group in 2011 and has been working on plasmonic approaches for silver-based photocathodes.

**HONORS & AWARDS**
The Cheryl Griffith Tropf Fellowship in Physics (2017)
AVS 60th International Symposium and Exhibition: Vacuum Science Division Student Award (2013)
JSA/JLab Graduate Fellowship (2012-2013)

**PUBLICATIONS**
"Tailored Fano resonance and localized electromagnetic field enhancement in Ag gratings" **Z Li**, *et al.*, Sci. Rep. **7**, 44335 (2017).
"Temperature and microstructural effects on the superconducting properties of niobium thin films" M. Beebe, *et al.*, IEEE Trans. Appl. Supercond. **27**(4) (2017).
"Enhancing Silver Photocathode Performance by Exciting Surface Plasmon Resonance on Ag corrugated thin films" **Z Li**, *et al.*, Advanced Photonics 2015, OSA Technical Digest, paper NS1A.3 (2015).
"Surface plasmon resonance modulation in nanopatterned Au gratings by the insulator-metal transition in vanadium dioxide films", M. Beebe *et al.*, Opt. Express **23**, 13222-13229 (2015).
"Optical Studies on VO2 Thin Films" L. Wang et al., Mater Res Soc Symp Proc **1803** (2015). doi:10.1557/opl.2015.454.
"Magnetic Shielding Larger Than the Lower Critical Field of Niobium in Multilayers", W. Roach, *et al.*, IEEE Trans. Appl. Supercond. **23**(3) (2013).
"NbN thin films for superconducting radio frequency cavities", W. Roach, *et al.*, Supercond. Sci. Technol. **25**(12) (2012).
"Niobium nitride thin films and multilayers for superconducting radio frequency cavities", W. Roach, *et al.*, ASC (2012).
"Surface and Interface Roughness Analysis of Ultrathin Co/Pd Multilayer for Magnetic Tunnel Junctions", K. Yang, *et al.*, IcAUMs (2012).